An Experimental Study on the Dynamics of a Cantilevered Pipe Aspirating Fluid and Subjected to Reverse External Axial Flow

Ahmed Shaaban

Master of Engineering

Department of Mechanical Engineering

McGill University

Montreal, Québec, Canada

October 18th, 2022

A thesis Submitted to McGill University in partial fulfillment of the requirements of the degree of Master of Engineering

ABSTRACT

The dynamics of a hanging cantilevered pipe aspirating fluid simultaneously subjected to a partially confined external axial flow in the reverse direction has been investigated experimentally. A bench-top-size apparatus is used in the experiments consisting of a pressure vessel filled with water, containing a hanging cantilevered pipe and a shorter concentric outer rigid tube which is also vertically cantilevered. The flow configuration under consideration is a simplified representation of the hydrocarbon storage mode in salt-mined caverns, which are large underground cavities used for storing hydrocarbons.

A parametric study was performed to examine the effect of annular gap size, pipe length, eccentric positioning of the rigid tube relative to the central pipe, and of a constriction at the inlet/outlet of the outer rigid tube, on the onset of instability for various external to internal flow velocity ratios, U_o/U_i, ranging from 0.015 to 0.80.

Experiments were conducted for a wide annular gap and the results were compared to those from a previous study in which a narrower rigid tube was utilized. It was found that, for the range of flow velocity ratios investigated, the pipe loses stability via first-mode flutter. The experimental results were sorted into two ranges of flow velocity ratios, namely low ($U_o/U_i = 0.015 – 0.06$) and high ($U_o/U_i = 0.20 – 0.80$), in which different dynamical behaviours were observed. The results demonstrate that the onset of instability occurs at relatively lower flow velocities as the U_o/U_i ratio is increased. Moreover, enlarging the annular gap has a destabilizing effect on the aspirating pipe, in terms of rms amplitude and onset of instability. In comparison with the narrower rigid tube, with a wider rigid tube the signal power of the second-mode frequency was significantly amplified.

In studies with shorter pipe lengths, it was shown that the dynamical behavior remained similar to those of a longer pipe, for all flow velocity ratios, with regards to rms amplitude trends and type of instability. However, the onset of instability was delayed for the shorter pipes.

The eccentricity experiments demonstrated a similar dynamical behaviour to the concentric case in terms of rms amplitude trends and type of instability. A higher amplitude was observed for all U_o/U_i ratios with increasing eccentricity, i.e., for a larger gap between the centers of the rigid tube and pipe. Additionally, there was also a clear destabilization in terms of critical flow velocities for low flow velocity ratios. For the higher flow velocity ratios, the first critical flow velocity remained approximately unchanged, but the second critical flow velocity was delayed with increasing eccentricity.

The flow separation experiments, in which a narrow passage was formed at the inlet or outlet of the annulus, once more demonstrated similar dynamical, rms amplitude, and instability trends to the case with no separation for high U_o/U_i ratios. However, for low U_o/U_i ratios, the trend in rms amplitude was not preserved. The critical flow velocities for all U_o/U_i ratios were decreased, regardless of the position of the constriction. Moreover, a constriction at the entrance of the annulus resulted in an increase in the rms amplitude, whereas a constriction at the outlet resulted in a decrease.

SOMMAIRE

La dynamique d'un tuyau suspendu en porte-à-faux aspirant un fluide et soumis simultanément à un écoulement axial externe partiellement confiné dans la direction inverse a été étudiée expérimentalement. Un appareil de laboratoire est utilisé dans les expériences, consistant en un réservoir sous pression rempli d'eau, contenant un tuyau suspendu en porte-à-faux et un tube rigide extérieur concentrique plus court qui est également en porte-à-faux verticalement. La configuration d'écoulement étudiée est une représentation simplifiée du mode de stockage des hydrocarbures dans les cavernes salines, qui sont de grandes cavités souterraines utilisées pour le stockage des hydrocarbures.

Une étude paramétrique a été réalisée pour examiner l'effet de la taille de l'espace annulaire, de la longueur du tube, du positionnement excentrique du tube rigide par rapport au tube central, et d'une constriction à l'entrée/sortie du tube rigide extérieur, sur le début de l'instabilité pour différents rapports de vitesse d'écoulement externe/interne, U_o/U_i, allant de 0.015 à 0.80.

Des expériences ont été menées pour un large espace annulaire et les résultats ont été comparés à ceux d'une étude précédente dans laquelle un tube rigide plus étroit a été utilisé. Il a été constaté que, pour la gamme des rapports de vitesse d'écoulement étudiés, le tube perd sa stabilité par flottement au premier mode. Les résultats expérimentaux ont été classés en deux gammes de rapports de vitesse d'écoulement, à savoir faible ($U_o/U_i = 0.015 - 0.06$) et élevé ($U_o/U_i = 0.20 - 0.80$), dans lesquelles des comportements dynamiques différents ont été observés. Les résultats montrent que le début de l'instabilité se produit à de vitesses d'écoulement relativement plus faibles lorsque le rapport U_o/U_i augmente. De plus, l'élargissement de l'espace annulaire a un effet déstabilisant sur le tube aspirant, en termes d'amplitude rms et du seuil d'instabilité. En

comparaison avec le tube rigide plus étroit, avec un tube rigide plus large, la puissance du signal de la fréquence du second mode a été significativement amplifiée.

Dans les études avec de tuyaux plus courts, il a été démontré que le comportement dynamique est similaire à celui d'un tuyau plus long, pour tous les rapports de vitesse d'écoulement, en ce qui concerne les tendances d'amplitude rms et le type d'instabilité. Cependant, le seuil de l'instabilité a été retardé pour les tuyaux plus courts.

Les expériences d'excentricité ont démontré un comportement dynamique similaire au cas concentrique en termes de tendances d'amplitude rms et de type d'instabilité. Une amplitude plus élevée a été observée pour tous les rapports U_o/U_i avec une excentricité croissante, c'est-à-dire pour un écart plus grand entre les centres du tube rigide et du tuyau qui l’entoure. De plus, il y avait également une déstabilisation claire en termes de vitesses d'écoulement critiques pour les faibles rapports de vitesse d'écoulement. Pour les rapports de vitesse d'écoulement plus élevés, la première vitesse d'écoulement critique est restée approximativement inchangée, mais la deuxième vitesse d'écoulement critique a été retardée avec l'augmentation de l'excentricité.

Les expériences de séparation de l'écoulement, dans lesquelles un passage étroit a été formé à l'entrée ou à la sortie de l'anneau, ont démontré une fois de plus de tendances similaires en termes de dynamique, d'amplitude rms et d'instabilité par rapport au cas sans séparation pour des rapports U_o/U_i élevés. Cependant, pour les faibles rapports U_o/U_i, la tendance de l'amplitude rms n'a pas été préservée. Les vitesses d'écoulement critiques pour tous les rapports U_o/U_i ont diminué, quelle que soit la position de la constriction. De plus, une constriction à l'entrée de l'anneau a entraîné une augmentation de l'amplitude rms, alors qu'une constriction à la sortie a entraîné une diminution.

ACKNOWLEDGEMENTS

First and foremost, I would like to express my sincere gratitude to my research supervisors Professor Michael P. Païdoussis and Professor Arun K. Misra for accepting me as a graduate student and for the opportunity to be part of the Fluid-Structure Interaction (FSI) research group as well as for the support and encouragement throughout my studies.

Special thanks to my colleague and friend, Mahdi Chehreghani, for his help at the beginning of my M.Eng. study and for the planning, coordinating, and discussion of the experiments over my time at the FSI lab.

I would like to thank Mary Fiorilli St-Germain for assistance and guidance in administrative matters.

I would like to acknowledge the financial support provided by the Department of Mechanical Engineering of McGill University through a Graduate Excellence Fellowship award. I would also like to gratefully acknowledge the financial support provided by the Natural Sciences and Engineering Research Council of Canada (NSERC), Solution Mining Research Institute (SMRI), and Pipeline Research Council International (PRCI).

Finally, I would like to thank my parents and siblings for their love and support throughout my life.

TABLE OF CONTENTS

LIST OF FIGURES

LIST OF TABLES

Appendix A

Chapter 1 : Introduction

1.1 Fluid-structure interactions

Fluid-structure interaction (FSI) is the consequence of a multiphysics coupling between the laws that govern fluid dynamics and structural mechanics. FSI problems are represented by the interactions between deformable or mobile slender structures and the surrounding external or internal flow [1]. The flow of fluid over a slender structure exposes it flow-induced loads due to the stresses and strains exerted on the solid structure. These flow-induced loads are modeled as forces generating flow-induced vibrations (FIV) which can lead to static or oscillatory structural deformations, with the behaviour of the fluid affected accordingly. The magnitude of the deformation is dependent on the material properties of the slender structure as well as the pressure and velocity of the fluid-flow field [2].

Flow-induced vibrations (FIV) of slender structures have been extensively studied over the past decade due to the increased demand for stability and reliability in many industrial applications, including power generators, heat exchangers, ocean mining pipes, drill-strings, brine-strings in salt-mined caverns, and many other applications [3]. The slender structures utilized in the aforementioned applications include pipes, cylinders, shells, and plates.

The work presented in this thesis is focused on the dynamics of cantilevered pipes simultaneously subjected to internal and external axial flows. A lot of work has been devoted to the understanding of the dynamics of pipes conveying fluid due to the interesting flow-induced instabilities observed, and hence the system is referred to as a paradigm in dynamics. The type of instability experienced by fluid-conveying pipes at sufficiently high flow velocities is dependent on the boundary conditions and is either flutter or static divergence (buckling). The influence of the boundary conditions can be illustrated through the following cases: cantilevered pipes conveying fluid lose stability via flutter, i.e., an oscillatory instability, whereas pipes clamped at both ends are subjected to static divergence, i.e., buckling [4].

The study of the dynamics of a pipe conveying fluid has been and remains primarily motivated by curiosity rather than application [8]. However, it does have engineering applications. Cocurrent and countercurrent flow heat exchangers and drill-strings in drilling rig systems are some examples which could be modeled as a pipe simultaneously subjected to internal and external axial flows, as illustrated in Figure 1-1 [5,6]. Another system that can be idealized and modeled in a similar manner is in solution-mined caverns.

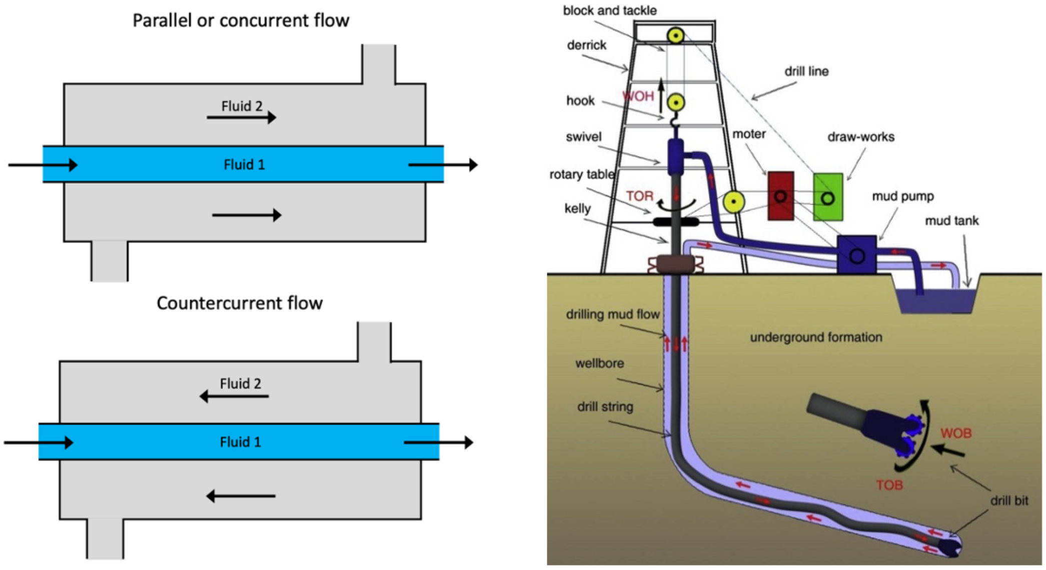

(a) (b)

Figure 1-1: Schematics of (a) cocurrent and countercurrent flow heat exchangers; (b) a drilling rig system [7].

1.2 Solution-mined caverns

The operation of solution-mined caverns is a typical application that utilizes both types of fluid conveying pipes: discharging and aspirating pipes. Salt-mined caverns involve a long cantilevered pipe, known as the “brine-string”, and an annular region formed by a cantilevered cemented casing surrounding the upper portion of the pipe. Caverns are man-made by drilling a well into the salt formation and pushing water down the well to dissolve the salt, which returns to the surface as brine. The salt-mined cavern formation is completed by employing alternatively the “direct” or “reverse” circulation processes to achieve the desired cavern shape and size, as shown in Figure 1-2 [9]. Direct circulation refers to the injection of low-concentration brine or fresh water downward through the inner tubing (the “brine-string”) into the cavern, and high-concentration brine is forced to flow upward through the “outer tubing” or the annular region separating the outer tube and inner pipe; refer to Figure 1-2(a). The inverse process, referred to as reverse circulation, is carried out by injecting low-concentration brine or fresh water downwards through the annular region and extracting high-concentration brine by flowing upwards through the brine-string; refer to Figure 1-2(b).

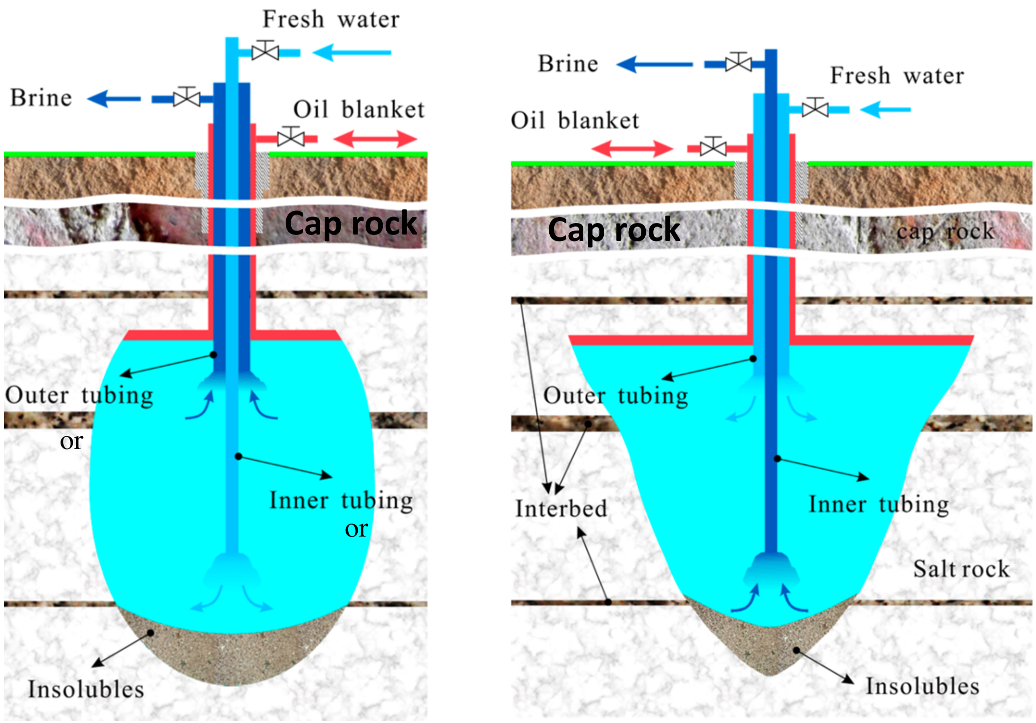

(a) (b)

Figure 1-2: (a) Direct circulation: low-concentration brine or fresh water injected through the brine-string and brine flows upwards through the outer tubing; (b) Reverse circulation: low-concentration brine or fresh water injected through the outer tubing and brine flows upwards through the brine string [9].

Once the cavern is created and fully filled with brine, it may be used for hydrocarbon storage. Essentially, solution-mined caverns can be used in two different operation modes. The first mode is for hydrocarbon storage, where hydrocarbons are injected downwards through the annulus displacing the brine upwards through the hanging brine-string; the second mode is the hydrocarbon production or retrieval mode, which is the inverse of the storage mode: hydrocarbons are extracted through the annulus by displacement with brine injected through the brine-string; refer to Figure 1-3. The production mode is similar to the flow configuration used for direct circulation, illustrated in Figure 1-2(a) and the storage mode utilizes the inverse flow configuration, i.e., reverse circulation, illustrated in Figure 1-2(b).

Salt-mined caverns being open vessels offer a high delivery rate, which is why they are used for “peak” loads or short-term trading requiring high extraction flow rates [10]. However, the high extraction rates come with a drawback: brine-string oscillations become more pronounced at high flow velocities and could potentially lead to impact on the rigid casing, which may damage the brine-string and even break it in severe cases. It is estimated that in the past few decades, twenty-one accidents involving gas and petroleum leaks have occurred in salt-mined caverns [11]. Therefore, it is essential to understand the dynamics of both aspirating and discharging brine-strings to prevent such catastrophic accidents from occurring.

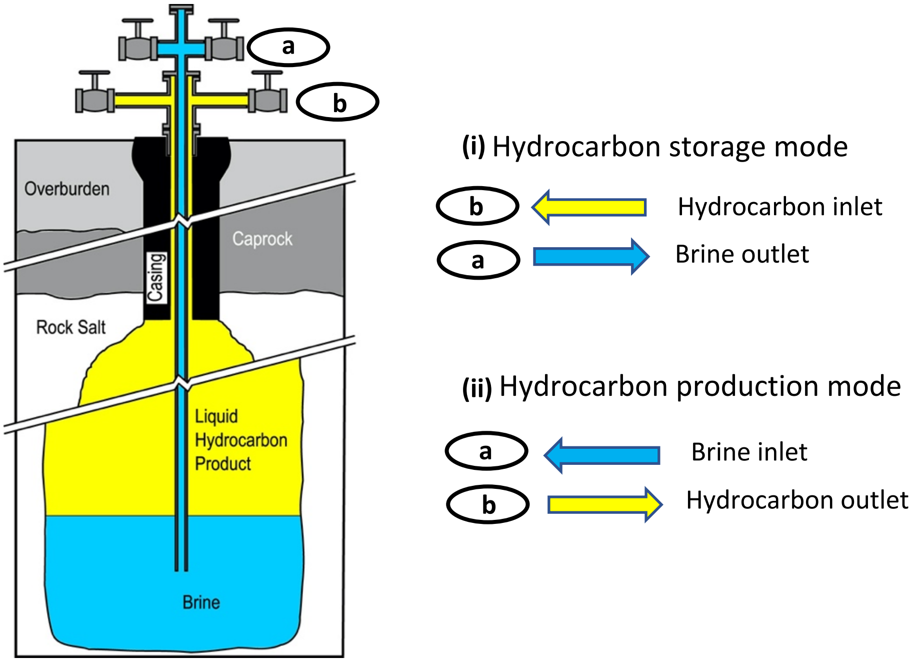

Figure 1-3: Schematic outlining the operation modes of solution-mined caverns. (i) hydrocarbon storage; (ii) hydrocarbon production [12].

1.3 Literature review

The system under consideration is an idealized model of solution-mined caverns which consists of a hanging cantilevered conveying pipe and counter-currently subjected to a partially confined external flow through a coaxial annular region over its upper portion. There are several comprehensive reviews available on the subject for interested readers, including the two volumes of the book by Païdoussis [4,13]. Accordingly, the literature review in this thesis concentrates on the most relevant studies on the subject in the following order: (i) pipes conveying fluid; (ii) cylinders in axial flow; (iii) pipes simultaneously subjected to internal and external axial flows. After discussion of the effects of internal and external axial flows separately, it becomes easier to see the coupled effect which is representative of the work conducted in the current investigation.

1.3.1 Pipes discharging fluid

The earliest work on conveying pipes was conducted by Bourrières [14] in 1939, the pipe and fluid were modeled as two interacting inextensible strings, such that the inner string is in motion relative to the outer one, and the string representing the pipe is assumed to be infinitely flexible. The linear equation of motion for a cantilevered pipe was obtained and the vibration of the pipe was observed experimentally. Several authors conducted analytical and experimental studies on fluid-conveying pipes subject to different boundary conditions between 1950 and 1955. These include Ashley and Haviland [15], Feodos'yev [16], Housner [17], Long [18], and Handelman [19]. The purpose of these studies was to understand the influence of the fluid flow on the pipe's stability and natural frequencies. There was also a model developed by Niordson [20] in 1953 for pipes of nonuniform cross-section where the pipe was modeled and analyzed as a beam, similar to the other studies; however, initially the pipe was modeled as a circular cylindrical shell but the resultant equations were not solved.

In 1962, Benjamin [21] investigated theoretically the problem of articulated pipes conveying fluid and found that the pipe may lose stability due to buckling or amplified oscillation if it is positioned vertically. However, if the motion is constrained to the horizontal plane, buckling is not possible. The theoretical predictions were supported by an experimental investigation [22]. Gregory and Païdoussis [23] extended Benjamin's model to account for continuous flexible tubular cantilevers conveying fluid, i.e., with an infinite number of degrees of freedom. The onset of instability or critical flow velocity was obtained theoretically and validated experimentally [24].

In 1970, Païdoussis [25] investigated two systems comprising a tubular cantilever discharging fluid: (a) hanging cantilever and (b) "standing" cantilever. The hanging cantilever lost stability by flutter, i.e., by an oscillatory instability, at sufficiently high flow velocity, as opposed to the articulated pipes which were subjected to buckling [21, 22]. The "standing" cantilever was found to buckle under its own weight when there is no flow in the pipe, but as the flow velocity increased the pipe was restabilized; however, the pipe became unstable due to flutter at higher flow velocities. Experiments were carried out and found to be reasonably in good agreement with the theoretical predictions.

Stein and Tobriner [26] studied for the first time pipes of infinite length and were able to provide an expression to compute the critical flow velocity and frequency. The pipes were found to become unstable by flutter beyond a specific flow velocity.

The preceding theoretical studies modeled the pipe conveying fluid as a beam restricted to lateral motions with the exception of the work by Niordson [20] as discussed earlier. Païdoussis and Denise [27, 28] modeled very thin pipes conveying fluids with a variety of boundary conditions using thin-shell theory. Another study was conducted by Shayo and Ellen [29] in which cantilevered pipes were modeled using both shell and beam modes. The theory in [28] predicted a shell-mode flutter instability for cantilevered shells, whereas clamped-clamped shells were found to lose stability due to buckling followed by coupled-mode flutter.

The dynamics of flexible pipes containing flowing fluid was investigated theoretically by Païdoussis and Issid [30] for the following cases: (a) constant flow velocity and (b) harmonically varying flow velocity. It was found that pipes with both ends supported such as clamped-clamped or pinned-pinned lose stability by buckling followed by coupled-mode flutter at higher flow velocities, whereas cantilevered pipes are subjected to single-mode flutter. An experimental investigation, motivated by offshore applications such as marine risers and deep ocean mining, was conducted by Shilling and Lou [31] for the system consisting of a vertical cantilever pipe conveying fluid and immersed in a tank filled with still water. It was concluded that the internal flow rate and the degree of immersion of the pipe in the fluid could substantially influence the natural frequencies of the system.

In 1969, Thurman and Mote [32] developed the first nonlinear model for a simply supported pipe conveying fluid. The purpose of this study was to show the limits of linear analysis and to show the importance of nonlinear terms in the equations of motion for the system under consideration. Holmes [33, 34] individually and in a study with Marsden [35] extended the linear model by Païdoussis and Issid [30] to include the non-linear terms corresponding to the deflection-induced tension in the pipe. It was found that pipes with both ends supported cannot become unstable via coupled-mode flutter as was predicted in [30], whereas a cantilevered pipe was predicted to lose stability via Hopf bifurcation, i.e., flutter, at sufficiently high flow velocities. Rousselet and Herrmann [36, 37] developed a non-linear model for a pipe conveying fluid utilizing two distinct methods: (a) force-balance (or Newtonian) and (b) energy methods. Additionally, a flow expression was derived considering the pressure drop due to fluid friction within the pipe.

Further work on the system was conducted by Lundgren et al. [38] with the addition of an inclined terminal nozzle at the free end of a cantilevered pipe. The predictions of the non-linear model, utilizing a set of integrodifferential equations, were found to be qualitatively in agreement with the basic experiments conducted. The model in [38] was reutilized by Bajaj et al. [39] for a fluid-conveying pipe without a nozzle. It was found that instability via a Hopf bifurcation may occur and could be either sub- or supercritical, regulated by the parameter related to the pressure loss within the pipe.

The planar dynamics of cantilevered pipes conveying fluid, with focus on the nonlinear effects due to the addition of motion-limiting constraints, was studied both experimentally and theoretically by Païdoussis and Moon [40]. Period-doubling and chaos were predicted as a result of the interaction of limit-cycle motions at flow velocities past the Hopf bifurcation, in addition to the potential wells corresponding to the buckling of the pipe due to the existence of the motion constraints. Semler [41] and Semler et al. [42] derived planar nonlinear equations of motion for a fluid-conveying pipe for both the simply supported and cantilevered boundary conditions. The nonlinear equations were compared to previously derived nonlinear equations [33-39], concluding that the recent equations in [41, 42] are the most comprehensive and accurate. It was also determined that chaotic motions may arise due to motion-limiting constraints. The chaotic and nonlinear behavior of constrained fluid-conveying pipes was further studied by Païdoussis and Semler [43] utilizing the full nonlinear equation of motion and a trilinear-spring to represent the impact constraints.

Copeland and Moon [44] investigated a hanging conveying cantilevered pipe with a mass attached at its free end. It was determined that chaotic motions arise for any non-zero mass attached to the free end but are not possible in the absence of the end-mass, as predicted in preceding models. The planar nonlinear equations of motion in [42] was modified, as part of a three-part investigation, by Wadham-Gagnon et al. [45] to account for three-dimensional motions of cantilevered pipes conveying fluid. The second part of the investigation by Païdoussis et al. [46] revised the model to account for the presence of constraints, such as a single or multiple springs positioned at a point along the length of the pipe. Modarres-Sadeghi et al. [47], in the final part of the study, investigated the three-dimensional behaviour of fluid-conveying pipes with an end mass attached at the free end. In another study, Modarres-Sadeghi et al. [48] investigated the same system with focus on two-dimensional and three-dimensional dynamics of horizontal and vertical cantilevered pipes at flow velocities past the Hopf bifurcation. Many studies have been performed on fluid-conveying pipes with particular interest in nonlinear dynamics, for instance the work by Sarkar and Païdoussis [49], Wang et al. [50], and Duan et al. [51].

1.3.2 Pipes aspirating fluid

The linear dynamics of pipes conveying fluid has been discussed in the preceding section with the assumption for cantilevered pipes that the flow is directed from the clamped end to the free end. The linear equations of motion for flexible pipes aspirating fluid are similar to those for a pipe discharging fluid with minor variations. In this section a brief literature review will be presented on aspirating pipes, with the flow directed from the free towards the clamped end, which are believed to require special treatment.

In the mid 1960s, Païdoussis [4] conducted the first experiment involving a vertically hanging cantilevered aspirating pipe immersed in water at the free end and connected to a pump at the other end. The pipe was found to remain stable for the range of flow velocities tested. Païdoussis and Luu [52], motivated by ocean mining applications, developed a model two decades later that predicted an aspirating pipe would lose stability via flutter at relatively low flow velocities and would regain stability beyond that point. This model considered the aspirating pipe to be identical to its counterpart pipe conveying fluid with the flow direction reversed. Païdoussis [53] modified the model by including suction at the free end, resulting in an equivalent negative pressurization equal to $-\rho U^2$ throughout the pipe, which was taken to be zero for the discharging pipe. In the presence of suction, the centrifugal force cancels out, and therefore the pipe cannot possibly flutter as was predicted by the earlier model. Furthermore, an experimental study was conducted, and the aspirating pipe remained stable, in accordance with the preceding model.

In later work, Kuiper and Metrikine [54] proposed that the pressure difference is a function of the geometry of the pipe at the free end, and it may range form $-\rho U^2$ to $-\frac{1}{2}\rho U^2$ and thus the centrifugal force remains. Additionally, the pipe may lose stability via flutter since the Coriolis force generates negative damping for aspirating pipes. In light of these findings, Païdoussis et al. [55] revised the model to include the following assumptions: (a) there is a small mean velocity “v” at the entrance of the pipe’s free end, whereas “U” denotes the flow velocity within the pipe; (b) there exists an additional mean tension at the pipe’s free end, determined by the flow at the inlet edge of the pipe via a parameter “γ”. An investigation was conducted where “v” remained vertical and the pipe was found to remain stable. In another case where “v” was tangential to the oscillating free end of the pipe, the pipe lost stability by flutter: however, the degree of agreement between experiments and theory was found to be highly dependent on the parameter “γ” and ratio “v/U”.

A few years later, Kuiper and Metrikine [56] proved experimentally, for the first time, that a partially submerged aspirating pipe can become unstable via flutter at adequately high flow velocities. A key aspect of those experiments was the partial immersion of the pipe in water, which reduced the hydrodynamic drag and encouraged initiation of flutter. In the unstable region, the pipe presented reciprocating phases, an orbital oscillation that is nearly periodic, and a noise-like oscillation. Moreover, the theories introduced earlier accurately predicted the dominant frequencies but not the critical flow velocity or behavior.

Several experiments were performed by Rinaldi [57] and Giacobbi [58] to eliminate two issues associated with water submerged aspirating pipes: (a) drag caused by surrounding water, which could dampen small oscillations; and (b) shell-type buckling collapse, which could occur near the clamped end of the pipe due to the large external-to-internal fluid pressure difference related to the aspiration process. The aspirating pipe was observed to oscillate at low flow velocities. Rinaldi [57] conducted more experiments to study the effect of different pipe materials and profile end-pieces on the dynamics. The behavior was, however, similar for all the end pieces considered, and it was concluded that the aspirating pipe's rms amplitude increased as flow velocity increased, whereas its first mode frequency remained almost constant. Furthermore, Païdoussis and Tétreault-Friend [59] demonstrated that a weak type of flutter can occur by comparing the aspirating pipe problem to that of aspirating sprinklers.

Giacobbi et al. [60] finally devised a model accounting for entry conditions at the free end of the pipe. Model predictions were found to be consistent with experiments when the inlet parameters were set within the limits suggested by CFD simulations. In addition, the model predicted loss of stability due to first-mode flutter with critical flow velocities similar to those found experimentally.

1.3.3 Cylinders in axial flow

The earliest work on cylinders in axial flow was conducted by Hawthorne [61], who was motivated by stability of the “Dracone” barge. The “Dracone” is a long towed flexible cylinder with tapered ends used in transporting liquids such as oil and fresh water which are less dense than the seawater surrounding it.

In a two-part study, Païdoussis extended Hawthorne’s simple model [62] and conducted an experimental investigation for the cylinder in axial flow subjected to different boundary conditions [63]. It was theoretically predicted and experimentally proven that the cylinder may lose stability by buckling in the first mode at sufficiently high flow velocities, followed by higher mode oscillatory instabilities. Païdoussis [64] extended his model further to study the stability of towed, fully submerged flexible cylinders. It was found that the cylinders are subjected to rigid-body instabilities at low towing speeds and flexural oscillatory instabilities at higher towing speeds.

The equation of motion derived in [62] contained an error related to the incorporation of the viscous forces and unfortunately the incorrect equations were utilized in multiple studies including the work by Orloff and Ives [65] and Pao [66]. Païdoussis [67] corrected the error in the original equations and later modified the equations to consider internal dissipation, gravity, pressurization, and confinement effects for both cantilevered and simply supported cylinders, which may be either isolated or a part of a cluster of identical cylinders [68]. It was found that, for an isolated cylinder, small flow velocities damp free motions, and at higher flow velocities a simply supported cylinder is subjected to first mode buckling followed by second mode buckling and coupled mode flutter with increasing flow velocity. Moreover, a cantilevered cylinder is subjected to first mode buckling followed by higher mode flutter with increasing flow velocity. Additionally, a cluster of cylinders was found to lose stability by the same instability types as the isolated cylinder, but at lower flow velocities. It was also found that increasing the degree of confinement has a significant effect on the instabilities. The predictions of the modified model [68] where found to be qualitatively similar to those of the original model [62] with some minor quantitative differences. However, the predictions of the modified model were significantly different from the original model for the case of very long systems such as the ones investigated by Orloff and Ives [65] and Pao [66]. A study by Païdoussis and Pettigrew [69] confirmed theoretically and experimentally that flexible cylinders in axial flow are significantly destabilized with increasing confinement. In another study Païdoussis et al. [70] found that a flexible cylinder in a narrow coaxial duct surrounded by annular flow is destabilized with increasing confinement; however, increasing confinement beyond some critical degree of confinement has a stabilizing effect.

Improved models and solution methods were developed to investigate the dynamics of towed slender cylinders due to their relation to multiple applications for instance towed acoustic cylinders which are employed in oil and gas exploration. Triantafyllou and Chryssostomidis [71] analytically determined the safe towing speed of a submerged slender cylindrical beam beyond which the beam is subjected to buckling. In another study Triantafyllou and Chryssostomidis [72] derived the equation of motion of a submerged long slender beam in axial flow, which is pinned at the upstream end and free at the other end. The equation of motion was utilized in determining the stability of a string, which is essentially a beam of negligible bending stiffness. It was determined that a towed string maybe stabilized if (a) the external tension at the free end is greater than aU^2, where "a" is the added mass of the beam cross section and "U" is the external flow speed; or (b) the length-to-diameter ratio is greater than $2C_f/\pi$, where C_f is the frictional coefficient of the string. Dowling [73,74], in a two-part study, investigated the dynamics of a neutrally buoyant, towed flexible cylinder in addition to a negatively buoyant, heavier than water cable. It was concluded that an acoustic streamer, which is modeled as a long thin towed flexible cylinder, is stable at all towing speeds.

It was found in a more recent study by de Langre et al. [75] that very long cylinders with a well-streamlined free end are subjected to both divergence and flutter, contrary to the predictions of the preceding models in [72,73]. Additionally, it was shown, through linear and non-linear dynamics, that flutter and divergence occur in the downstream region near the free end for both long and short cylinders. It was also determined that the form of instability is independent of the length of the cylinder. The type of instabilities observed in those studies were similar to those for hanging fluid-conveying pipes as found earlier by the work of Doaré and de Langre [76].

The first nonlinear model for towed cylinders was developed by Kheiri et al. [77] and an experimental investigation [78] was also conducted to justify the predictions of the nonlinear model in addition to the predictions of the previous linear model [79]. It was found that, if the tail-end of the towed cylinder is not blunt and if the towrope is short, then it is subjected to rigid-body instabilities at low flow velocities, followed by flexural instabilities at higher flow velocities. Moreover, a blunt tail-end allows the stabilization of the towed cylinder and the suppression of all instabilities for all towing speeds.

A cantilevered cylinder in axial air-flow directed from the free end to the clamped end was investigated theoretically and experimentally by Rinaldi and Païdoussis [80]. The cylinder was subjected to small amplitude first-mode oscillations at low flow velocities followed by buckling at higher flow velocities. Moreover, a linear model was developed and found to reasonably predict the dynamical behaviour [80]. The linear model was later improved by Rinaldi and Païdoussis [81] to account for the fluid-dynamic forces at the free-end of the cylinder in a more accurate way. The predictions of the amended model were comparable to those of the initial model in terms of instability type. However, the recent model predicted the critical flow velocities, for flutter and divergence, much better than the initial model.

This flow configuration (from free end to clamped end), also known as inverted flow, is utilized for thin cantilevered elastic plates, which are typically referred to as "flags". Inverted flags were found to be subjected to flutter at low flow velocities and the mechanism behind the oscillatory instabilities was discussed in multiple studies including that by Tavallaeinejad et al. [82].

Païdoussis et al. investigated for the first time the nonlinear dynamics of cantilevered cylinders in axial flow in a three-part study [83-85]. The first part of the study [83] was concerned with the experimental investigation of the dynamics of the system and it was found that cylinders with well-streamlined end lose stability due to divergence followed by second and third-mode flutter at higher flow velocities; however, cylinders with blunt free ends are not subjected to such instabilities. The nonlinear equation of motion for the system was derived in the second part [84], taking into consideration nonlinearities in the inviscid, viscous, and hydrostatic forces. The nonlinear equations were used in the third part [85] to study the nonlinear dynamics of the system and a comparison was made with the experimental results in [83]. The theoretical predictions were found to be in reasonable qualitative and quantitative agreement with the experimental results.

1.3.4 Pipes simultaneously subjected to internal and external axial flows

Cesari and Curioni [86] studied the problem of aspirating pipes subject simultaneously to external and internal flows theoretically, while Hannoyer and Païdoussis [5] studied the problem of a cantilevered pipe both experimentally and theoretically. In the latter, both internal and external flows are directed from the clamped end to the free end. It was determined that the dynamics of the cantilevered system is governed by the internal flow, and that it loses stability by flutter at sufficiently high flow velocities.

Païdoussis et al. [6], motivated by drill strings containing a fluid-powered drill-bit, investigated theoretically a system consisting of a vertical cantilevered pipe with internal flow running from the clamped end to the free end, and surrounded by a cylindrical container with a closed bottom. The cylindrical container served as a confinement for the pipe, and the fluid flowing around the pipe and out of the container was in the opposite direction to that in the pipe. It was found that the internal flow dominates the dynamics of the system for a wide annular region, whereas for narrower annuli, the external flow is dominant. Regardless of the size of the annulus, it was determined that the system would lose stability via flutter, but for narrower annular regions the critical flow velocities would be relatively lower, based on the parameters selected. Thereafter, Qian et al. [87], theoretically examined a reverse system through the inversion of the flows in both the pipe and cylindrical container, so that the pipe is aspirating, and the external flow is discharging. In this model, the flow at the free end of the pipe is regarded as a reverse jet rather than a sink flow as in an earlier model developed in Païdoussis et al. [55]. According to this study, for the parameters selected, aspirating pipes could lose stability through either flutter or divergence at high flow velocities.

Moditis et al. [12] developed a linear model for the system in which a cylindrical pressure vessel containing a vertical, downwards discharging pipe is surrounded by a shorter rigid tube forming an annulus with an upwards external flow. Essentially, this system represents the first mode of operation of solution-mined caverns discussed earlier. It was found that the discharging pipe could become unstable by either flutter or divergence at sufficiently high flow velocities, depending on the parameters of the system. The system in [12] was later studied theoretically by Abdelbaki et al. [88] in terms of a nonlinear dynamical model and experimentally by Chehreghani et al. [89]. It was found experimentally that the discharging pipe loses stability via second-mode flutter at sufficiently high flow velocity for low external-to-internal flow velocity ratios, i.e., U_o/U_i, whereas for higher flow velocity ratios the pipe is subject to static deformation followed by first-mode flutter and possibly second-mode flutter in some cases, depending on the system parameters. The predictions of the nonlinear model in [88] were found to be in reasonably good qualitative and quantitative agreement with the experimental results. Moreover, the predicted frequencies of oscillations of the nonlinear model were more reasonable than the linear model predictions [12].

Thereafter, Ge et al. [9], examined theoretically the reverse system through inversion of the flows in both the pipe and annulus, so that the pipe is aspirating and the external flow is discharging. It was assumed that the flow at the free end is a reverse jet, as in the study by Qian et al. [87]. Once again, it was concluded that the aspirating pipe could lose stability by flutter or divergence at high flow velocities, depending on the system parameters. Later, Butt [90] and Butt et al. [91] investigated experimentally the theoretical system studied by Ge et al. [9], finding that flutter is responsible for the loss of stability of the aspirating pipe at sufficiently high flow velocities. Additionally, Butt [90] investigated the effect of varying the length of the outer rigid tube for the system under consideration. Thereafter, Butt et al. [92] investigated the same system theoretically by modeling the internal flow as a plug flow, and the external flow using slender-body theory. It was found that the aspirating pipe loses stability at sufficiently high internal flow velocities primarily through first-mode flutter. The theory and experiments conducted by Butt et al. [91,92] were found to be in reasonably good agreement.

1.3.5 Leakage-flow-induced instabilities

Flexible structures subject to leakage flows experience fluid elastic instabilities. Leakage flow refers to a flow passing through narrow passages to wider regions and this flow does not necessarily have to be the main or only flow in the system; refer to Figure 1-4 (a). Some typical leakage flow passages are illustrated in Figure 1-4 (a). In some systems with narrow passages extending from end to end, the flow is referred to as annular flow. Several authors have studied leakage-flow-induced instabilities in the past, as such vibrations have been observed in various engineering applications, e.g., hydraulic gates, nuclear reactor components, and plug and check valves. However, the effect of leakage-flow-induced instabilities on the dynamics of solution-mined caverns has never been investigated before to determine their impact on the magnitude of oscillations and onset of instability.

Païdoussis [13] has briefly discussed some of the leakage flow related systems. The first time Païdoussis has experienced leakage flow was in the constant-flow part of the apparatus for an experiment dealing with flow in horizontal collapsible tubes. Moreover, Païdoussis [93] presented many cases of leakage-flow-induced vibrations occurring in real engineering systems. A particularly interesting case, which is somewhat representative of pipes subjected to external flows, is case 43 [93] dealing with a Pressurized Water Reactor (PWR). This case is representative of the leakage flow path illustrated in Figure 1-4 (a (i)). The system was modeled as a rectangular blade inserted in a water channel, which is narrow upstream and becomes wider downstream; refer to Figure 1-4 (a). The blade is pivoted at the downstream end and supported at two other points along the length of the blade. An additional constriction upstream exists due to the presence of upstream wear pads. It was concluded that the blade became unstable due to self-excited oscillations. Miller [94] proposed that the self-excited oscillations are flutter related to negative damping. This is best illustrated by considering the simplified version of the system; refer to Figure 1-4 (b). If the flow is directed from left to right and the blade is given an instantaneous velocity upwards, then the amount of water flowing in the upper portion of the channel shall decrease, whereas the flow in the lower portion of the channel shall increase. The instantaneous motion of the blade is comparable to localized valving effects, which results in decelerated flow in the upper portion of the channel and accelerated flow in the lower region. Moreover, the static pressure is also influenced, such that a momentary reduction in pressure in the upper subchannel and a momentary increase in the lower subchannel in comparison to the initial pressure levels is generated. Therefore, a net force in the upward direction is generated and the system extracts energy from the flow. This supports the conclusion regarding the possible existence of a negative damping instability, i.e., flutter, which should be more significant than the positive internal damping in the system. If the flow direction is reversed, i.e., right to left, the effect on the system should be reversed, such that the system would be stabilized.

Mulcahy [94] studied the same problem, but considering higher flow velocities and found that the frequency of vibration suddenly drops, and the system loses stability due to static divergence. However, it was proposed by Mulcahy that in general a constriction upstream of a narrow channel destabilizes the system, while a constriction at the downstream end has a stabilizing effect; this is a very valuable generalization. The reason for the instability is the pressure loss at the inlet of the flow passage due to the presence of the wear pads.

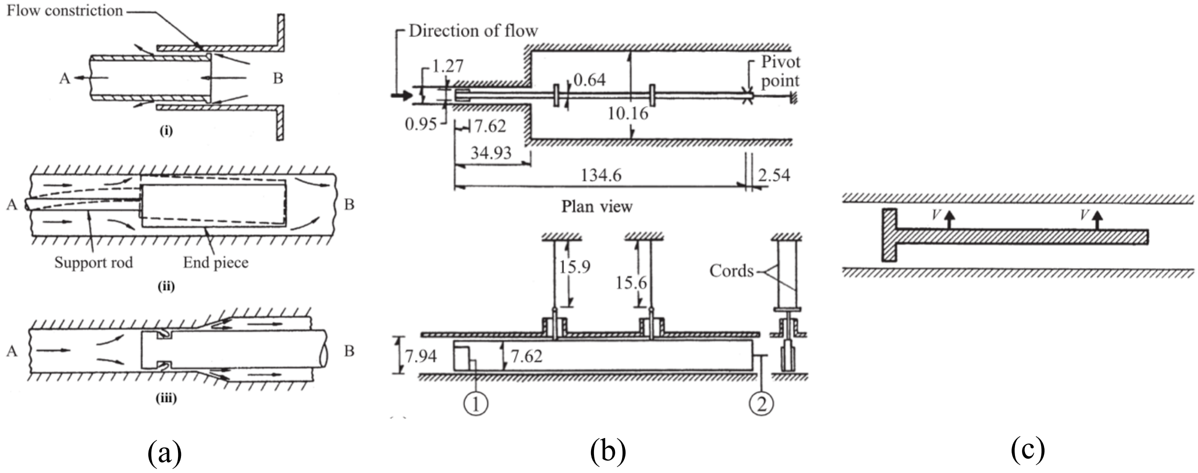

Figure 1-4: (a) Leakage flow passage types: (i) a tube-in-tube slip joint, (ii) a typical nuclear reactor control rod geometry, (iii) an Advanced Gas-Cooled Reactor (AGR) fuel channel; (b) pressurized water reactor component comprising a plate placed in a narrow channel; (c) an idealization of the system in (b) [13].

Mulcahy [95] investigated the system related to nuclear reactors control rods, in which the leakage flow path is similar to that illustrated in Figure 1-4 (a (ii)), but with a 90° clockwise rotation of the rod. It was found that if the central piece rotationally vibrates in a way similar to that illustrated by the dashed lines in Figure 1-4 (a (ii)), then the system may lose stability by flutter due to the existence of the local valving effect and the convergent/divergent flow regions. However, if the central piece is subjected only to transverse vibrations, and a downstream constriction is added, then the system may lose stability by divergence.

The third leakage flow path shown in Figure 1-4 (a (iii)) is a greatly idealized representation of a fuel channel in an Advanced Gas-Cooled Reactor (AGR). This system utilizes a finned ‘gag-bomb’ for blocking the flow for refueling, while the reactor is running. This system has a complex self-excitation mechanism as concluded by multiple authors including Païdoussis (case 52) [93], Mulcahy [97], and Hobson [98]. The complexity arises from the combination of the annular flow in the narrowest gap upstream of the system's diffuser, localized choking of the flow over the fins, the delay in restabilizing the flow causing a component of the fluid forces to be in phase with the gag velocity, and the flow in the diffuser.

Further investigations were conducted by Mateescu and Païdoussis [99] to analyze the stability in narrow annular channel and determine the fluid forces acting on the central body through inviscid flow theory, and later extended the work to include the viscous effects of a real fluid flow [100]. Mateescu et al. [101] experimentally studied the unsteady pressure field generated in a narrow annular passage. Mulcahy [102] and in a separate investigation Inada and Hayama [103,104] studied channels of different geometrical variations, for instance channels of diverging widths. It was found that diverging channels are subject to static divergence. Inada and Hayama [104,105] have analyzed the problem for a system taking into consideration translational and rotational vibrations (two degrees of freedom) and found that the system to be subjected to coupled mode flutter, even for a converging leakage flow channel.

1.4 Limitations of the studies in the literature

It is apparent from the literature review in the previous section that there are very few studies concerned with hanging cantilevered pipes subjected simultaneously to internal and external axial flows when compared to the enormous number of studies on pipes discharging and aspirating fluid as well as cylinders in axial flow. Moreover, a limited number of studies are available for pipes aspirating fluid, as compared to its counterpart of pipes discharging fluid.

Pipes subjected simultaneously to internal and reverse external axial flows are expected to be governed by some dynamical combination of the separate systems consisting of fluid-conveying pipes and cylinders in axial flow; however, no studies have focused on determining whether the internal or external flow dominates the dynamics. Additionally, the influence of system parameters, such as annular gap size, eccentric positioning of the rigid tube relative to the central pipe, and a constriction at the inlet/outlet of the outer rigid tube, on the onset of instability for various external to internal flow velocity ratios has not been investigated. The studies in the past have considered systems with very large annular gaps, i.e., a small degree of external flow confinement, and in two separate studies an annular gap of diameter twice that of the outer pipe diameter.

1.5 Research objectives

The present research is concerned with the dynamics of a vertically cantilevered aspirating pipe subjected to reverse external annular flow over its upper portion. The main purpose of this research is to investigate the influence of various parameters on the onset of instability and post-instability dynamical behaviour of the system for various external-to-internal flow velocity ratios, U_o/U_i. The parameters studied include annular gap size, pipe length, eccentric positioning of the rigid tube relative to the central pipe, and a constriction at the inlet/outlet of the outer rigid tube According to the literature review, the dynamics of this system, in particular concerning the aspirating pipe, is not adequately understood; however, it is important, because of its relation to applications in the oil and gas industry and particularly the hydrocarbon storage mode in solution-mined caverns. Hence, learning more about the dynamics of this system, as discussed earlier, will be a significant step in preventing catastrophic accidents. For a better understanding of the overall dynamical behaviour of this system, it is essential to first work on determining whether the internal or external flow dominates the dynamics of the system. The experimental objectives of this thesis may be summarized as follows:

- exploring the effect of a wider annular gap on the stability and dynamical behaviour of an aspirating cantilevered pipe simultaneously subjected to a reverse partially confined external axial flow; the external flow is constrained by a rigid tube positioned coaxially with respect to the pipe.
- examining the effect of pipe length on the stability and dynamical behaviour of the system.
- studying the effect of an eccentrically positioned rigid tube with respect to the aspirating pipe on the stability and dynamical behaviour of the system.
- investigating the difference in frequency of oscillations at the tip of the aspirating pipe and at a region within the rigid tube (near the free end).
- exploring the influence of flow separation, i.e., external flow passing from a very narrow gap to a significantly wider gap over the upper portion of the pipe or from a wider region to a narrower region, on the stability and dynamical behaviour of the system.

1.6 Thesis structure

This thesis consists of four chapters including Chapter 1, the introductory chapter. The content of the remaining chapters is briefly described in what follows.

Chapter 2 describes the experimental setup utilized in the current investigation, including the apparatus, flexible pipe, plexiglas tube, eccentricity plate, and constriction rings. Additionally, the experimental methodology, data acquisition, and data analysis processes are described. Finally, two experiments carried out to examine the independent effects of the external and internal flows are discussed to give a better understanding of the dynamics of the system prior to the discussion of the parametric study results.

The experimental results for the system comprising a hanging cantilevered pipe aspirating fluid and simultaneously subjected to a partially confined external axial flow in the reverse direction due to the addition of a cantilevered plexiglas tube over the upper portion of the pipe, are presented in Chapter 3. The current investigation is a parametric study focused on the effect of the following parameters on the dynamics of the system: (i) annular gap size, (ii) eccentric position of the plexiglas tube with respect to the flexible pipe, (iii) pipe length, (iv) flow separation (constriction at the cantilevered or free end of the rigid tube). Furthermore, a brief comparison between modal frequencies detected within the rigid tube and at the tip of the pipe is included.

In Chapter 4, a summary of the experimental findings and the conclusions reached are presented, followed by a short description of possible future work.

Chapter 2 : Experimental apparatus and methods

2.1 Experimental Apparatus

The apparatus used in this investigation is a scaled down idealized model representing the operations of solution-mined caverns. A bench-top-size apparatus was used, consisting of a water filled cylindrical pressure vessel with four plexiglas windows, which allow easy viewing of and access to the interior of the vessel. The inner diameter and length of the vessel are approximately 0.48 and 0.61 meters respectively. Hence, the volume of the vessel is roughly 0.11 cubic meters. In addition, a flexible pipe and a rigid plexiglas tube are vertically cantilevered inside the vessel.

Flexible pipes made of different materials were utilized in the current investigation, namely Silastic RTV and Santoprene rubber. The Silastic pipes are a castable two-part liquid silicone-rubber. Details on the casting process may be found in [57]. The mechanical and geometrical properties of the different pipes utilized are summarized in Table 2-1. The first-mode frequency in air for the silicone-rubber pipes is 1.09 Hz, and 2.10 Hz for the Santoprene pipe. The theoretical natural frequencies of the various pipes are summarized in Table 2-2 based on the models developed in [12,90,92]. Moreover, it is considered that the effect of structural damping on the dynamics of the system is negligible in comparison to that of fluid damping (due to pipe immersion in water). Nevertheless, interested readers are referred to Rinaldi [57] for typical logarithmic decrement values for the silicone-rubber. The pipes are cantilevered inside the pressure vessel using a hollow male adapter which is fitted into the inner hollow region of the pipes, and then screwed to the ceiling of the vessel.

It is worth mentioning that pipe III, prior to length reduction, was of the same length as pipe I, with the same flexural rigidity and frequency values as pipe I.

Table 2-1: Mechanical and geometrical properties of the flexible pipes. *EI*: flexural rigidity, *m*: mass per unit length, *L*: length, D_i: inner diameter, D_o: outer diameter.

Pipe	I	II	III
Material	Silicone-rubber	Santoprene	Silicone-rubber
EI [N m^2]	7.37x10^{-3}	37.3x10^{-3}	7.37x10^{-3}
m [kg m^{-1}]	1.97x10^{-1}	0.86x10^{-1}	1.97x10^{-1}
L [mm]	441	443	221
D_i [mm]	6.35	9.50	6.35
D_o [mm]	16.0	13.0	16.0

Table 2-2: Theoretical natural frequencies in water of the flexible pipes based on the models in [12,90,92]. f_1: first-mode frequency, f_2: second-mode frequency; f_3: third-mode frequency, f_4: fourth-mode frequency.

Pipe	I	II	III
Material	Silicone-rubber	Santoprene	Silicone-rubber
f_1 [Hz]	0.31	1.01	1.42
f_2 [Hz]	2.90	6.50	9.59
f_3 [Hz]	7.24	17.89	26.17
f_4 [Hz]	13.60	34.99	51.12

The pipe is surrounded coaxially by a rigid plexiglas tube of diameter D_{ch} = 54 mm and length L', forming an annular region over its upper portion. The rigid tube is pressure fitted into a plastic adapter which is screwed to the ceiling of the pressure vessel. The ratio of the length of the rigid tube, L', to the length of the pipe, L, is denoted by r_{ann}. A rigid tube of length L' = 200 mm is utilized for the experiments with pipes I and II and a shorter rigid tube of length L' = 100 mm is used for the experiments with pipe III (shorter pipe). Therefore, the value of r_{ann} is fixed at approximately ½ for all experiments, to facilitate comparison between the different combinations of pipes and rigid tubes.

The average pressure inside the vessel is measured using a Bourdon tube pressure gauge, installed on the bleed lines connected to the top of the pressure vessel. Throughout this investigation, the pipe and tube were submerged within the pressure vessel, as verified by opening the manual bleed valve. Moreover, the valves connected to the bleed lines allow the extraction of air from the pressure vessel. The described system is shown in Figures 2-1 and 2-2 (a).

Figure 2-1**:** Photograph of the experimental apparatus with pipe I and a rigid tube of Length L' = 200 mm. 1- Pressure vessel, 2- Flexible pipe, 3- Plexiglas tube, 4- Flowmeters, 5- Storage tank, 6- Electric pump.

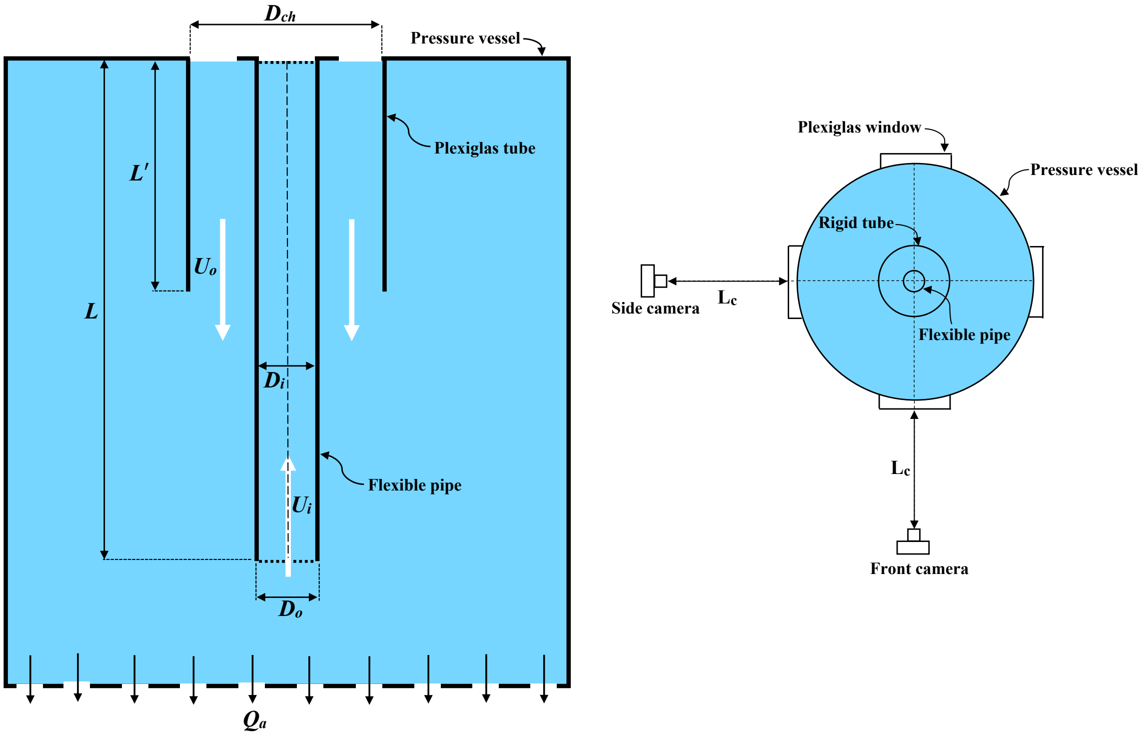

(a) (b)

Figure 2-2**:** (a) Schematic diagram showing the flow configuration utilized for hydrocarbon storage in solution-mined caverns; (b) schematic of a sectional top view of the apparatus with the dual camera system.

The fluid is introduced into the system by flowing downward through the annular region, with flow velocity U_o. Thereafter, the fluid is discharged from the pressure vessel by flowing through the flexible pipe with flow velocity U_i upwards. Additionally, fluid may be discharged through outlet holes at the bottom of the vessel to achieve higher U_o/U_i ratios. The amount of flow discharged at the bottom of the pressure vessel is controlled by outlet valves.

A 2.2 kW (3 HP) electric impulse pump draws water from a storage tank, located near the pressure vessel, to provide the external flow, i.e., flow in the annulus. The gain of the pump is controlled using a digital controller. For elevated U_o/U_i ratios, flow is discharged from the bottom of the pressure vessel with a volumetric flow rate Q_a. By continuity, when $Q_a = 0$, then $U_o/U_i =$

0.015 for the silicone-rubber pipes (pipes I and III) and $U_o/U_i = 0.033$ for the Santoprene pipe (pipe II). To achieve higher values of U_o/U_i, additional fluid must be discharged from the bottom of the pressure vessel, i.e., $Q_a \neq 0$. The maximum flow rate achieved using the apparatus is limited by the maximum pressure the vessel can endure without leaking, which is around 30 psi ($\simeq 205$ kPa).

2.2 Data acquisition

Two magnetic flow meters are used to display the external and internal flow rates in the annulus and the pipe, indicated in L/s. The additional discharged flow Q_a may be determined from $Q_a = Q_o - Q_i$. Afterwards, the internal flow velocity U_i and external flow velocity U_o may be directly computed from the known geometry of the system.

The motion of the pipe is visualized by tracking the centroid of a 38 mm long 'red marked' region, near the free end of the pipe, using two orthogonally positioned cameras. The dual camera system is composed of two identical FLIR® Grasshopper3 2.3 MP cameras, which are externally triggered using a function generator to ensure synchronization. The cameras are leveled at the same height and located equidistant from the free end of the pipe, as depicted in Figure 2-2 (b).

The 'red marked' portion of the flexible hanging pipe is set as the focal point of both cameras to simplify the post-processing of recorded videos, which are recorded at 64 frames per second for a duration of 180 seconds. The marked portion is detected in each processed frame and later tracked in the following frames. By utilizing the pixel location of the centroid of the marked portion of the pipe in each captured frame, as well as the knowledge of the pipe outer diameter, it is possible to calculate the displacement of the pipe.

2.3 Experimental methodology

The experiments were initially designed to examine the effect of external flow confinement, specifically the diameter of the outer rigid tube, on the dynamics of the system under consideration for several external to internal flow velocity ratios. In the present experiments, an outer rigid tubes of diameter D_{ch} = 54 mm and D_{ch} = 27 mm were used, and the results were compared to those in Butt et al. [90], in which a similar system with a rigid tube of diameter D_{ch} = 31.5 mm was utilized.

The experimental procedure is described briefly in the following steps:

1. The flexible pipe and Plexiglas tube are hung vertically inside the pressure vessel.
2. The two magnetic flow meters are plugged in to display the flow rate entering the system through the rigid tube and the flow rate exiting the system through the pipe.
3. The storage tank is filled with water, and then the pressure vessel is fully filled using the pump.
4. The apparatus is left running for a few minutes to guarantee that the vessel is pressurized and that the trapped air is bled out through the bleed line connected at the top of the vessel.
5. The dual camera system and lights near the cameras are turned on. The two cameras are set to record at 64 frames per second for 180 seconds, and the recording is started once the function generator is turned on to ensure synchronization.
6. For each U_o/U_i ratio investigated, the gain of the pump is controlled such that the flow velocity in the annular region, i.e., U_o, was increased stepwise. Additionally, the outlet valves are opened to extract the additional flow from the bottom of the vessel for the cases where $Q_a \neq 0$. The gain of the pump and the outlet valves influence each other and hence they are adjusted until the desired flow velocities are achieved.

7. The system is kept running at each flow velocity step to attain steady state, then the recording is started once the function generator is turned on to ensure synchronization. At each flow velocity step, a video is recorded by each camera and transmitted to the nearby computer through a USB 3.0 connection cable.

2.3.1 Eccentricity experimental setup

A set of experiments was designed to examine the effect of an eccentrically positioned rigid tube with respect to the central flexible pipe and the pressure vessel on the dynamics of the system under consideration. A square plate approximately 150 mm wide by 150 mm long and 13 mm tall was screwed to the ceiling of the pressure vessel in place of the rigid tube adapter; refer to Figure 2-3. The plate facilitates the attaching of the rigid tube adapter at some offset degree or displacement with respect to the centerline of the hanging pipe and pressure vessel in any direction. The allowed displacements, denoted by "t_{gap}", are 4,8,10, and 14 mm and were chosen to be towards the front camera and the pressure vessel's front window for consistency; refer to Figure 2-4 (a). Moreover, the investigation in the current study was only concerned with displacements of 10 and 14 mm, which required the removal and turning of the plate by 180 degrees so that the displacement is always toward the front Plexiglas window. The steps are the same as described earlier once the plate, rigid tube, and pipe are clamped inside the vessel as shown in Figure 2-4 (b).

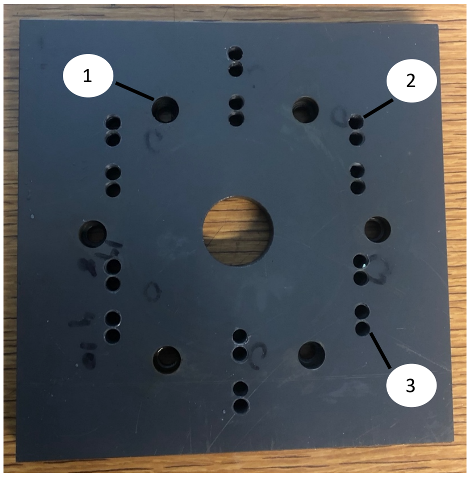

Figure 2-3: Photograph of the eccentric square shaped plate of dimensions: L: 150 mm x W:150 mm x H: 13 mm. 1- screw location to attach plate to the ceiling of the pressure vessel, screw location to attach the rigid tube adapter to the plate with an offset of 2- “t_{gap} =14 mm”, or 3- “10 mm”.

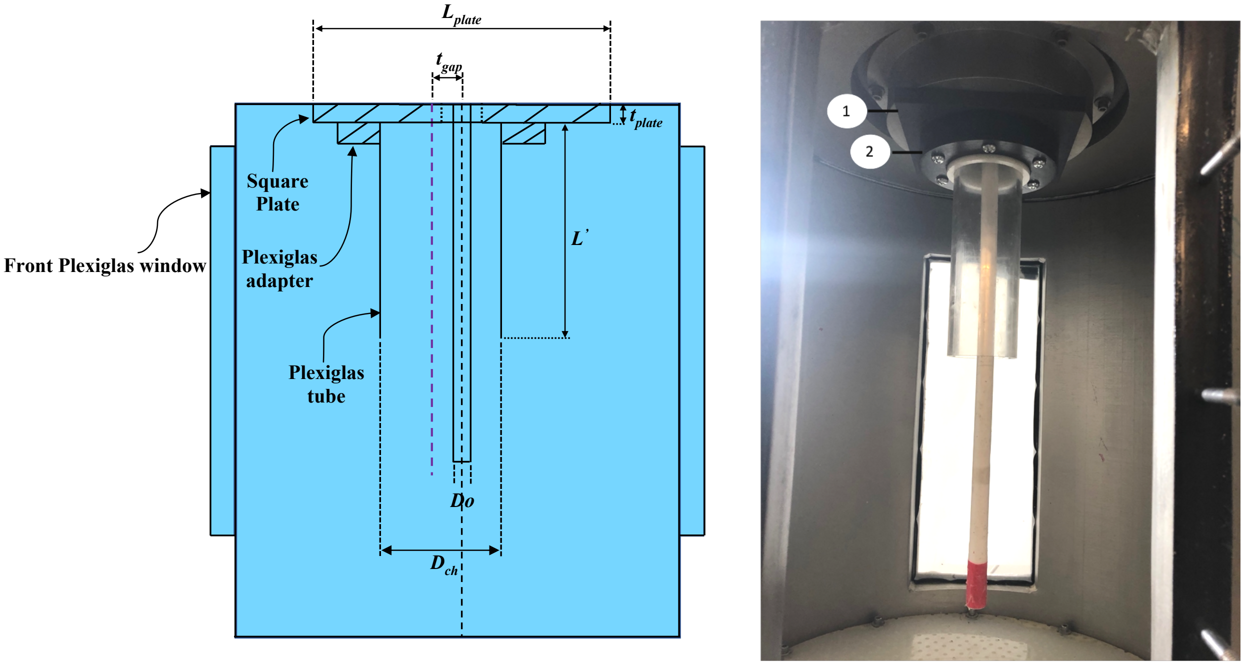

(a) (b)

Figure 2-4: (a) Schematic diagram showing the displacement of the rigid tube with respect to the pipe and pressure vessel. (. . .) Centerline of the rigid tube, (. . .) centerline of the pipe and vessel. (b) Photograph of the eccentric plate and rigid tube adapter inside the vessel. 1- eccentric plate, 2- rigid tube adapter.

2.3.2 Flow separation experimental setup

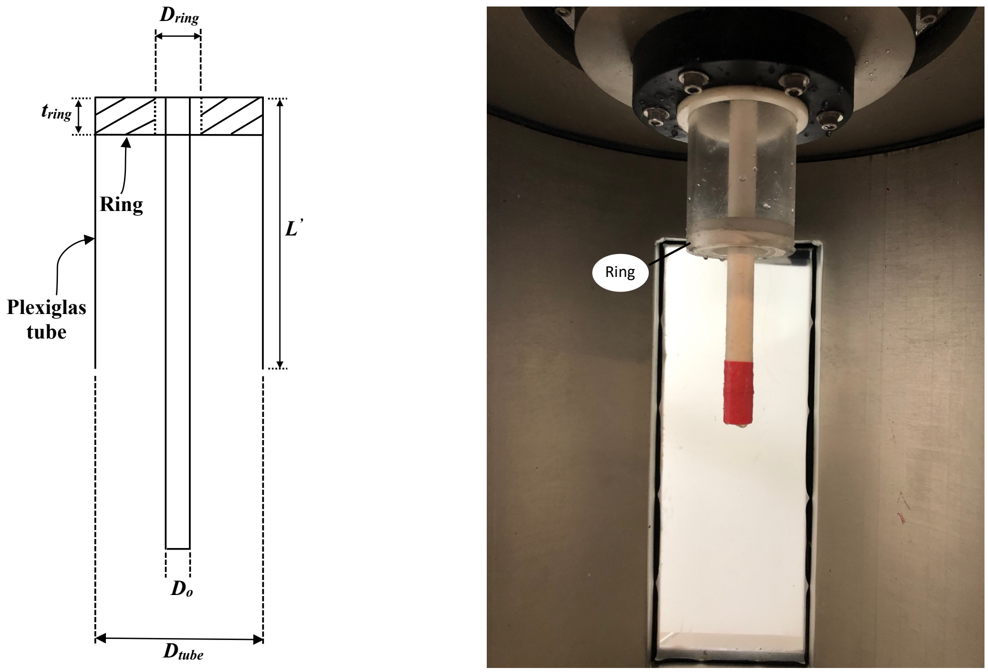

(a) (b)

Figure 2-5: (a) Schematic diagram showing the top location of the flow separation ring with respect to the inlet of the rigid tube and pipe; (b) Photograph of the ring of inner diameter D_{ring} = 32 mm at the outlet of the rigid tube.

Another set of experiments was designed to investigate the effect of flow separation on the dynamics of the system through the addition of a constriction at the inlet or outlet of the rigid tube. These particular modifications were chosen based on the work done for comparable systems – refer to section 1.3.5. The flow configuration under consideration is expected to be destabilized for an inlet constriction and the effect should be reversed for a constriction at the outlet of the rigid casing. The objective of the current investigation is to verify those predictions experimentally as a step towards the potential improvement in the design of solution-mined caverns.

A "ring" shaped piece is pressure fitted at the inlet of the rigid tube, such that the external flow passes through a narrow passage to the wider region confined by the outer rigid tube; refer to

Figure 2-5(a). Furthermore, a ring may be placed at the outlet of the rigid tube such that the flow passes from a wider passage to a narrower one; refer to Figure 2-5(b). The “ring” has an outer diameter equal to the diameter of the channel, D_{ch}, and an inner diameter and thickness, denoted by D_{ring} and t_{ring} respectively. Rings of various inner diameters were tested, and it was found that a reasonably narrow passage or a sufficiently severe constriction is required to induce a leakage flow instability, as will be discussed in later sections. The steps are the same as described earlier, once the ring, rigid tube, and pipe are mounted inside the vessel as shown in Figure 2-5(a,b).

2.4 Data analysis

At each flow velocity step, two videos were recorded using the synchronized front and side cameras. The recorded videos from the two cameras were subsequently fed into an image processing MATLAB script to compute displacement time series. The initial undeformed position of the pipe at $U_i = 0$ served as a reference. Further analysis was conducted, and the raw time series data is also used to obtain other characteristics of the motion, such as bifurcation diagrams, phase portraits, and power spectral density functions (PSDs).

It is worth mentioning that the bifurcation diagrams in the following sections will be presented in both dimensional (bottom x-axis) and dimensionless (top x-axis) flow velocities as illustrated in Figure 2-(a,b) to facilitate comparison to subsequent experimental and theoretical results. The conversion factors utilized are through

$$u_i = \left(\frac{\rho_f A_i}{EI}\right)^{\frac{1}{2}} L U_i, \; u_o = \left(\frac{\rho_f A_o}{EI}\right)^{\frac{1}{2}} L U_o, \tag{2.1}$$

where ρ_f is the density of the fluid, $A_i = \frac{1}{4}\pi {D_i}^2$, and $A_o = \frac{1}{4}\pi {D_o}^2$; EI, D_i, and D_o were defined earlier in the caption of Table 2-1. Additionally, the dimensionless frequency is represented as follows:

$$\omega = \left(\frac{m+\rho_f A_i+\rho_f A_o}{EI}\right)^{\frac{1}{2}} L^2\, \Omega \qquad (2.2)$$

where $\Omega = 2\pi f$ is the radian frequency, m is the mass per unit length of the pipe, and f is the frequency in Hertz.

2.5 Dependence of the dynamics of the system on external and internal flows

The current experimental investigation and past studies have been concerned with determining the onset of instability for various U_o/U_i ratios. The experiments were carried by varying internal and external flow velocities stepwise while the U_o/U_i remained constant. Therefore, a combined effect, due to the simultaneous variation of the internal and external flows, was observed.

Two experiments were conducted, using pipe I and the rigid tube of length L' = 200 mm, to better understand the isolated effect of external and internal flows on the system under consideration, prior to discussing the effect of varying the system parameters. An attempt to isolate the effects of the two flows was accomplished by keeping one flow velocity constant while varying the other flow velocity; hence, each step will be representative of a different flow velocity ratio as illustrated in Figure 2-6(a,b).

The case with a constant U_i demonstrated that the system becomes independent of U_o at values of U_o greater than 0.25 m/s, as demonstrated by the almost constant oscillatory component of the amplitude in Figure 2-7(a). A value of U_o = 0.25 m/s is equivalent to U_o/U_i = 0.46. Moreover, the experiment with U_o as a constant, demonstrated the same external flow velocity independence, as illustrated by the approximately constant rms amplitude for U_o/U_i greater than 0.20 in Figure 2-6(b). Therefore, it is possible to conclude that for high U_o/U_i ratios the dynamics is independent of the external flow velocity.

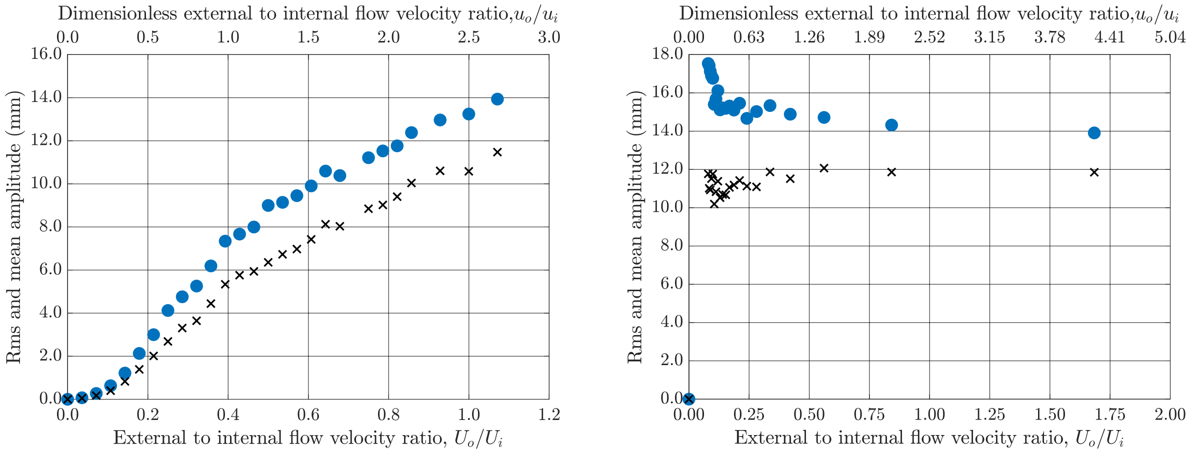

(a) (b)

Figure 2-6: Bifurcation diagrams illustrating rms and mean amplitudes of oscillation versus external to internal flow velocity U_o/U_i. (a) $U_i = 0.538$ m/s (constant); (b) $U_o = 0.532$ m/s (constant). (●) Total displacement; (×) mean displacement component (pipe I).

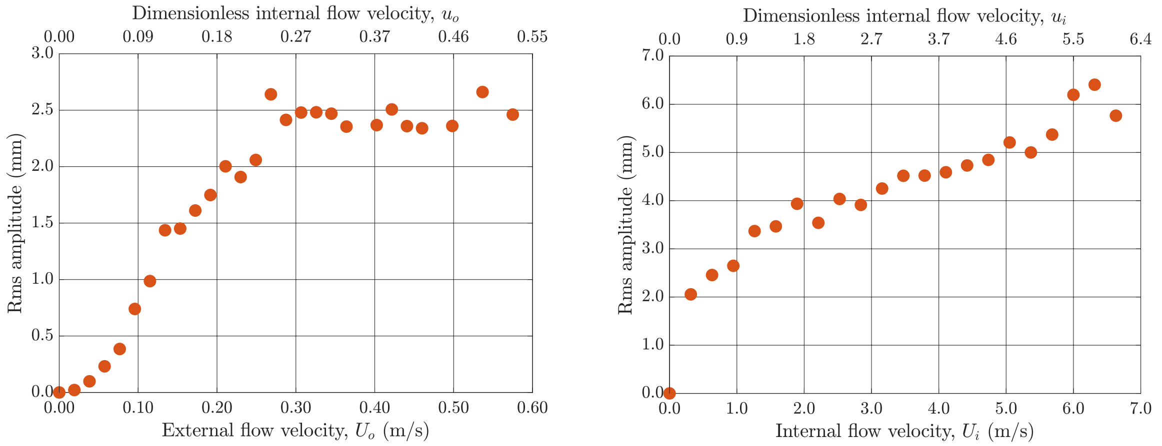

(a) (b)

Figure 2-7: Bifurcation diagram illustrating rms amplitudes of oscillation versus (a) external flow velocity U_o (U_i fixed at 0.538 m/s); (b) internal flow velocity U_i (U_o fixed at 0.532 m/s). (●) Oscillatory displacement component (pipe I).

Chapter 3 : Experimental investigation of a partially confined aspirating pipe subjected to a reverse external axial flow

In this chapter the experimental results of the parametric study concerning the dynamics of a cantilevered aspirating pipe subjected to a partially confined reverse external axial flow will be presented. Results of the parameters examined will be presented in the following order: annular gap size, eccentrically positioning the rigid tube relative to the central flexible pipe, pipe length, and flow separation through the addition of a constriction (constriction at cantilevered end, and then at the free end). At the end of the eccentricity section a brief discussion regarding the modal frequencies within the rigid tube will be discussed and compared to those detected at the tip of the pipe.

In the following sections, the dimensional to dimensionless flow velocity conversion factors utilized are: (i) $u_i = 0.914U_i$ and $u_o = 2.303U_o$ for pipe I, (ii) $u_i = 0.611U_i$ and $u_o = 0.836U_o$ for pipe II, and (iii) $u_i = 0.458U_i$ and $u_o = 1.154U_o$ for pipe III – refer to Chapter 2 for the formulation. Dimensionless flow velocities are used to allow an impartial comparison between the various flexible pipes utilized in the current investigation.

3.1 Experimental results for annular gap size for a coaxial rigid tube of length $L' = 200$ mm

In this section, results of the experiments conducted using pipes I and II with a plexiglas tube of diameter $D_{ch} = 54$ mm and length $L' = 200$ m are presented. The U_o/U_i ratios investigated have demonstrated two different dynamical behaviours, for different flow velocity ratios. Therefore, the experimental results are sorted into two ranges, namely low ($U_o/U_i = 0.015 – 0.060$) and high ($U_o/U_i = 0.20 – 0.80$) flow velocity ratios for pipe I. The results are compared to the experiments conducted in Butt [90] and Butt et al. [91] for a rigid tube of $D_{ch} = 31.5$ mm, as well as the recent experiments conducted for a very narrow rigid tube of $D_{ch} = 27$ mm.

In the case referred to as the basic geometry case, there is no additional fluid discharged from the bottom of the pressure vessel, i.e., $Q_a = 0$, and $U_i A_i = U_o A_{ch}$ by continuity. These two ‘base’ cases represented by $U_o/U_i = 0.015$ for $D_{ch} = 54$ mm and $U_o/U_i = 0.055$ for $D_{ch} = 31.5$ mm are discussed first.

3.1.1 Results for low flow velocity ratios (pipe I)

Results for $U_o/U_i = 0.015$ and $U_o/U_i = 0.055$ ($Q_a = 0$)

The bifurcation diagrams showing the rms amplitude of oscillations versus U_i for $U_o/U_i = 0.015$ ($D_{ch} = 54$ mm) and $U_o/U_i = 0.055$ ($D_{ch} = 31.5$ mm) are shown in Figure 3-1(a,b), respectively.

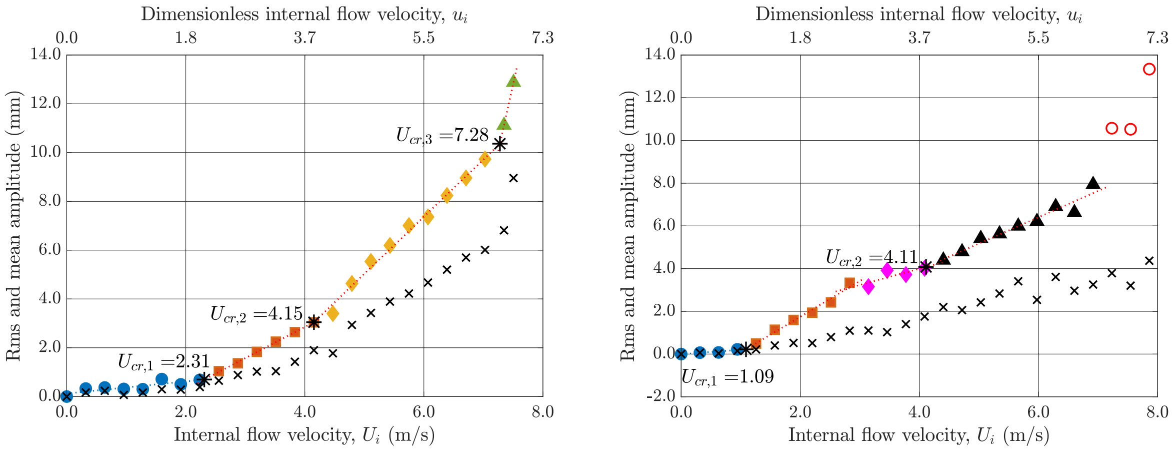

(a) (b)

Figure 3-1: Bifurcation diagrams illustrating rms and mean amplitudes of oscillation versus internal flow velocity U_i (or dimensionless internal flow velocity u_i). (a) $U_o/U_i = 0.015$ ($D_{ch} = 54$ mm); (b) $U_o/U_i = 0.055$ ($D_{ch} = 31.5$ mm). Rms amplitude: (●) pre-instability, (■) post-instability 1, (◆) post-instability 2, (▲) post-instability 3; (∗) critical flow velocity; (○) impacting; (◆) plateau; (▲) post-instability 2; (×) mean deformation ($Q_a = 0$, pipe I).

For U_o/U_i = 0.015, motions of very small amplitude were observed at low internal flow velocities, as seen in Figure 3-1(a). At such low internal flow velocities, no dominant frequency was observed, and hence these weak motions were attributed to turbulence. As U_i was further increased to a value of 1.92 m/s ($u_i = 1.76$), a dominant frequency $f_1 \simeq 0.42$ Hz, pertaining to weak first-mode oscillations of the pipe, was detected in the PSD. Moreover, the oscillations increased in amplitude thereafter, as reflected by the steeper increase in rms amplitude, and it is considered that the pipe lost stability via first-mode flutter at $U_i = 2.31$ m/s ($u_i = 2.11$).

In the region referred to as 'post-instability 1', the dominant frequency remained around $f_1 \simeq 0.43$ Hz; however, at $U_i = 3.51$ m/s ($u_i = 3.21$) a second-mode frequency $f_2 \simeq 2.43$ Hz of very weak power appeared in the PSD, in addition to the pre-existing dominant first-mode frequency; refer to Figure 3-2(a). The oscillations observed were representative of mixed-mode oscillations, namely first-mode oscillations with a superimposed weak second-mode frequency component. At $U_i = 4.15$ m/s ($u_i = 3.79$), a steeper increase in rms amplitude was observed, and this flow velocity is considered to be the threshold of another instability, denoted by $U_{cr,2}$; refer to Figure 3-1(a). As U_i is increased further, the first-mode frequency remained dominant around $f_1 \simeq 0.43$ Hz with slight variations, while the second-mode frequency increased in power with U_i. At $U_i = 7.28$ m/s ($u_i = 6.66$), which is referred to as the third critical velocity, i.e., $U_{cr,3}$, the steepest increase in rms amplitude began, as depicted in Figure 3-1(a). The second-mode frequency appeared significant in terms of power at $U_i = 7.35$ m/s ($u_i = 6.72$); refer to Figure 3-3(a).

The dynamical behaviour of the pipe in regions with high amplitude oscillations, i.e., 'post-instability 2' and 'post-instability 3', was analyzed further using time series, polar, and phase portrait plots. In general, the dynamical behaviour of the aspirating pipe was found to be unsteady and chaotic. However, there are two distinctive and repetitive behaviours observed beyond the second and third critical points. At U_i = 3.51 m/s (u_i = 3.21), the oscillations were almost periodic with a small chaotic and expanding component, as shown in Figure 3-2(b-d). Increasing U_i further, the behaviour was found to be increasingly chaotic with a substantial expansion component; refer to Figure 3-3(b-d).

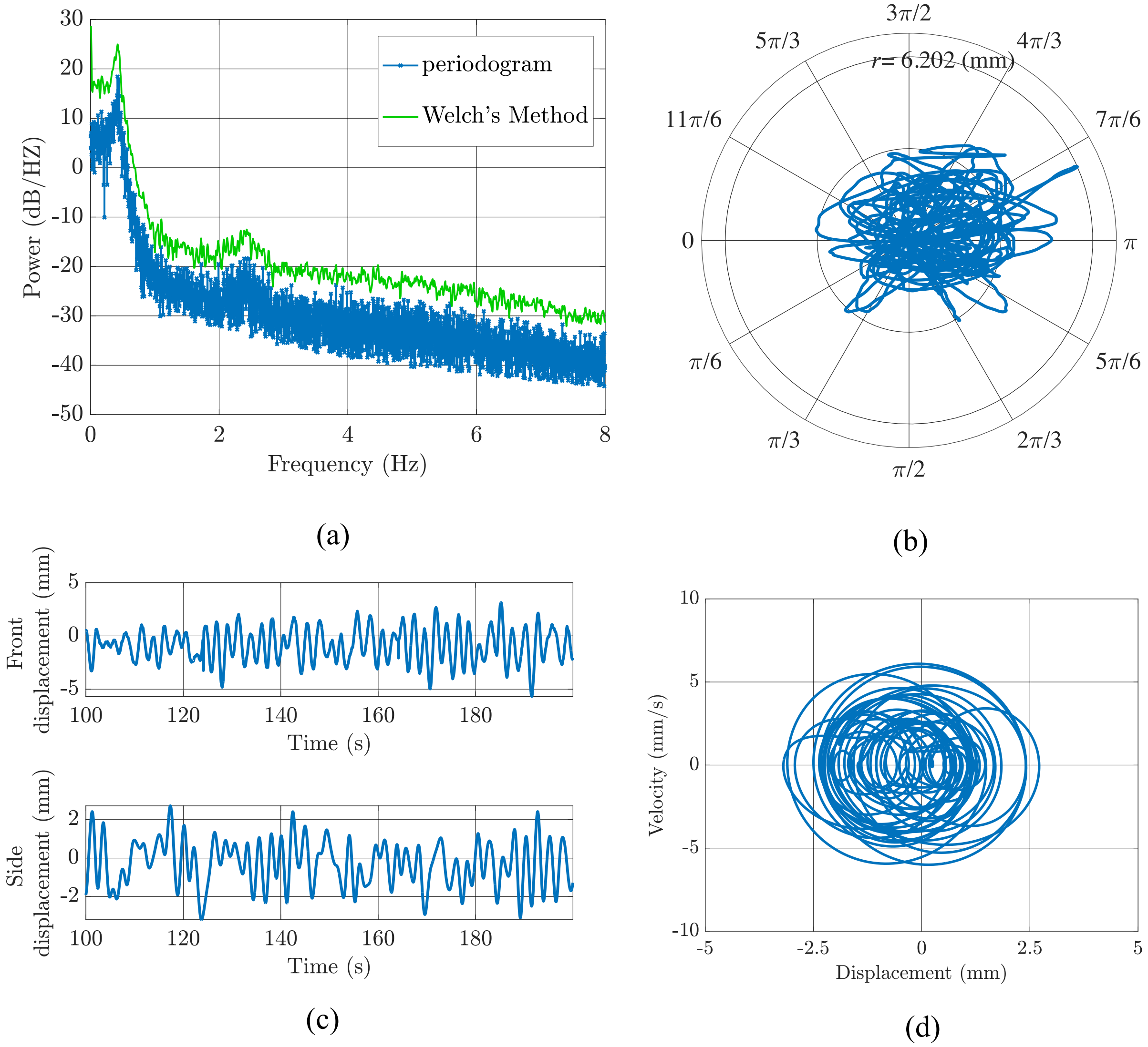

Figure 3-2: (a) PSD; (b) polar plot; (c) time series; (d) displacement-velocity phase portrait (side camera) at U_i = 3.51 m/s (u_i = 3.21) for U_o/U_i = 0.015 and D_{ch} = 54 mm (pipe I).

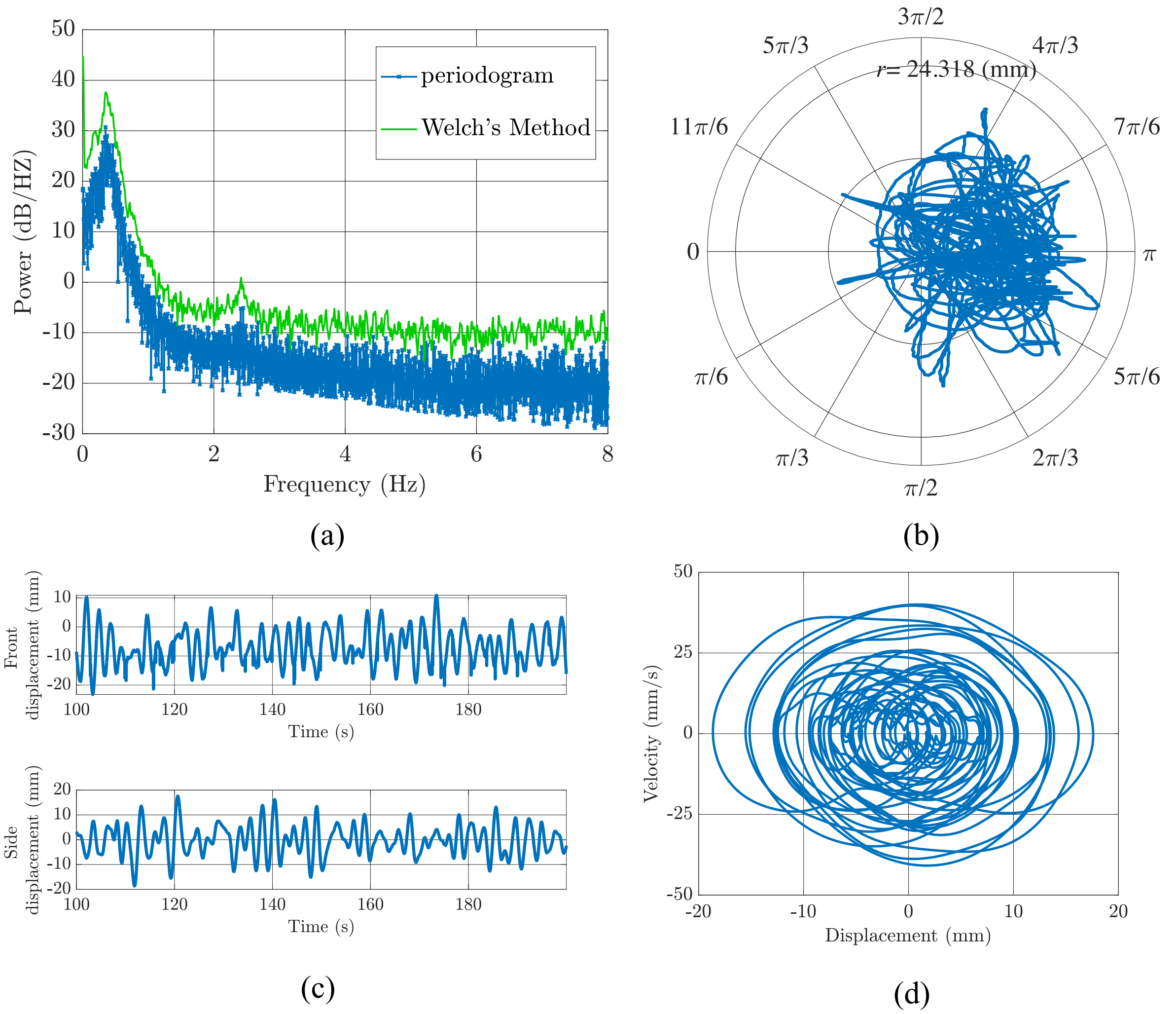

(a) (b) (c) (d)

Figure 3-3: (a) PSD; (b) polar plot; (c) time series; (d) displacement-velocity phase portrait (side camera) at $U_i = 7.35$ m/s ($u_i = 6.72$) for $U_o/U_i = 0.015$ and $D_{ch} = 54$ mm (pipe I).

For $U_o/U_i = 0.055$ ($D_{ch} = 31.5$ mm) in Butt et al. [91], the overall behaviour is qualitatively similar to that for $U_o/U_i = 0.015$, in terms of increasing trends in rms amplitudes, except for the plateau referred to as ‘region 3’ in Figure 3-4(a). In view of the more detailed attention paid in the present study to the dynamics of the system at low internal flow velocities U_i, the results presented in [91] for $D_{ch} = 31.5$ mm were missing a few points at low U_i, which pretrain to the pre-instability region. Therefore, experiments have been repeated for a rigid tube of $D_{ch} = 31.5$ mm, for some

U_o/U_i ratios, to allow for a fair comparison to the current experimental results with regards to the onset of instability; refer to Figure 3-1(b) and Figure 3-8(c,d).

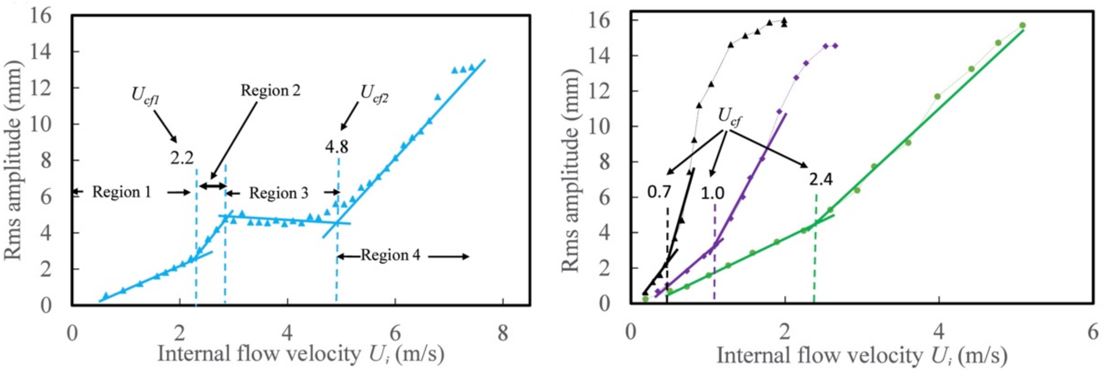

(a)

(b)

Figure 3-4: Bifurcation diagram illustrating rms amplitudes of oscillation versus internal flow velocity U_i. (a) $U_o/U_i = 0.055$; (b) $U_o/U_i = 0.10 – 0.40$. Rms amplitude: (▲) $U_o/U_i = 0.055$, (●) $U_o/U_i = 0.10$, (◆) $U_o/U_i = 0.20$, (▲) $U_o/U_i = 0.40$; U_{cf}: Critical flow velocity (Butt [89] and Butt et al. [91] for $D_{ch} = 31.5$ mm).

Two frequencies were observed in [91] in the plateau region, the first being the first-mode frequency of the pipe, i.e., f_1, and the second being a ½ order subharmonic of f_1. Frequency f_1 was dominant for the lower U_i values in the plateau region, but as the flow velocity increased further, a signal power exchange between the two frequencies was noted. The signal powers of the two frequencies were found to be almost equal towards the end of the plateau at $U_i = 4.11$ m/s ($u_i = 3.76$). Thereafter, in region 4, the ½ order subharmonic was found to be dominant. The PSDs presented in Butt et al. [91] illustrated the presence of another frequency, $f \simeq 2.5$ Hz, but it was not discussed, as it was of relatively low power in the range of internal flow velocities considered. This frequency has also been observed in the recent experiments and it corresponds to the second-mode frequency for $U_o/U_i = 0.015$ ($D_{ch} = 54$ mm). Impacting of the pipe on the lower rim of the rigid tube was also noted and can be seen in the bifurcation diagram through the crowding of the points in the proximity of $U_i = 7$ m/s ($u_i = 6.40$); refer to Figures 3-1(b) and 3-4(a).

Results for $U_o/U_i = 0.03$ and 0.06 ($D_{ch} = 54$ mm)

Two experiments were conducted for $U_o/U_i = 0.03$ and 0.06 to test whether the dynamical behaviour observed for $U_o/U_i = 0.015$ would persist. The dynamical behaviour was found to be qualitatively similar to that for $U_o/U_i = 0.015$ up to the region referred to as "Post-instability 2". The rate of increase in amplitude diminishes beyond the third critical flow velocity, $U_{cr,3}$, as depicted in Figure 3-5(a,b). Moreover, the first-mode frequency component continued being predominant.

For $U_o/U_i = 0.03$, a third-mode frequency, $f_3 \simeq 6.72$ Hz, of very weak power, appeared in the PSD at $U_i = 4.79$ m/s ($u_i = 4.38$) in addition to the pre-existing dominant first-mode frequency and the weaker second-mode frequency. Furthermore, the signal power of the second-mode frequency was found to be significant, i.e., over 0 dB/Hz at $U_i = 4.79$ m/s ($u_i = 4.38$), and its strength increased nearly sixfold in the proximity of $U_i = 6.71$ m/s ($u_i = 6.13$). The signal power of the third-mode frequency remained relatively insignificant for the range of flow velocities examined.

The bifurcation diagram for $U_o/U_i = 0.06$ showed a similar behaviour to that for $U_o/U_i = 0.03$, with regards to the less steep increase in rms amplitude in the region referred to as "Post-instability 3", and a qualitatively similar behaviour to both $U_o/U_i = 0.015$ and 0.03 in preceding regions. The diminishing rate of increase in rms amplitude was also accompanied by a third-mode frequency $f_3 \simeq 6.92$ Hz of very weak power, which appeared in the PSD in addition to the pre-existing frequencies, i.e., f_1 and f_2, observed in the lower U_o/U_i cases. The signal power of the second-mode frequency was found to be significant, i.e., over 0 dB/Hz at U_i = 2.55 m/s (u_i = 2.33), and its strength was about 30 times greater in the proximity of U_i = 6.38 m/s. On the other hand, the signal power of the third-mode frequency remained relatively insignificant at the maximum attainable flow velocity value of U_i = 6.71 m/s (u_i = 6.13); refer to Figure 3-6(a).

The dynamical behaviour of the pipe in regions with high amplitude oscillations, i.e., in 'post-instability 3', was analyzed further using time series, polar, and phase portrait plots for U_o/U_i = 0.06. The dynamical behaviour is qualitatively comparable to that for U_o/U_i = 0.015; however, the magnitude of oscillations was higher for U_o/U_i = 0.06, as demonstrated by the increasingly chaotic and substantially expanding component at U_i = 6.71 m/s (u_i = 6.13); refer to Figure 3-6(b-d).

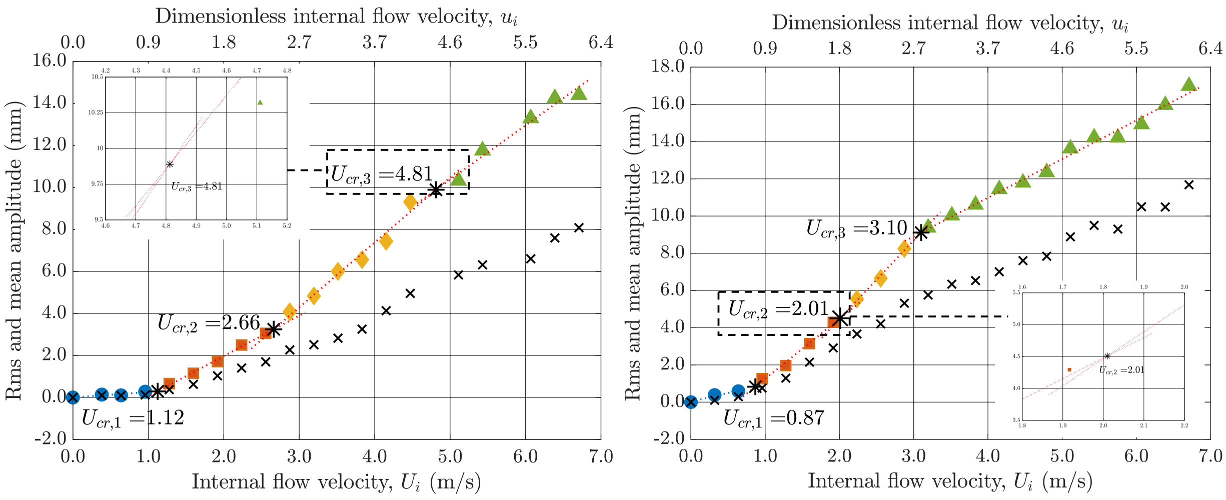

(a) (b)

Figure 3-5: Bifurcation diagrams illustrating rms and mean amplitudes of oscillation versus internal flow velocity U_i (or dimensionless internal flow velocity u_i). (a) U_o/U_i = 0.03; (b) U_o/U_i = 0.06. Rms amplitude: (●) pre-instability, (■) post-instability 1, (◆) post-instability 2, (▲) post-instability 3; (∗) critical flow velocity; (×) mean deformation (pipe I, D_{ch} = 54 mm).

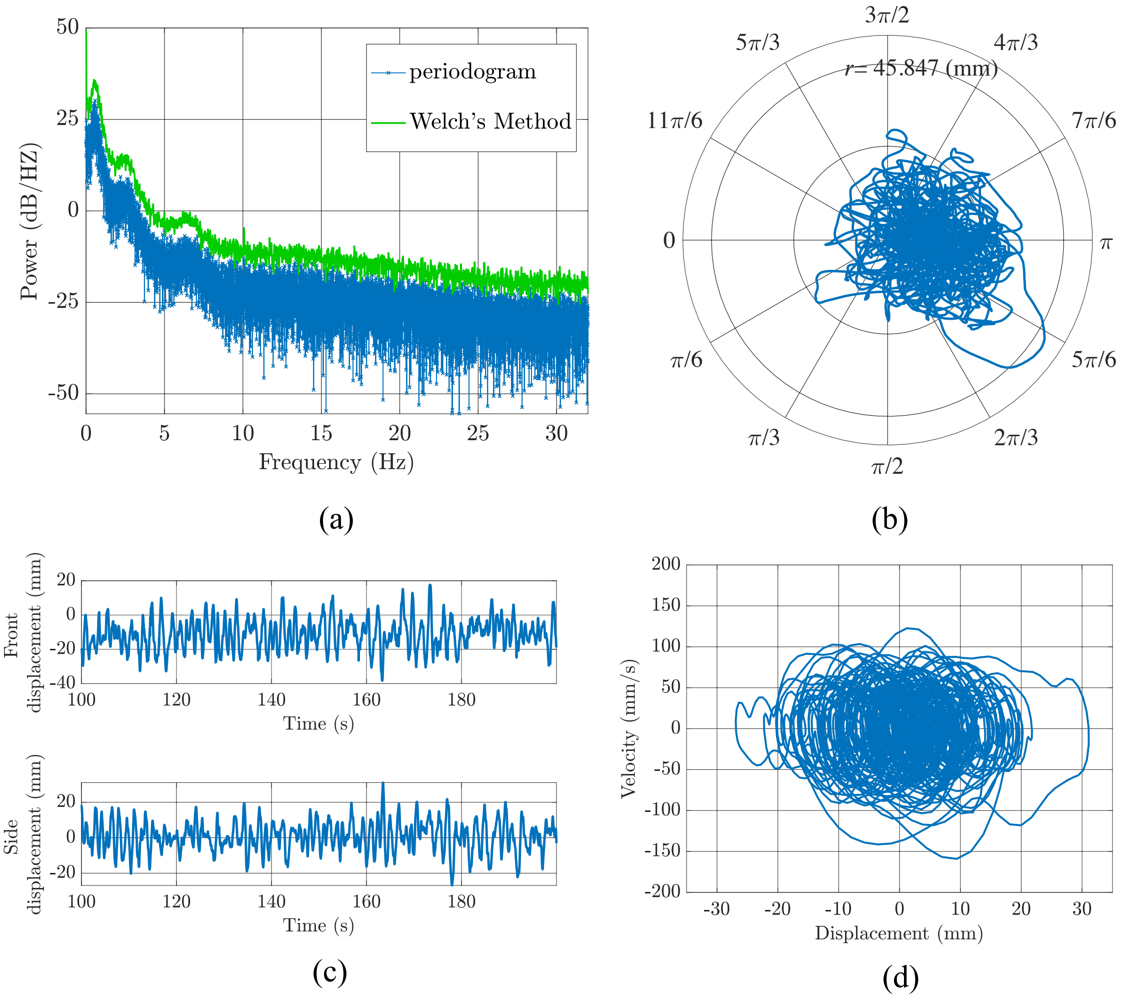

(a) (b)

(c) (d)

Figure 3-6: (a) PSD; (b) polar plot; (c) time series; (d) displacement-velocity phase portrait (side camera) at $U_i = 6.71$ m/s ($u_i = 6.13$) for $U_o/U_i = 0.06$ and $D_{ch} = 54$ mm (pipe I).

Based on the PSDs and visual observations, the mixed-mode oscillations became more prominent with increasing U_o/U_i ratios from 0.015 to 0.06. Furthermore, the pipe lost stability at relatively lower critical flow velocities as the U_o/U_i ratio was increased. For instance, the critical flow velocities were decreased from $U_{cr,1} = 2.31$ m/s ($u_i = 2.11$), to 0.87 m/s ($u_i = 0.80$), $U_{cr,2} = 4.15$ m/s ($u_i = 3.79$), to 2.01 m/s ($u_i = 1.84$), and $U_{cr,3} = 7.28$ m/s ($u_i = 6.66$) to 3.10 m/s ($u_i = 2.83$) as the U_o/U_i ratio was increased from 0.015 to 0.06. This reduction in critical flow velocity was accompanied by an evident reduction in the size of the regions in the bifurcation diagrams. It is also worth mentioning that the third mode component is almost unnoticeable in the PSDs for U_o/U_i = 0.03, as compared to those for U_o/U_i = 0.06. In all low U_o/U_i cases, the first-mode frequency remains dominant and almost constant at an average value of $f_1 \simeq 0.45$ Hz with increasing internal flow velocity, as shown in Figure 3-7(a).

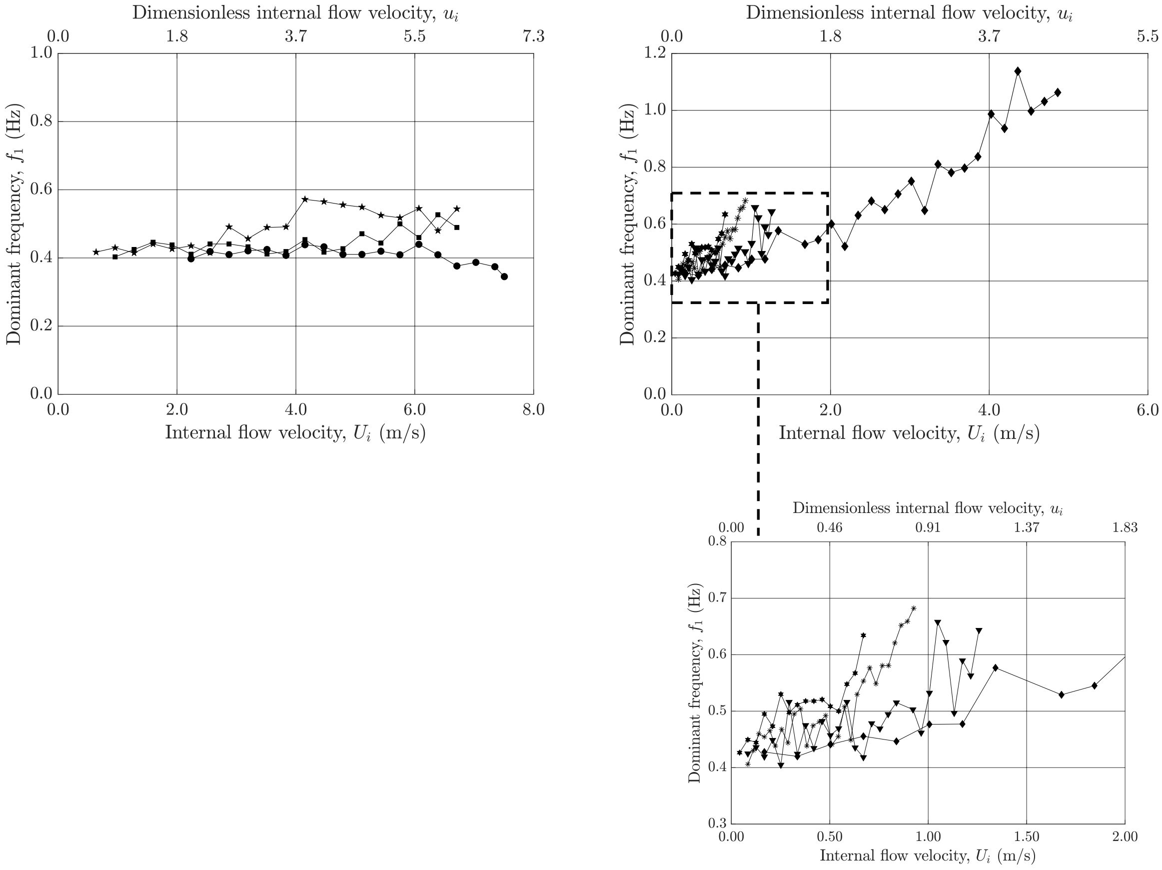

(a)

(b)

Figure 3-7: Dominant first mode frequency, f_1 versus internal flow velocity, U_i (or dimensionless internal flow velocity u_i). (a) low U_o/U_i ratios; (b) high U_o/U_i ratios. (●) $U_o/U_i = 0.015$, (■) $U_o/U_i = 0.03$, (★) $U_o/U_i = 0.06$, (◆) $U_o/U_i = 0.20$; (▼) $U_o/U_i = 0.40$; (∗) $U_o/U_i = 0.60$; (✱) $U_o/U_i = 0.80$ (pipe I, D_{ch} = 54 mm).

3.1.2 Results for high flow velocity ratios (pipe I)

Further experiments were conducted for higher U_o/U_i ratios with the wider rigid tube (D_{ch} = 54 mm), specifically U_o/U_i = 0.20 - 0.80. The higher U_o/U_i ratios demonstrated a different dynamical behaviour from that for the low U_o/U_i range discussed earlier. In terms of bifurcation diagram trends, a short pre-instability region was followed by a single steeper increase in rms amplitude, then the amplitude increased further at a diminished rate similar to the "Post-instability 3" region for U_o/U_i = 0.03 and 0.06; refer to Figures 3-8(a,c) and 3-9(a,b). The PSDs show a dominant first mode frequency with superimposed weaker second and third-mode frequencies, as for U_o/U_i = 0.03 and 0.06. However, the signal power of the second and third-mode frequencies were relatively amplified as compared to the lower U_o/U_i ratios, and an additional weaker fourth-mode frequency was observed. Furthermore, higher vibrational modes had a lower signal power as compared to lower vibrational modes, i.e., power of $f_1 > f_2 > f_3 > f_4$. The critical flow velocities were observed to decrease with increasing flow velocity ratio. Moreover, the value of the first-mode dominant frequency increased with increasing internal flow velocity; refer to Figure 3-7(b). Details related to each one of the specific U_o/U_i ratios will be presented in what follows.

Results for U_o/U_i = 0.20 and 0.40

For U_o/U_i = 0.20, a different behaviour was observed as compared to lower flow velocity ratios; refer to Figure 3-8(a). A single steep increase in magnitude of oscillations was determined, where the rms amplitude grew almost up to 10 mm in the "Post-instability 1" region, as compared to nearly 3 mm for U_o/U_i = 0.06. The pipe lost stability via first mode flutter at U_i = 0.24 m/s (u_i = 0.22). At the beginning of "Post-instability 1", a weak second-mode frequency component was observed in the PSD but was insignificant until the flow velocity was increased to U_i = 0.84 m/s

($u_i = 0.77$), whereas the third-mode frequency was detected towards the end of "Post-instability 1" and became significant at around $U_i = 2.35$ m/s ($u_i = 2.15$). Hence, the steep increase in amplitude past the second critical flow velocity may be due to the dominant first-mode frequency with superimposed weaker second and third-mode frequency components. By the end of "Post-instability 2", both second and third-mode frequencies had increased their signal strength with increasing flow velocity, such that f_2 has increased 20 times and f_3 nearly tenfold. Additionally, a weak fourth-mode frequency component appeared in the PSDs in the vicinity of $U_i = 3.19$ m/s ($u_i = 2.92$), but remained negligible in terms of power for the range of flow velocities examined; refer to Figure 3-10(a). In light of the significant increase in signal power of all frequency components at high flow velocities, further analysis is required to better characterize the motion. Time traces from the front and side cameras along with the scattered pattern in the Poincaré map all support the unsteady and chaotic nature of the motions – refer to Figure 3-10(b,c). Furthermore, the polar plot, phase portrait from the side camera, and three-dimensional trajectory, in Figure 3-10(d-f), suggest the existence of a somewhat 3D periodic motion with a relatively stronger expanding component as compared to lower flow velocity ratios. Additionally, the phase plane plot is full all the way to the origin, i.e., far from a clean paradigmatic limit cycle, backing the characterization of the oscillations as unsteady and intermittent.

For $U_o/U_i = 0.40$, qualitatively, the same behaviour as in $U_o/U_i = 0.20$ was observed, with regards to bifurcation diagram and PSDs – refer to Figure 3-8(b). The pipe lost stability by first mode flutter at $U_i = 0.11$ m/s ($u_i = 0.10$) and the second-mode frequency became notable at $U_i = 0.37$ m/s ($u_i = 0.34$). For the third-mode frequency, it materialized toward the end of "Post-instability 2", whereas the fourth-mode frequency was detected but remained insignificant as U_i was increased. The same phenomenon occurred for higher flow velocity ratios, but the critical flow velocities were reduced with increasing U_o/U_i ratios. The aspirating pipe was found to lose stability at very low critical flow velocities, i.e., nearly zero, for $U_o/U_i = 0.60$ and 0.80. For instance, the onset of instability is 0.09 m/s ($u_i = 0.08$) and 0.07m/s ($u_i = 0.06$) for $U_o/U_i = 0.60$ and 0.80, respectively.

Recently, experiments were conducted with the narrow rigid tube ($D_{ch} = 31.5$ mm) for $U_o/U_i =$ 0.20 and 0.40. For the narrower rigid tube, the rms amplitude was found to increase at two distinct ascending rates for both $U_o/U_i = 0.20$ and 0.40, as illustrated in Figures 3-4(b) by Butt et al. [91] or in Figure 3-8(c,d). Moreover, the mean deformation component of the oscillations was found to form a plateau at around 2 mm at sufficiently high flow velocities for $U_o/U_i = 0.20$ and 0.40 with the narrow rigid tube – refer to Figure 3-8(c,d).

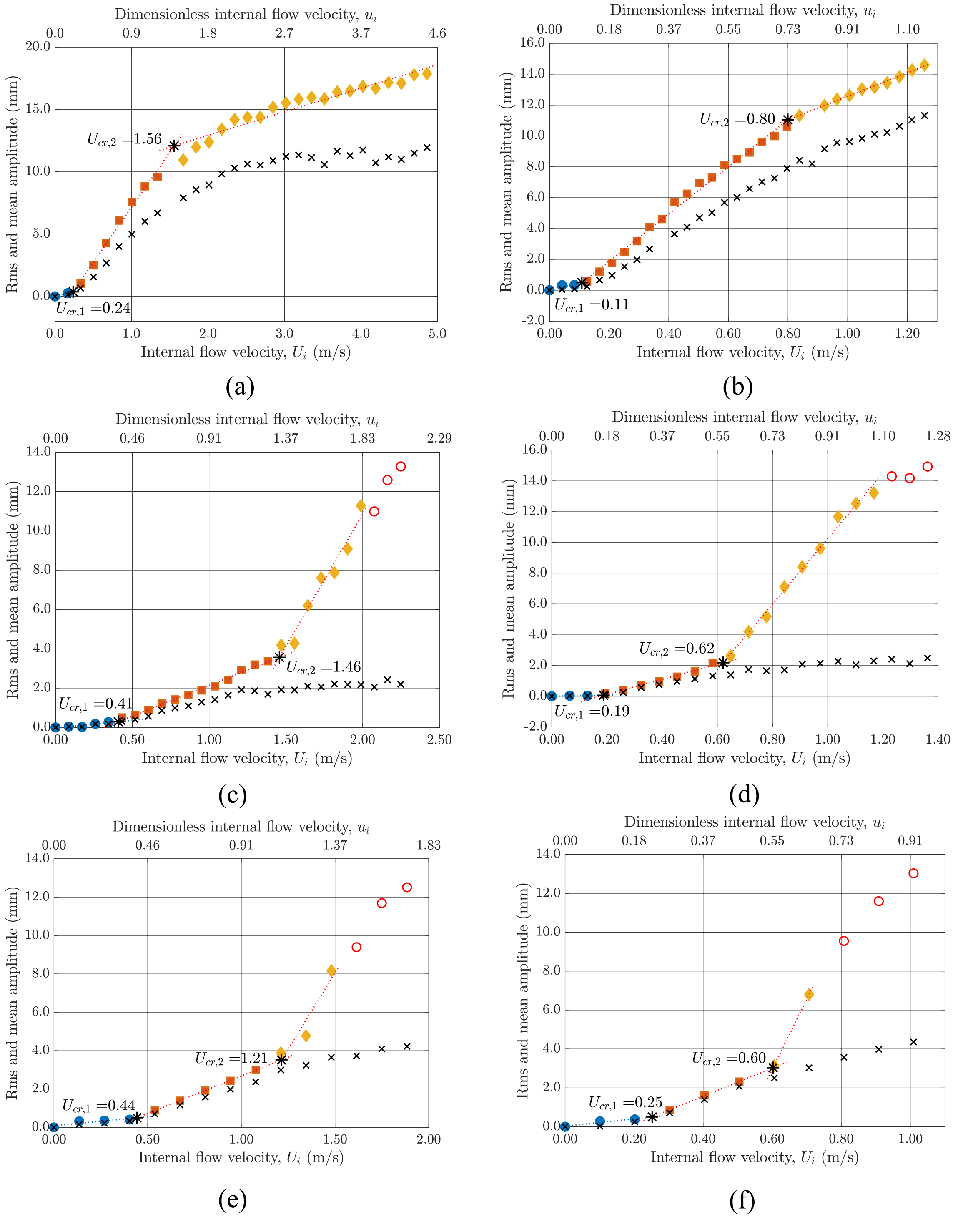

Figure 3-8: Bifurcation diagrams illustrating rms and mean amplitudes of oscillation versus internal flow velocity U_i (or dimensionless internal flow velocity u_i). (a) $U_o/U_i = 0.20$ ($D_{ch} = 54$ mm); (b) $U_o/U_i = 0.40$ ($D_{ch} = 54$ mm); (c) $U_o/U_i = 0.20$ ($D_{ch} = 31.5$ mm); (d) $U_o/U_i = 0.40$ ($D_{ch} = 31.5$ mm); (e) $U_o/U_i = 0.20$ ($D_{ch} = 27$ mm); (f) $U_o/U_i = 0.40$ ($D_{ch} = 27$ mm). Rms amplitude: (●) pre-instability, (■) post-instability 1, (◆) post-instability 2; (∗) critical flow velocity; (○) impacting; (×) mean deformation (pipe I).

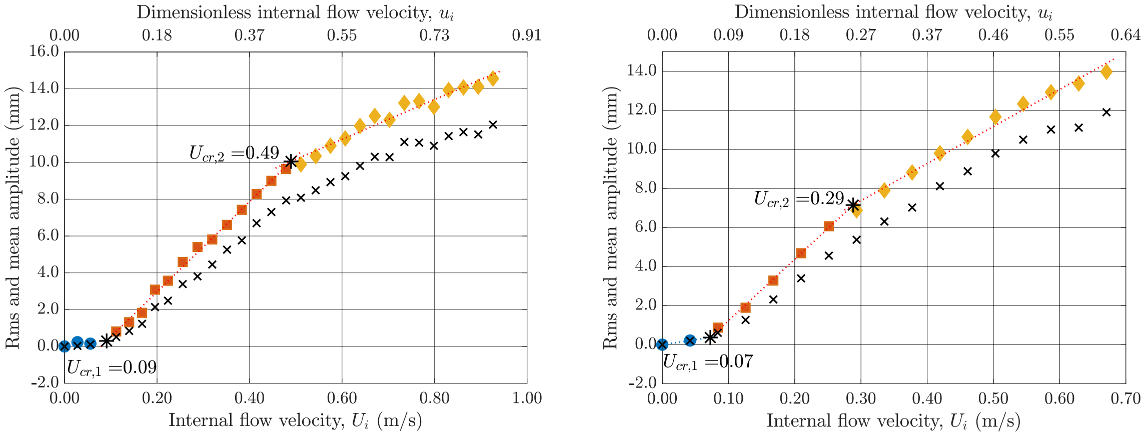

(a) (b)

Figure 3-9: Bifurcation diagrams illustrating rms and mean amplitudes of oscillation versus internal flow velocity U_i (or dimensionless internal flow velocity u_i). (a) $U_o/U_i = 0.60$; (b) $U_o/U_i = 0.80$. Rms amplitude: (●) Pre-instability, (■) Post-instability 1, (◆) Post-instability 2; (∗) Critical flow velocity; (✕) Mean deformation (pipe I, D_{ch} = 54 mm).

The onset of instability in dimensional form, i.e., $U_i = U_{cr}$, for each U_o/U_i investigated is summarized in Table 3-1 and in dimensionless format, i.e., $u_i = u_{cr}$, in Table A-1 to facilitate comparison between the two different annular gap sizes. The pipe was found to lose stability at lower critical flow velocities as U_o/U_i ratios increased, regardless of the annular gap size. Additionally, the first critical flow velocity was relatively higher for the narrow rigid tube as compared to the narrower one for comparable U_o/U_i ratios, i.e., 0.20 and 0.40. However, the reverse pattern was observed for the second critical flow velocity.

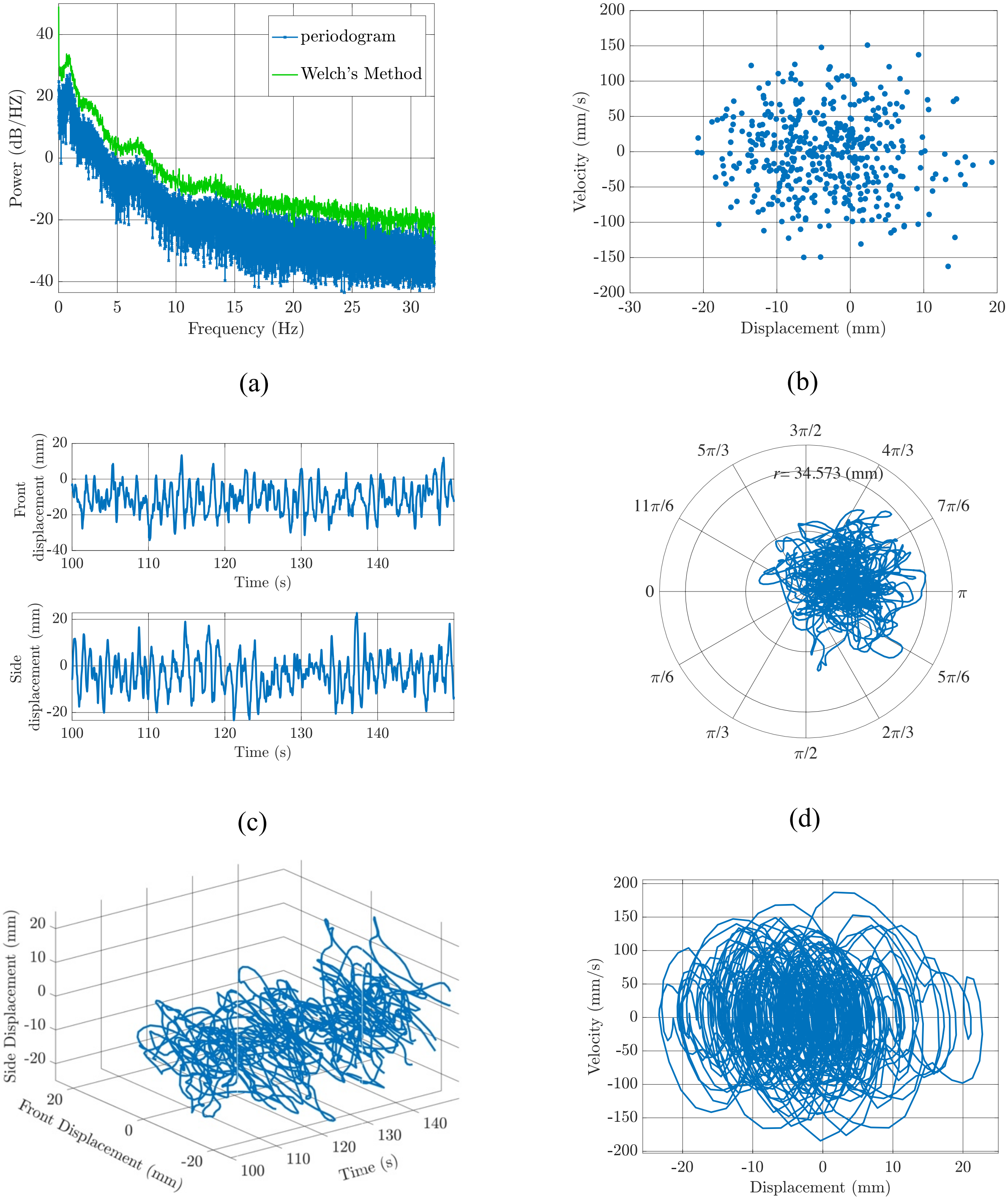

(a) (b)

(c) (d)

(e) (f)

Figure 3-10: (a) PSD; (b) Poincaré map; (c) time series; (d) polar plot; (e) three-dimensional trajectory; (f) displacement-velocity phase portrait (side camera) at $U_i = 3.35$ m/s ($u_i = 3.06$) for $U_o/U_i = 0.20$ and $D_{ch} = 54$ mm (pipe I).

Bifurcation diagrams for rms and mean amplitude versus external flow velocity, U_o (u_o)

In the previous sections, the bifurcation diagrams illustrated rms and mean amplitude versus internal flow velocity, U_i (or u_i). Bifurcation diagrams with external flow velocity U_o on the lower horizontal axis and dimensionless external flow velocity u_o on the upper abscissa are presented next. The lower range of U_o/U_i ratios examined, i.e., 0.015 – 0.06, appeared to fan out from a common line at around $U_o \simeq 0.04$ m/s ($u_o = 0.09$), as illustrated in Figure 3-11(a). On the other hand, for the high range of U_o/U_i ratios (0.20 - 0.80) the curves merged into one at a sufficiently high external flow velocity – refer to Figure 3-11(b). Therefore, the dynamics of the system is independent of the internal flow, or dependent on the external flow only, for the high range of U_o/U_i ratios investigated. This conclusion is in agreement with the one made earlier in section 2.5. A qualitatively similar conclusion was made for the narrow annular gap in Butt et al. [91]. Moreover, the bifurcation diagrams were all combined into one for all U_o/U_i ratios and the reduction in critical flow velocity with increasing U_o/U_i ratios in the form of a bar graph are shown in Figure 3-12(a,b).

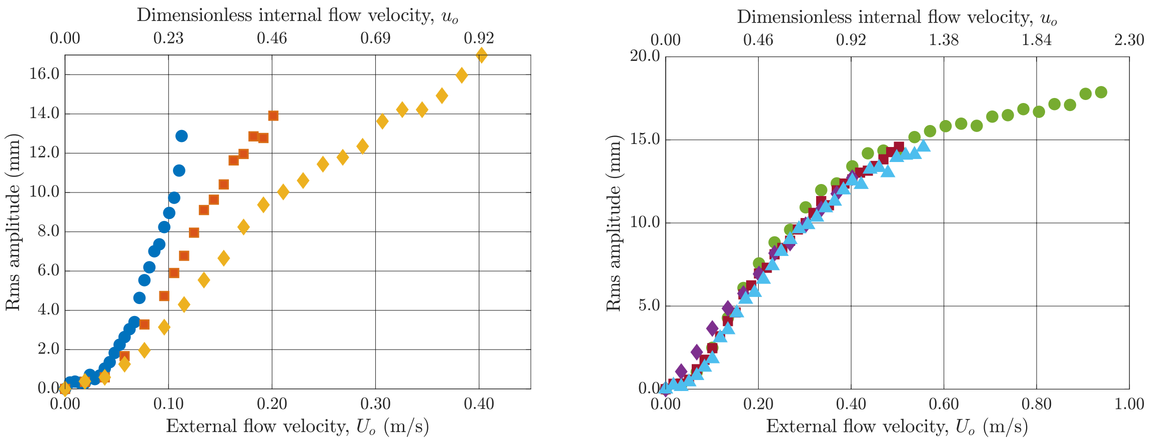

(a) (b)

Figure 3-11: Bifurcation diagrams illustrating rms amplitude of oscillation versus external flow velocity U_o (or dimensionless external flow velocity u_o). (a) $U_o/U_i = 0.015 - 0.06$; (b) $U_o/U_i = 0.20 - 0.80$. Rms amplitude: (●) $U_o/U_i = 0.015$, (■) $U_o/U_i = 0.03$, (◆) $U_o/U_i = 0.06$, (●) $U_o/U_i = 0.20$, (■) $U_o/U_i = 0.40$, (▲) $U_o/U_i = 0.60$, (◆) $U_o/U_i = 0.80$ (Pipe I, $D_{ch} = 54$ mm).

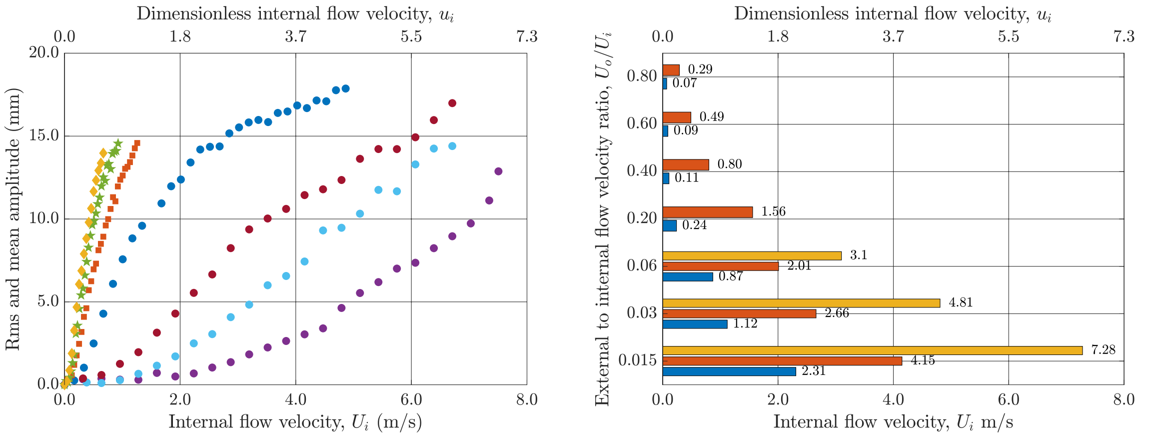

(a) (b)

Figure 3-12: (a) Bifurcation diagrams illustrating rms amplitude of oscillation versus internal flow velocity U_i (or dimensionless internal flow velocity u_i); (b) Bar graph illustrating U_o/U_i versus U_i (or u_i). Rms amplitude: (●) $U_o/U_i = 0.015$, (●) $U_o/U_i = 0.03$, (●) $U_o/U_i = 0.06$, (●) $U_o/U_i = 0.20$, (■) $U_o/U_i = 0.40$, (★) $U_o/U_i = 0.60$, (◆) $U_o/U_i = 0.80$; Bar graph: (🟦) $U_{cr,1}$, (🟧) $U_{cr,2}$, (🟨) $U_{cr,3}$ (Pipe I, $D_{ch} = 54$ mm).

Table 3-1: Summary of results illustrating critical flow velocities (U_i in m/s) for all U_o/U_i ratios investigated for the annular gap size study with pipe I.

	D_{ch} = 54 mm			D_{ch} = 31.5 mm			D_{ch} = 27 mm		
U_o/U_i	$U_{cr,1}$	$U_{cr,2}$	$U_{cr,3}$	$U_{cr,1}$	$U_{cr,2}$	$U_{cr,3}$	$U_{cr,1}$	$U_{cr,2}$	$U_{cr,3}$
0.015	2.31	4.15	7.28	-	-	-	-	-	-
0.03	1.12	2.66	4.81	-	-	-	-	-	-
0.055	-	-	-	1.09	4.11	-	-	-	-
0.06	0.87	2.01	3.10	-	-	-	-	-	-
0.20	0.24	1.56	-	0.41	1.46	-	0.44	1.21	-
0.40	0.11	0.80	-	0.19	0.62	-	0.25	0.60	-
0.60	0.09	0.49	-	-	-	-	-	-	-
0.80	0.07	0.29	-	-	-	-	-	-	-

Discussion of the results related to the effect of annular gap size

The experimental data showed that the first critical flow velocities for the narrower annular gap (D_{ch} = 31.5 mm) are greater than those for the wider annular gap (D_{ch} = 54 mm) for comparable U_o/U_i ratios, i.e., 0.20 and 0.40. On the other hand, the second critical flow velocities were found to decrease as the annular gap size was reduced. The effect of reducing annular gap size on the critical flow velocity was expected to be destabilizing, i.e., lower critical flow velocity, intuitively, as a higher virtual mass or added mass effect would be correlated to a narrower annular gap. In other words, the forces responsible for the instability, namely centrifugal fluid forces which are more substantial for a narrower annular gap are exerted on the pipe. Additionally, the increased inward-directed differential pressure acting on the pipe, leads to a higher pressure requirement for the external flow to pass through the narrower channel. But, as observed in Table 3-1, the effect on stability is the opposite for $U_{cr,1}$.

Experiments were also conducted using a very narrow annular gap of D_{ch} = 27 mm to further investigate the effect of annular gap on $U_{cr,1}$ for U_o/U_i = 0.20 and 0.40. The behaviour for D_{ch} = 27 mm is qualitatively similar to that for D_{ch} = 31.5 mm, in terms of the increasing trends in rms amplitudes, as shown in Figure 3-8(e,f). Furthermore, the effect of reducing the annular gap size on the critical flow velocities remained the same as D_{ch} was reduced to 27 mm, i.e., $U_{cr,1}$ was increased and $U_{cr,2}$ was decreased – refer to Table 3-1.

The stabilizing effect observed with regards to the first critical flow velocities for a narrower annular gap may be due to the existence of prevalent unsteady viscous forces, due to the viscosity-related variations in the unsteady pressure field, in contrast to the weaker inviscid flow effect at low internal flow velocities.

3.2 Experimental results for the Santoprene pipe (pipe II) with a coaxially positioned rigid tube of length L' = 200 mm.

Experiments were also conducted with the wide rigid tube (D_{ch} = 54 mm) for different U_o/U_i ratios using pipe II, which is more slender and has a higher flexural rigidity than pipe I, to see if the behaviour described earlier would persist – refer to Table 2-1 for pipe properties. By continuity, if $Q_a = 0$, then the base case is represented by $U_o/U_i = 0.033$ for pipe II.

The base case will be discussed first and compared to the base case for pipe I, i.e., for U_o/U_i = 0.015. In general, the same behaviour was observed as for pipe I in terms of the increase in rms amplitudes with three different ascending rates – refer to Figure 3-13(a). Moreover, the pipe lost stability by first mode flutter at U_i = 1.70 m/s (u_i = 1.04). Similar to the experiments with pipe I, the first-mode frequency remained dominant with an average value of f_1 = 1.01 Hz as U_i increased. A weak second-mode frequency f_2 = 7.29 Hz appeared in the PSD at U_i = 7.10 m/s (u_i = 4.34) along with the preceding first-mode frequency – refer to Figure 3-14(a). In comparison to U_o/U_i =

0.015, the second-mode frequency materialized at a higher internal flow velocity of U_i = 7.10 m/s (u_i = 4.34) for pipe II as compared to U_i = 3.51 m/s (u_i = 3.21) for pipe I, most likely due to the much greater flexural rigidity of pipe II. Nonetheless, all critical flow velocities were relatively lower for U_o/U_i = 0.033 with pipe II, in contrast to U_o/U_i = 0.015 for pipe I. However, if the critical flow velocities for U_o/U_i = 0.03 are compared, pipe II has relatively higher critical flow velocities as compared to those for pipe I. Furthermore, the behaviour at the maximum attainable flow velocity of U_i = 8.58 m/s (u_i = 5.24) is comparable, in terms of the unsteadiness and intermittent nature of the motions, to that for U_o/U_i = 0.015 for pipe I at the maximum examined flow velocity. However, the magnitude of oscillations was relatively higher, as can be inferred from the greater displacement values illustrated in Figure 3-14(b-d).

For U_o/U_i = 0.06, pipe II demonstrated similar increasing trends in amplitude as those observed with pipe I for the same U_o/U_i ratio – refer to Figure 3-13(b). In the proximity of U_i = 1.48 m/s (u_i = 0.90) and U_i = 2.40 m/s (u_i = 1.47), i.e., for the first two critical flow velocities, the PSDs demonstrated the existence of a first-mode frequency component. As U_i was increased to a value near the third critical flow velocity of U_i = 4.98 m/s (u_i = 3.04), a weak second-mode frequency of f_2 = 7.87 Hz was detected. The third-mode frequency was not noticed for pipe II, although it was present at U_i = 3.83 m/s (u_i = 3.50) for pipe I.

For the higher U_o/U_i ratios of 0.20 and 0.40, the pipe lost stability by first mode flutter at U_i = 0.85 m/s (u_i = 0.52) and U_i = 0.40 m/s (u_i = 0.24), respectively – refer to Figure 3-13(c,d). However, higher vibrational modes, i.e., f_2, f_3, and f_4, were not detected as for similar U_o/U_i ratios for pipe I. The strength of the vibrational modes of the pipe increased with increasing U_i for all experiments conducted with pipe II. The dimensional critical flow velocities, i.e., $U_i = U_{cr}$, for equivalent U_o/U_i

ratios were found to be higher for pipe II in comparison to those for pipe I – refer to Table 3-2.

Dimensionless critical flow velocities based on equation (2.1) are summarized in Table A-2.

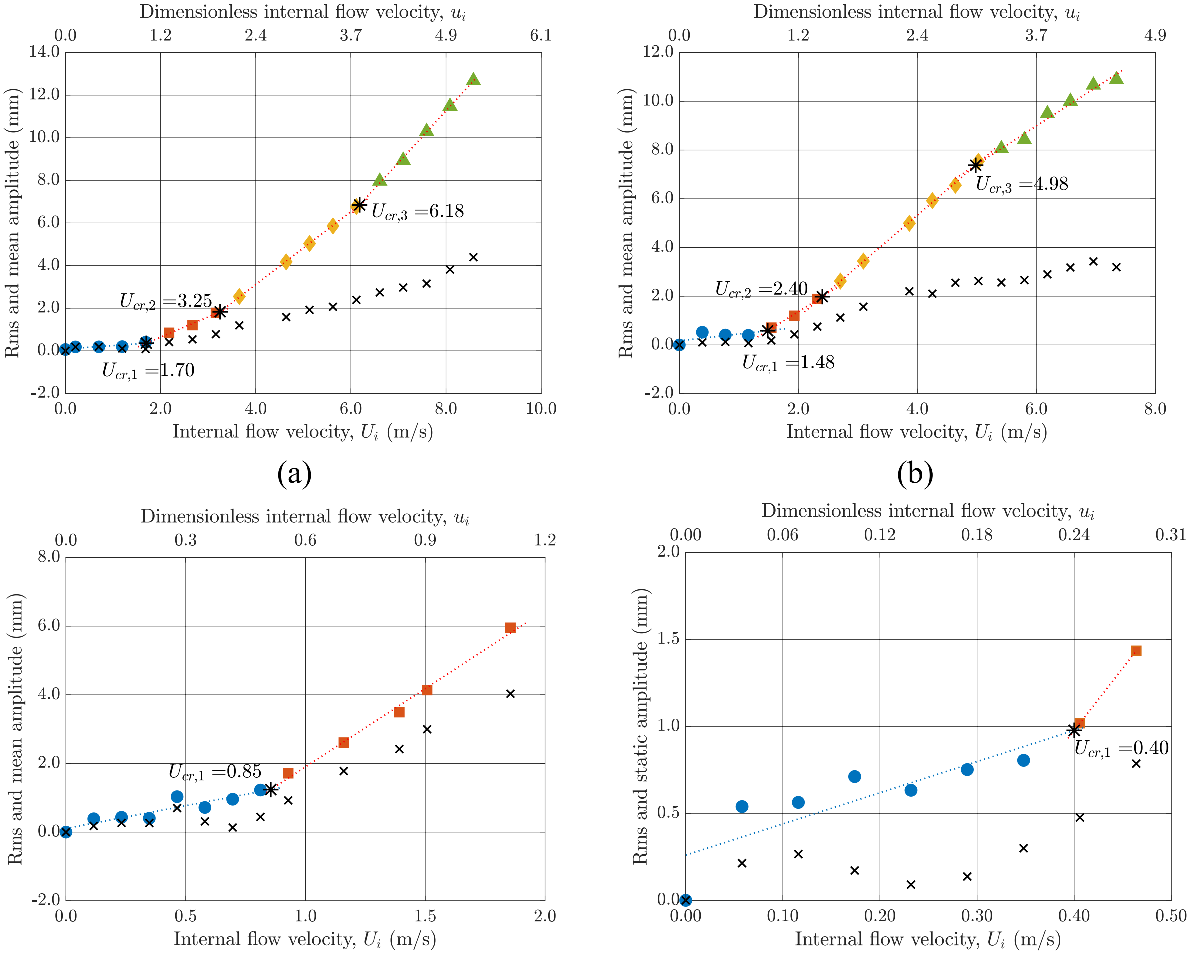

(a)

(b)

(c)

(d)

Figure 3-13: Bifurcation diagrams illustrating rms and mean amplitudes of oscillation versus internal flow velocity U_i (or dimensionless internal flow velocity u_i). (a) $U_o/U_i = 0.015$; (b) $U_o/U_i = 0.06$; (c)$U_o/U_i = 0.20$; (d) $U_o/U_i = 0.40$. Rms amplitude: (●) Pre-instability, (■) Post-instability 1, (◆) Post-instability 2, (▲) Post-instability 3; (∗) Critical flow velocity; (×) Mean deformation (pipe II, D_{ch} = 54 mm).

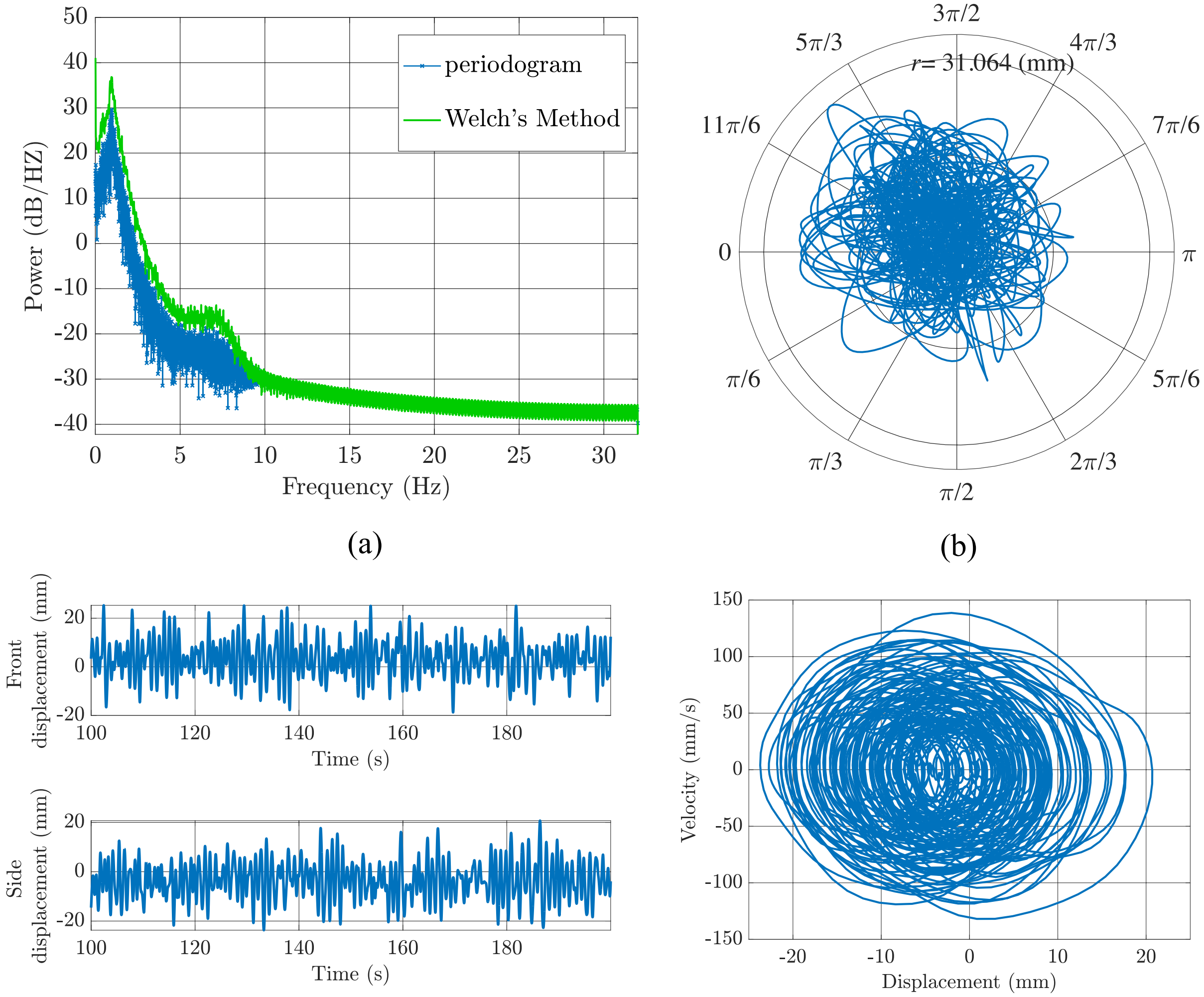

(a) (b)

(c) (d)

Figure 3-14: (a) PSD; (b) polar plot; (c) time series; (d) displacement-velocity phase portrait (side camera) at $U_i = 8.58$ m/s ($u_i = 5.24$) for $U_o/U_i = 0.033$ and $D_{ch} = 54$ mm (pipe II).

Table 3-2: Comparison of the critical flow velocities (U_i in m/s) for all U_o/U_i ratios investigated with pipes I and II.

	$D_{ch} = 54$ mm Pipe I			$D_{ch} = 54$ mm Pipe II		
U_o/U_i	$U_{cr,1}$	$U_{cr,2}$	$U_{cr,3}$	$U_{cr,1}$	$U_{cr,2}$	$U_{cr,3}$
0.033	-	-	-	1.70	3.25	6.18
0.06	0.87	2.01	3.10	1.48	2.40	4.98
0.20	0.24	1.56	-	0.85	-	-
0.40	0.11	0.80	-	0.40	-	-

3.3 Experimental results for an eccentrically positioned rigid tube of length L' = 200 mm with regards to flexible pipe I.

A set of experiments was conducted to examine the effect of eccentrically positioning the 200 mm long plexiglas tube with respect to pipe I on the dynamics. The displacement between the centerline of the pipe and that of the rigid tube is denoted by t_{gap} – refer to section 2.3.1 for the experimental setup. Two displacements or eccentricities were investigated, namely t_{gap1} = 10 mm and t_{gap2} = 14 mm. In this section, the results of the two eccentric cases will be compared to those of the concentric case discussed in the preceding subsections.

The behaviour of the aspirating pipe for the eccentric pipe experiments, for both t_{gap1} = 10 mm and t_{gap2} = 14 mm, was found to be qualitatively comparable to the concentric case for all U_o/U_i ratios examined. The bifurcation diagrams illustrate similar amplitude trends for all U_o/U_i ratios as those for the concentric case – refer to Figure 3-15 (a-d). Once more the pipe lost stability via first-mode flutter and the first-mode frequency remained dominant as U_i was increased for all U_o/U_i ratios. The value of the first-mode frequency component was found to increase with U_i only for high U_o/U_i ratios as was observed in the concentric case. The higher vibrational modes, i.e., f_2 for $U_o/U_i = 0.015$ and f_2 - f_4 for $U_o/U_i = 0.20 – 0.40$, appeared in the PSDs and became meaningful at nearly equivalent internal flow velocities to those observed for the concentric cases. The only exception is the experiment with an eccentricity of t_{gap1} = 10 mm for $U_o/U_i = 0.80$, in which the fourth-mode frequency was not observed; perhaps the flow velocity needed to excite it was not attained.

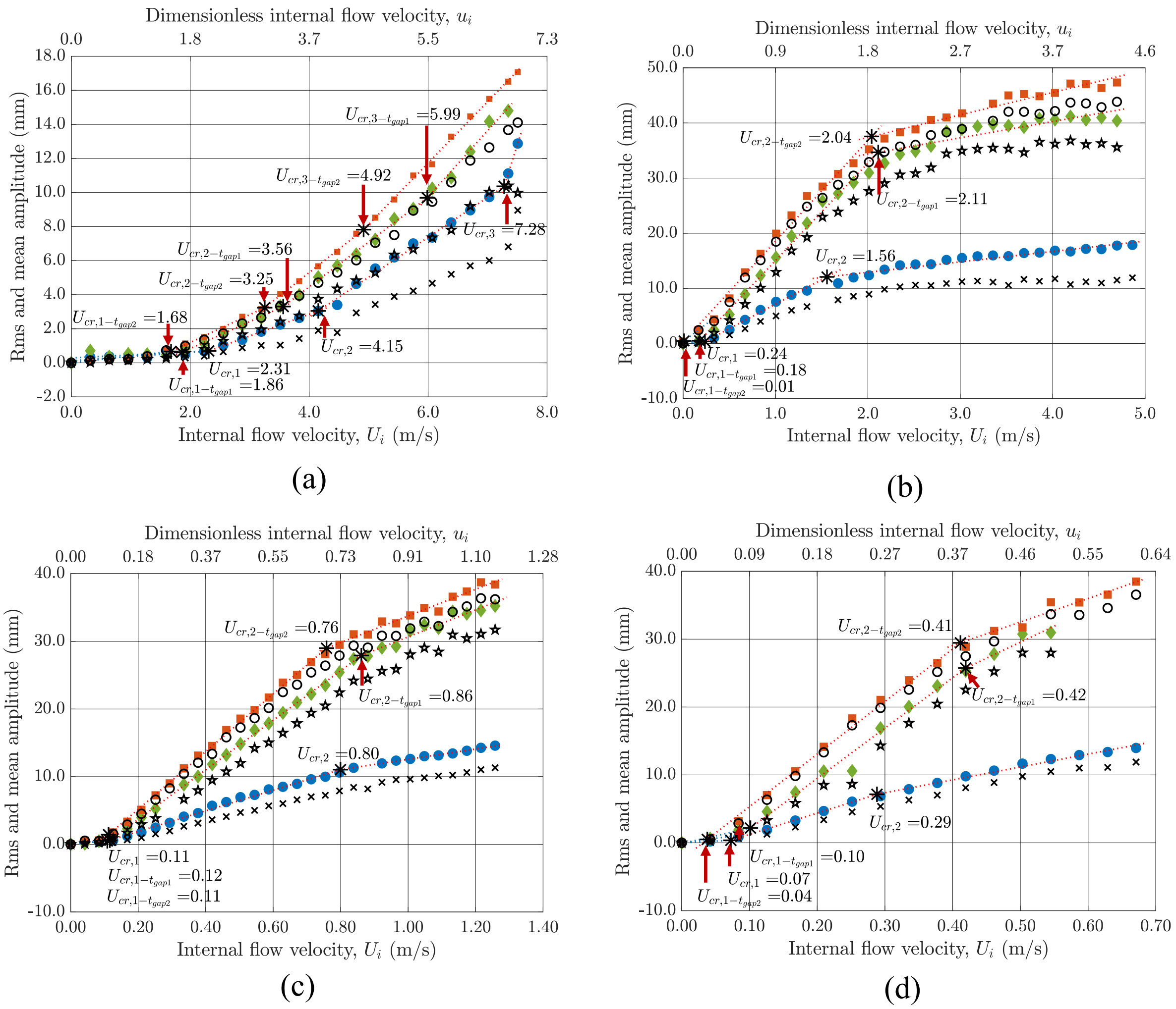

Figure 3-15: Bifurcation diagrams illustrating rms and mean amplitudes of oscillation versus internal flow velocity U_i (or dimensionless internal flow velocity u_i). (a) $U_o/U_i = 0.015$; (b) $U_o/U_i = 0.20$; (c)$U_o/U_i = 0.40$; (d) $U_o/U_i = 0.80$. Rms amplitude: (●) concentric outer tube; (◆) eccentric outer tube with t_{gap1} = 10 mm; (■) eccentric outer tube with t_{gap2} = 14 mm. (∗) Critical flow velocity; (×) mean deformation for concentric outer tube; (☆) mean deformation for eccentric outer tube with t_{gap1} = 10 mm; (○) mean deformation for eccentric case with t_{gap2} = 14 mm (pipe I, D_{ch} = 54 mm).

A noticeable destabilizing effect, in terms of an increase in amplitude of oscillations, was observed with increasing eccentricity for all regions, except for the region with turbulence induced motions, as shown in Figure 3-15 (a-d). The increase in amplitude of oscillations is mainly due to the increase in mean deformation rather than in the oscillatory component, which remained almost constant with increasing eccentricity. This was verified by visual observations, as the pipe demonstrated large static deformation towards the centerline of the rigid tube, which increased in magnitude with increasing internal flow velocity, with a relatively weaker superimposed oscillatory component.

Figure 3-16 illustrates the change or increase in mean deformation for both t_{gap1} = 10 mm and t_{gap2} = 14 mm eccentricity experiments with respect to the concentric case for all U_o/U_i ratios. Two observations can be made based on Figures 3-15 and 3-16: variations in mean deformation (i) are greater in magnitude for higher U_o/U_i ratios, regardless of the eccentricity degree, (ii) are higher for a greater offset or eccentricity degree for each one of the U_o/U_i ratios examined.

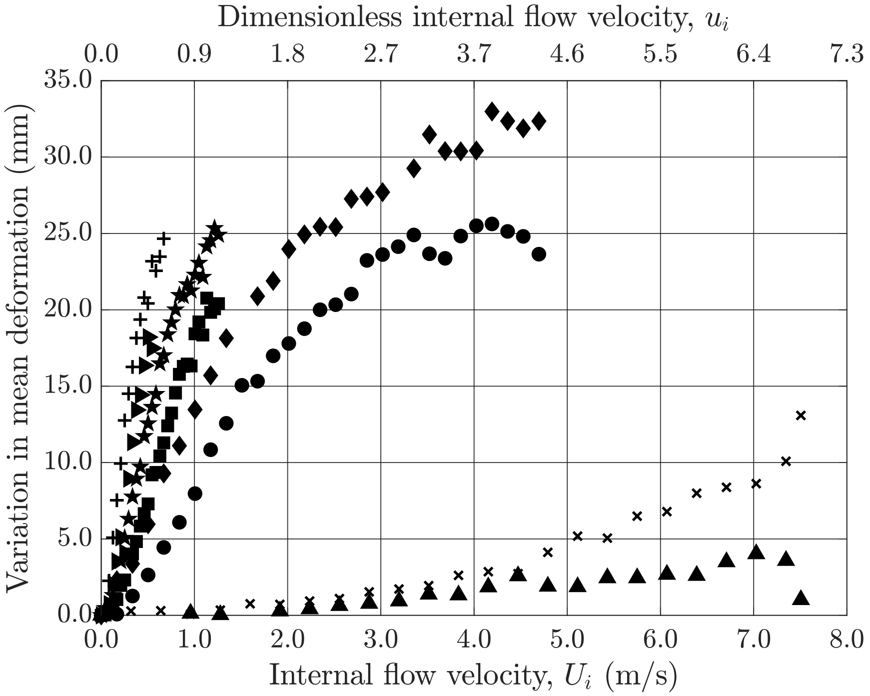

Figure 3-16: Bifurcation diagrams illustrating variation in mean deformation of oscillation versus internal flow velocity U_i (or dimensionless internal flow velocity u_i). Variation in mean deformation for t_{gap1} = 10 mm with respect to the concentric case: (▲) U_o/U_i = 0.015, (●) U_o/U_i = 0.20, (■) U_o/U_i = 0.40, (▶) U_o/U_i = 0.80. Variation in mean deformation for t_{gap2} = 14 mm with respect to the concentric case: (x) U_o/U_i = 0.015, (◆) U_o/U_i = 0.20, (★) U_o/U_i = 0.40, (+) U_o/U_i = 0.80 (pipe I, D_{ch} = 54 mm).

Beyond the pre-instability region, the change in mean deformation illustrated increasing trends with increasing internal flow velocity for all U_o/U_i. The increase was found to be more significant for higher U_o/U_i ratios.

Overall, the phase portraits and time traces demonstrate the unsteady and chaotic nature of oscillation – refer to Figures 3-17(a-d) and 3-18 (a-d). The time traces and phase portraits are more or less similar to those observed for the concentric case at equivalent U_i values – refer to the data of the concentric experiments in Figure 3-3(c,d) for $U_o/U_i = 0.015$ and Figure 3-10(c,f) for $U_o/U_i = 0.20$. The eccentric position of the pipe with respect to the rigid tube was reflected in the phase portraits by the fact that the curves, representing the trajectories of the system, are not centered about the zero-displacement mark as in the concentric case.

Critical flow velocities

For $U_o/U_i = 0.015$, the critical flow velocities were found to decrease with increasing eccentricity.

For $U_o/U_i = 0.20$, the first critical flow velocity showed a decreasing trend with increasing eccentricity. However, for $U_o/U_i > 0.20$, i.e., for 0.40 and 0.80, there was no trend with regard to $U_{cr,1}$. On the other hand, the second critical flow velocity was delayed when the degree of eccentricity was increased from $t_{gap} = 0$ to $t_{gap1} = 10$ mm; however, increasing eccentricity to 14 mm led to a very minor reduction in the second critical flow velocity for $U_o/U_i = 0.20 – 0.80$.

The decreasing trend in critical flow velocities with increasing U_o/U_i ratios was preserved for $t_{gap1} = 10$ mm and $t_{gap2} = 14$ mm, with the exception of $U_o/U_i = 0.20$ for $t_{gap2} = 14$ mm where a very low first critical flow velocity was detected. The dimensional critical flow velocities are summarized in Table 3-3 and the dimensionless critical flow velocities are presented in Table A-3.

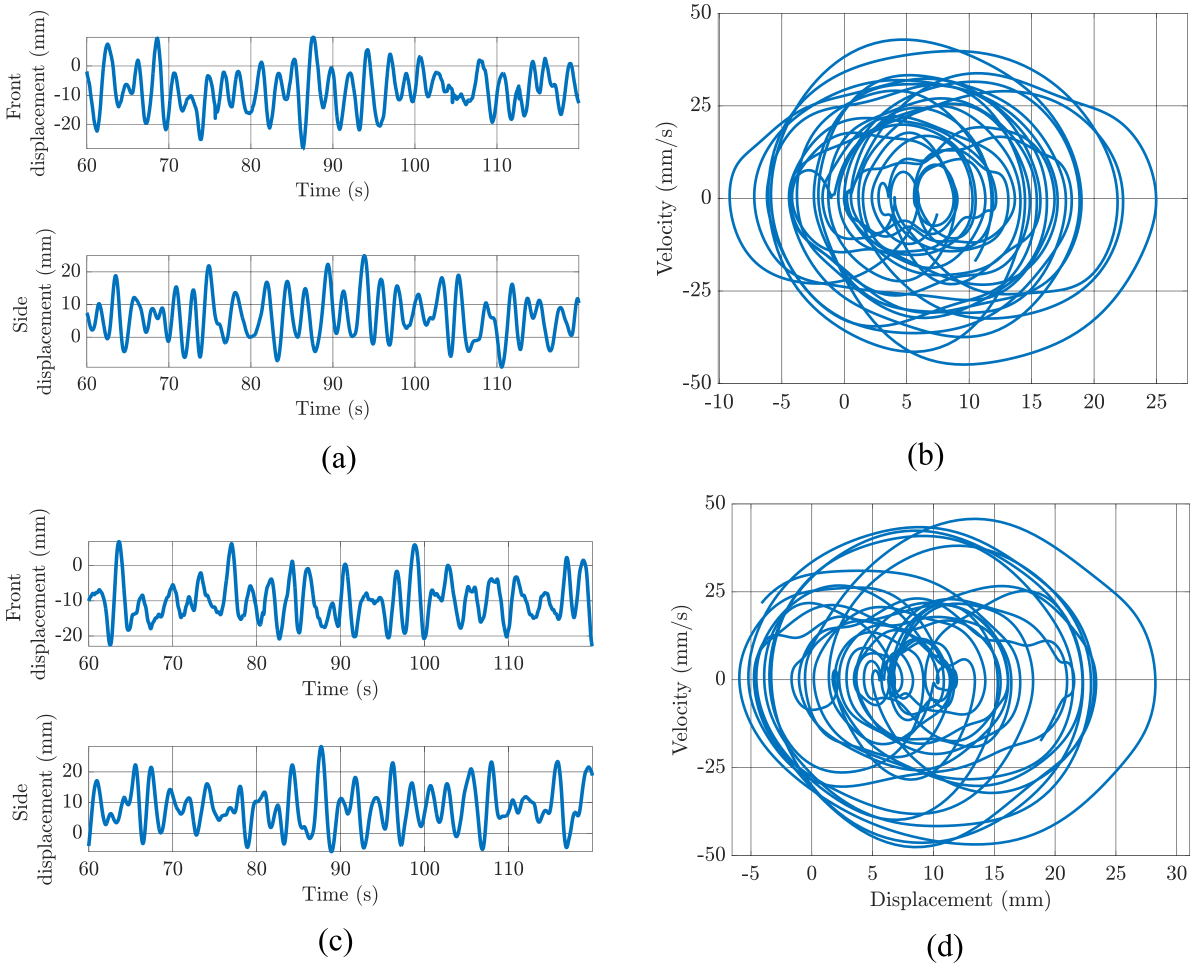

Figure 3-17: (a) Time series for t_{gap1} = 10 mm; (b) phase portrait (side camera) for t_{gap1} = 10 mm; (c) time series for t_{gap2} = 14 mm; (d) phase portrait (side camera) for t_{gap2} = 14 mm at U_i = 7.03 m/s (u_i = 6.43) for U_o/U_i = 0.015 (pipe I, D_{ch} = 54 mm).

Table 3-3: Comparison of the critical flow velocities (U_i in m/s) for all U_o/U_i ratios investigated with pipe I for various eccentricities.

	Concentric $t_{gap,1} = 0$ mm			Eccentric $t_{gap,1} = 10$ mm			Eccentric $t_{gap,1} = 14$ mm		
U_o/U_i	$U_{cr,1}$	$U_{cr,2}$	$U_{cr,3}$	$U_{cr,1}$	$U_{cr,2}$	$U_{cr,3}$	$U_{cr,1}$	$U_{cr,2}$	$U_{cr,3}$
0.015	2.31	4.15	7.28	1.86	3.56	5.99	1.68	3.25	4.92
0.20	0.24	1.56	-	0.18	2.11	-	0.01	2.04	-
0.40	0.11	0.80	-	0.12	0.86	-	0.11	0.76	-
0.80	0.07	0.29	-	0.10	0.42	-	0.04	0.41	-

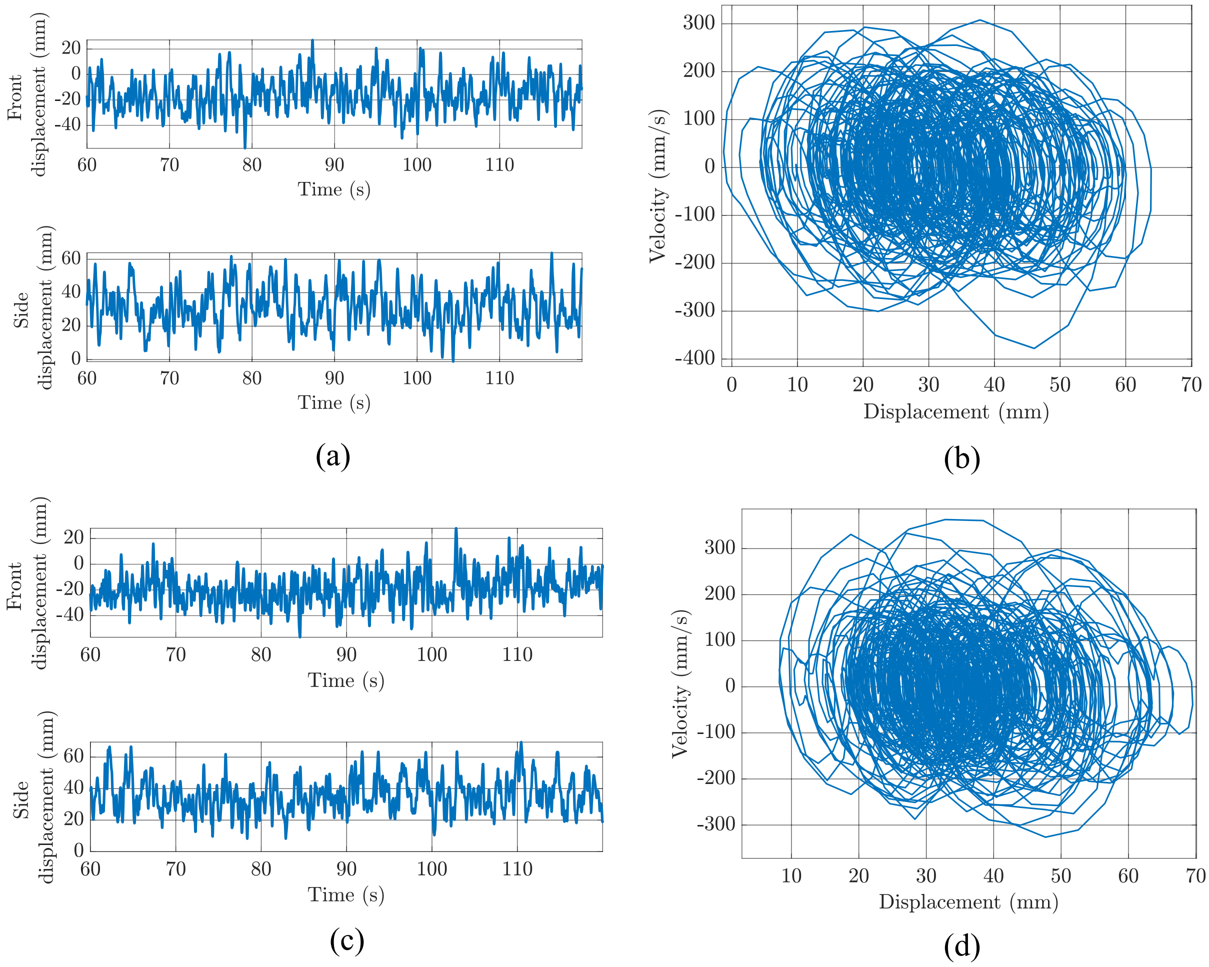

Figure 3-18: (a) Time series for $t_{gap1} = 10$ mm; (b) phase portrait (side camera) for $t_{gap1} = 10$ mm; (c) time series for $t_{gap2} = 14$ mm; (d) phase portrait (side camera) for $t_{gap2} = 14$ mm at $U_i = 3.35$ m/s ($u_i = 3.06$) for $U_o/U_i = 0.20$ (pipe I, $D_{ch} = 54$ mm).

Discussion of the results related to the effect of eccentricity

The experimental results for the effect of eccentricity demonstrated a destabilizing effect in terms of magnitude of oscillations. The increase in amplitude of oscillations is mainly due to an increase in mean deformation in contrast to the oscillatory component which remained almost constant. This may be attributed to the unbalanced external pressure forces since eccentricity alters the distribution of the external flow surrounding the central flexible pipe. In the current investigation the eccentricity was applied in the direction of the front window and camera. In other words, the outer rigid tube is closer to the front window and further away from the rear window. The smaller flow area at the back causes an increase in external pressure forces on that side of the pipe in comparison to the relatively weaker pressure forces on the other side. Therefore, a net force towards the centerline of the rigid tube or the front window would be generated, as was observed in the recent experimental examination. The unbalanced pressure force effect grows in magnitude with increasing eccentricity as shown by the more pronounced mean deformation amplitude for a greater eccentricity.

Frequency of the pipe at the tip versus near the outlet (or free end) of the plexiglas tube

It was visually observed that the magnitude or vibrational modes within the rigid tube, in particular right before the outlet (free end) of the plexiglas tube and at the tip of the pipe are different. The validity of this observation was tested through an experiment for an eccentricity degree of t_{gap1} = 10 mm and U_o/U_i = 0.40 in which this observation was more pronounced in comparison to prior experiments. The front camera utilized in prior experiments was used in addition to another camera at a higher level focused on a red marked region just before the outlet of the rigid tube (inside the tube). The oscillations were recorded at various internal flow velocities ranging from 0.67 m/s (u_i=0.61) to 1.03 m/s (u_i= 1.03).

The data collected from the camera focused on the tip of the pipe showed at most a relatively weak first-mode frequency at U_i = 0.67 m/s (u_i = 0.61) and 1.01 m/s (u_i = 0.92) – refer to Figure 3-19(a,e). On the other hand, the results from the camera focused on the region inside the rigid tube, right before its free end, illustrated a more visible first-mode frequency as well as higher vibrational modes of very low power, i.e., f_2 and f_3, which were not previously detected at the tip of the pipe for all U_i values examined – refer to Figure 3-19(a-j). Moreover, the magnitude of the first-mode component was more pronounced within the rigid tube in comparison to the tip of the pipe.

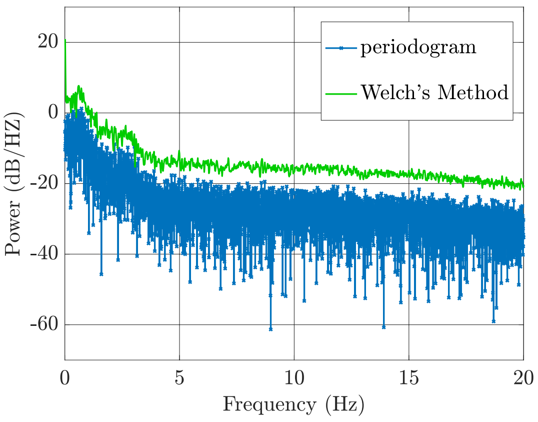
periodogram
Welch's Method
Power (dB/HZ)
20
0
-20
-40
-60
0
5
10
15
20
Frequency (Hz)

(a)

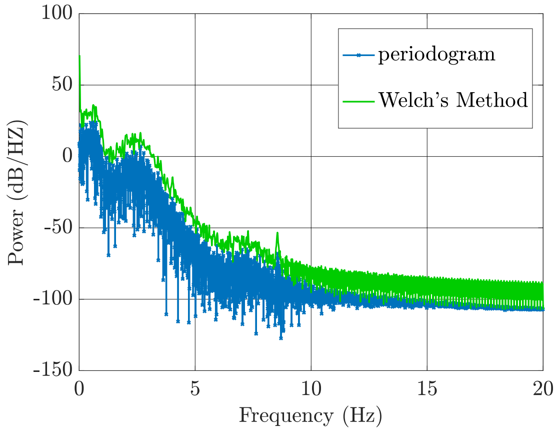
periodogram
Welch's Method
Power (dB/HZ)
100
50
0
-50
-100
-150
0
5
10
15
20
Frequency (Hz)

(b)

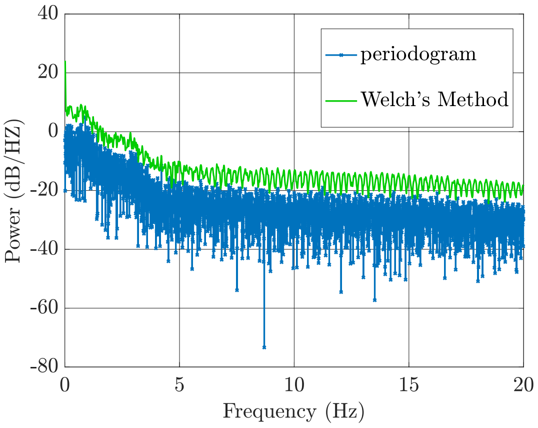
periodogram
Welch's Method
Power (dB/HZ)
40
20
0
-20
-40
-60
-80
0
5
10
15
20
Frequency (Hz)

(c)

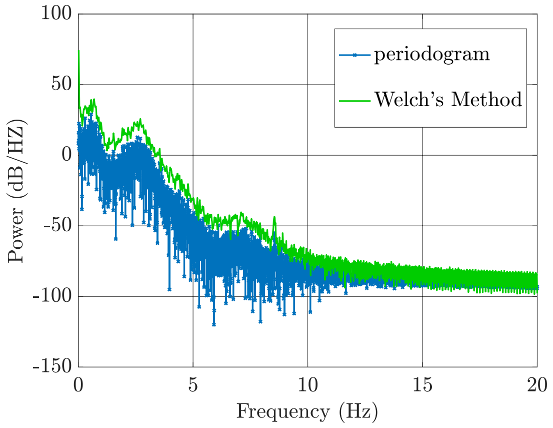
periodogram
Welch's Method
Power (dB/HZ)
100
50
0
-50
-100
-150
0
5
10
15
20
Frequency (Hz)

(d)

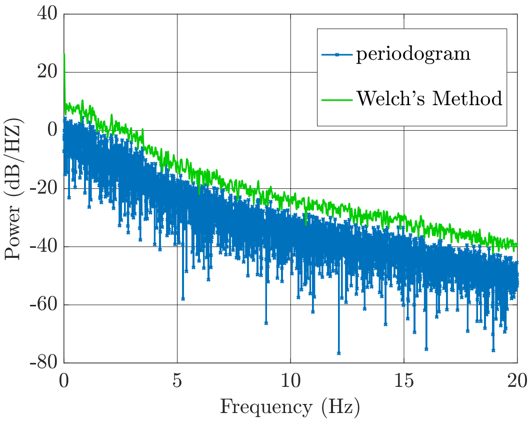
periodogram
Welch's Method
Power (dB/HZ)
40
20
0
-20
-40
-60
-80
0
5
10
15
20
Frequency (Hz)

(e)

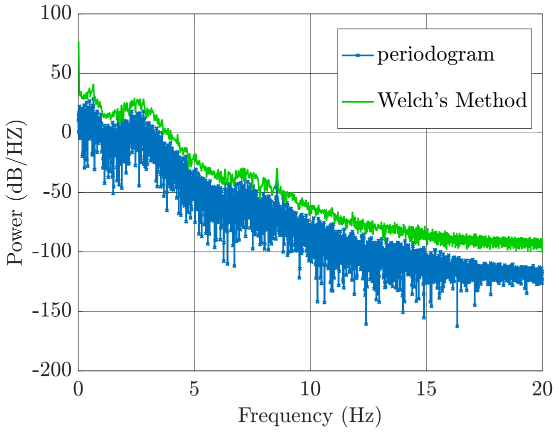
periodogram
Welch's Method
Power (dB/HZ)
100
50
0
-50
-100
-150
-200
0
5
10
15
20
Frequency (Hz)

(f)

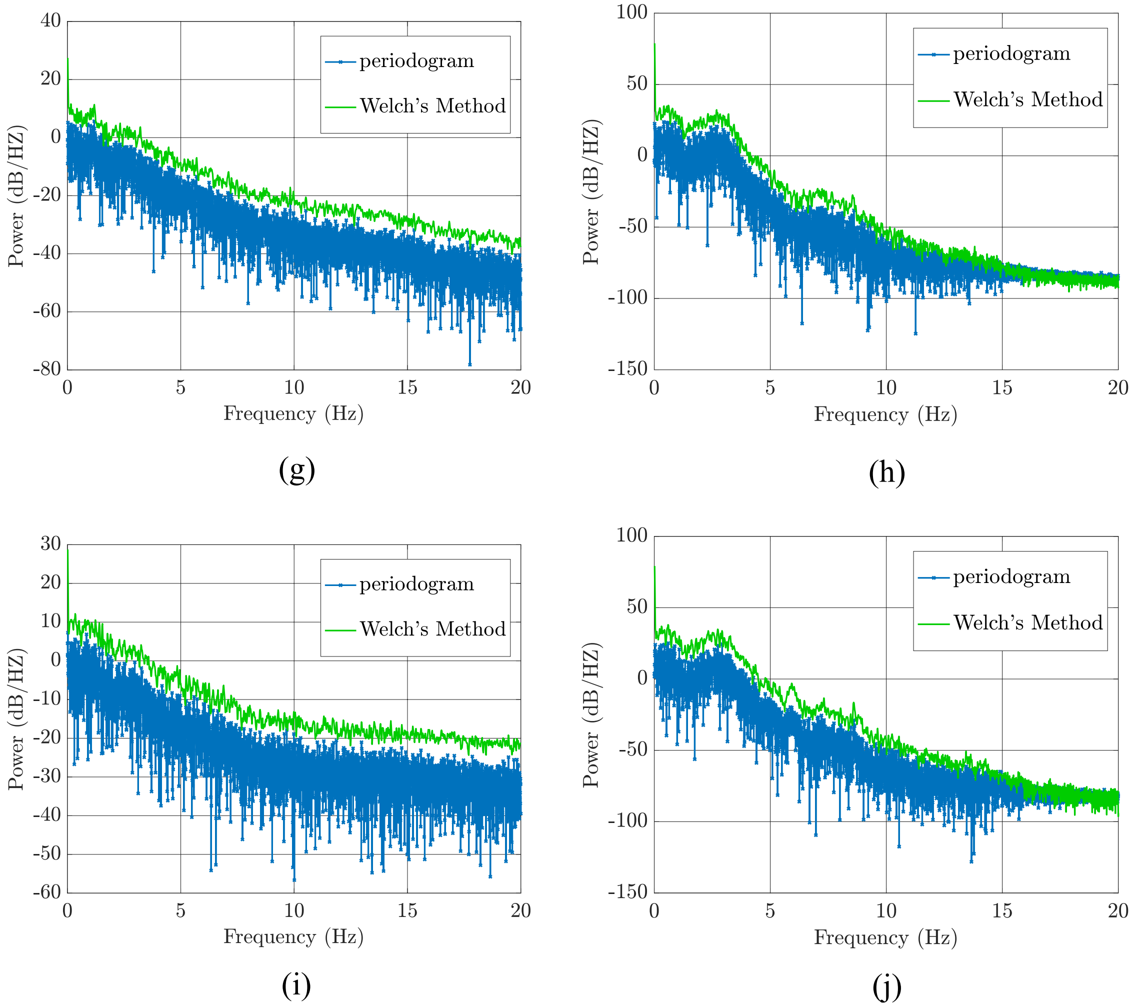

(g) (h)

(i) (j)

Figure 3-19: PSDs at $U_i = 0.67$ m/s ($u_i = 0.61$) (a) bottom camera, (b) top camera; $U_i = 0.80$ m/s ($u_i = 0.73$) (c) bottom camera, (d) top camera; $U_i = 0.92$ m/s ($u_i = 0.84$) (e) bottom camera, (f) top camera; $U_i = 1.01$ m/s ($u_i = 0.92$) (g) bottom camera, (h) top camera; $U_i = 1.13$ m/s ($u_i = 1.03$) (i) bottom camera, (j) top camera for $U_o/U_i = 0.40$ (pipe I, $D_{ch} = 54$ mm, $t_{gap1} = 10$ mm).

3.4 Experimental results for the shorter silicone-rubber pipe (pipe III) with a coaxially positioned rigid tube of length $L' = 100$ mm.

Experiments were conducted with a shorter pipe (pipe III) of the same material as the longer silicone-rubber pipe (pipe I) to study the effect of pipe length on the onset of instability and post-instability dynamical behaviour. The experiments with pipe III utilized a plexiglas tube of length $L' = 100$ mm such that the ratio of the rigid tube length to that of the pipe remains constant, i.e.,

$r_{ann} = \frac{L'}{L} \simeq$ ½, to facilitate comparison with the experiments conducted using pipe I and rigid tube of $L' = 200$ mm.

The behaviour of the short silastic pipe is comparable to that of the longer version in terms of trends in rms amplitudes for all U_o/U_i ratios – refer to Figure 3-20(a-d). The rms amplitude of the shorter pipe was found to be similar to that for the longer pipe at identical dimensionless internal flow velocity values, i.e., u_i, and for equivalent U_o/U_i ratios. In other words, the magnitude of oscillations was found to be nearly equivalent for the shorter pipe at $U_i = x$ and for the longer pipe at $U_i = 2x$ for all U_o/U_i ratios tested. However, the critical flow velocities were not doubled in dimensional form (U_{cr}) or halved in dimensionless form (u_{cr}) as the pipe length was halved – refer to Table 3-4 (dimensional) and Table A-5 (dimensionless) for the critical flow velocity ratios. A side-by-side summary of the critical flow velocities for pipes I and III can be found in Table 3-5 (dimensional) and Table A-6 (dimensionless). The critical flow velocities and pipe length are believed to be related in a complex manner. Furthermore, the current results demonstrated a change at an average rate around 1.52 for U_{cr} and 0.78 for u_{cr} – refer to Tables 3-4 and A-5.

The decreasing pattern in critical flow velocities with increasing U_o/U_i ratio was preserved for the shorter pipe. Moreover, the critical flow velocities for the shorter pipe were delayed (higher) in contrast to those for the longer pipe. There was also a delay in the appearance of the higher vibrational frequency components in comparison to pipe I.

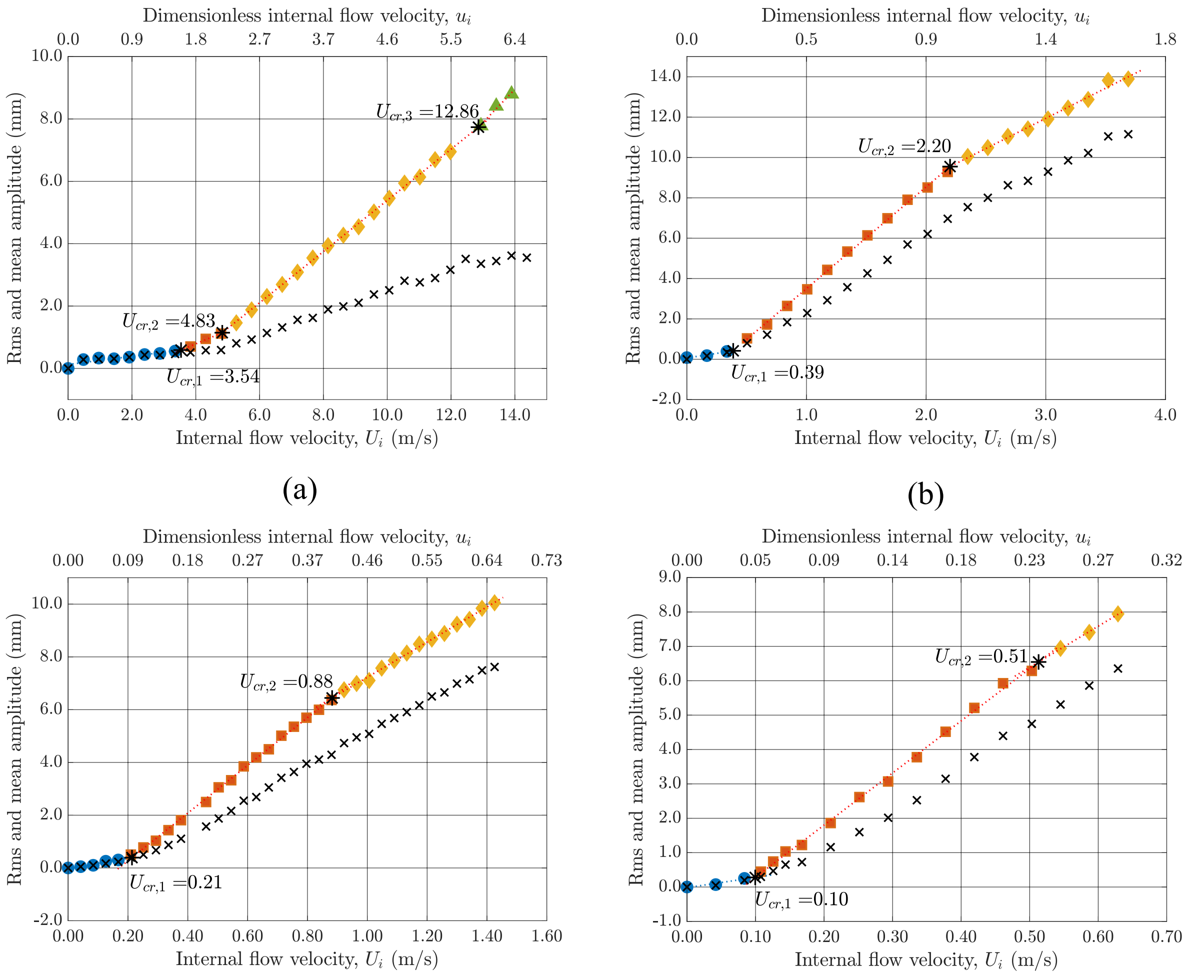

(a)

(b)

(c)

(d)

Figure 3-20: Bifurcation diagrams illustrating rms and mean amplitudes of oscillation versus internal flow velocity U_i (or dimensionless internal flow velocity u_i). (a) $U_o/U_i = 0.015$; (b) $U_o/U_i = 0.20$; (c) $U_o/U_i = 0.40$; (d) $U_o/U_i = 0.80$. Rms amplitude: (●) Pre-instability, (■) Post-instability 1, (◆) Post-instability 2; (✱) Critical flow velocity; (✕) Mean deformation (pipe III, D_{ch} = 54 mm, L' = 100 mm).

Table 3-4: Summary of the critical flow velocity (U_i in m/s) ratios of pipe III to pipe I for all U_o/U_i ratios investigated.

U_o/U_i	$\frac{U_{cr,1}\text{ (pipe III)}}{U_{cr,1}\text{ (pipe I)}}$	$\frac{U_{cr,2}\text{ (pipe III)}}{U_{cr,2}\text{ (pipe I)}}$	$\frac{U_{cr,3}\text{ (pipe III)}}{U_{cr,3}\text{ (pipe I)}}$
0.015	1.53	1.16	1.77
0.20	1.62	1.41	-
0.40	1.91	1.10	-
0.80	1.43	1.76	-

Table 3-5: Comparison of the critical flow velocities (U_i in m/s) for all U_o/U_i ratios investigated with pipes I and III of different length and constant $r_{ann} \simeq ½$.

	Plexiglas tube (L' = 200 mm) Pipe I (L = 441 mm)			Plexiglas tube (L' = 100 mm) Pipe III (L = 221 mm)		
U_o/U_i	$U_{cr,1}$	$U_{cr,2}$	$U_{cr,3}$	$U_{cr,1}$	$U_{cr,2}$	$U_{cr,3}$
0.015	2.31	4.15	7.28	3.54	4.83	12.86
0.20	0.24	1.56	-	0.39	2.20	-
0.40	0.11	0.80	-	0.21	0.88	-
0.80	0.07	0.29	-	0.10	0.51	-

The base case, i.e., $U_o/U_i = 0.015$, lost stability via first-mode flutter at $U_i = 3.54$ m/s ($u_i = 1.62$) and the first-mode frequency around $f_1 \simeq 1.53$ Hz remained dominant as U_i was increased. At U_i = 4.83 m/s ($u_i = 2.21$), a steeper increase in rms amplitude was observed, and this flow velocity is denoted by $U_{cr,2}$; refer to Figure 3-20(a). Near the end of post-instability 2, a weak second-mode frequency component around $f_2 \simeq 9.62$ Hz was detected in the proximity of U_i = 11.50 m/s (u_i = 5.27) but never materialized as U_i was increased. At U_i = 12.98 m/s ($u_i = 5.95$), which is referred to as the third critical velocity, i.e., $U_{cr,3}$, the steepest increase in rms amplitude began, as depicted in Figure 3-20(a). The pipe vibrational modes have been detected and materialized at relatively higher internal flow velocities as opposed to the case with the longer pipe.

For $U_o/U_i = 0.20$, the pipe became unstable by first-mode flutter at $U_i = 0.39$ m/s ($u_i = 0.18$) and the first-mode frequency continued to be dominant with increasing U_i. Mixed-mode oscillations, composed of first and weaker second-mode frequencies, were observed at $U_i = 2.20$ m/s ($u_i = 1.01$). The PSD illustrating the mixed-mode oscillations at $U_i = 3.35$ m/s ($u_i = 1.53$) is shown in Figure 3-21(c). Furthermore, a very weak third-mode frequency around $f_3 \simeq 25.73$ Hz was detected near the end of post-instability 2. In comparison to the experiment with the longer pipe, the weak fourth-mode frequency was not detected and the preceding vibrational modes, i.e.,

f_2 and f_3, were detected and found to materialize at comparably higher internal flow velocities in contrast with the experiments conducted with pipe I. The time traces and phase portrait, similar to the experiment with pipe I, demonstrated the chaotic and unsteady nature of the motions – refer to Figure 3-21(a,b). However, the oscillations seem to be centered about the -10 mm displacement mark rather than the origin like in the case of the longer pipe. The unsymmetric curves in the phase portrait were also noticed for the other U_o/U_i ratios and it was found to be less severe for the case of $U_o/U_i = 0.015$.

The observations for flow velocity ratios of $U_o/U_i = 0.40$ and $U_o/U_i = 0.80$ are comparable to those for $U_o/U_i = 0.20$ with regards to loss of stability by first-mode flutter, mixed-mode flutter, i.e., involving f_1 and f_2, at a higher U_i, and no sign of a fourth-mode vibrational component. A weak third-mode frequency near the maximum attainable flow velocity was observed for $U_o/U_i = 0.40$; however, it was not detected for $U_o/U_i = 0.80$. The higher vibrational modes likely require a higher internal flow velocity to be excited in the case of a short pipe. In other words, the higher vibrational modes would be expected to appear at similar dimensionless internal flow velocities for pipe I and III.

The dominant first-mode frequency was found to increase in value as U_i increased for the high U_o/U_i ratios and it remained nearly constant around $f_1 \simeq 1.53$ Hz for $U_o/U_i = 0.015$ – refer to Figure 3-21(d). This pattern is similar to that observed for the longer pipe.

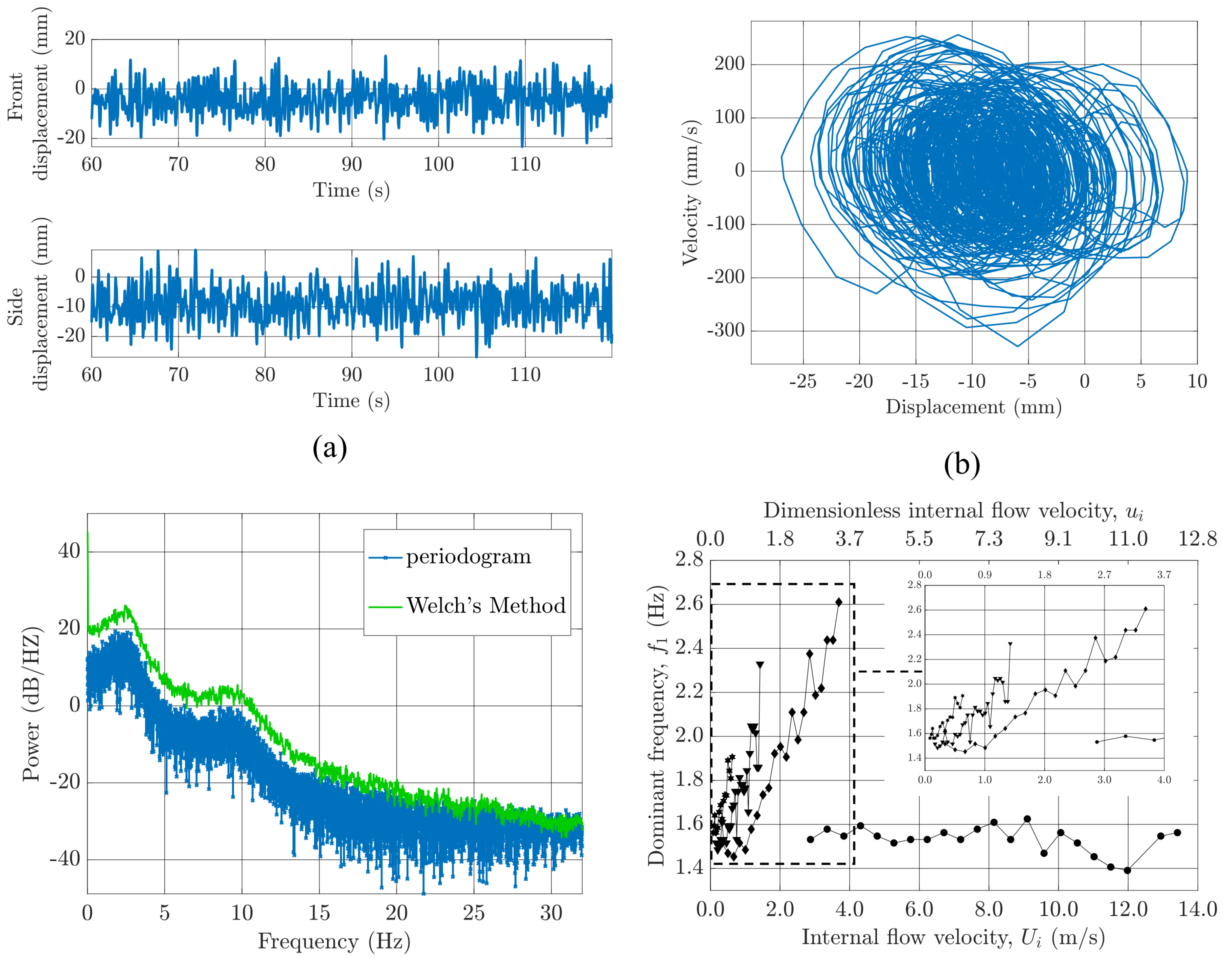

(a) (b)

(c) (d)

Figure 3-21: (a) time traces, (b) phase portrait (side camera), (c) PSD at $U_i = 3.35$ ($u_i = 1.53$) for $U_o/U_i = 0.20$; (d) f_1 versus internal flow velocity, U_i (or dimensionless internal flow velocity u_i). (●) $U_o/U_i = 0.015$, (◆) $U_o/U_i = 0.20$; (▼) $U_o/U_i = 0.40$, (✶) $U_o/U_i = 0.80$ (pipe III, $D_{ch} = 54$ mm, $L' = 100$ mm).

Discussion of the results pertaining to the effect of pipe length

The results presented for the effect of pipe length on the critical flow velocities, showed a reducing trend in dimensional critical flow velocity with increasing pipe length for a partially confined pipe. The results were also presented in terms of dimensionless terms, i.e., u_{cr}, which were computed considering the length L of the flexible pipe in the formulation given in equation

(2.1). Therefore, this formulation is not applicable for the examination of the effect of pipe length on the dynamics of the system considered. A more suitable non-dimensional formulation has been suggested by de Langre et al. [75] for cylinders subjected to axial flow as well as in Doaré and de Langre [76] for sufficiently long hanging pipes conveying fluid. The formulation in [76] accounts for the ratio between flexural rigidity and the gravitational force per unit length instead of the actual length of the pipe by defining a new parameter η, which is defined as:

$$\eta = \left(\frac{EI}{(\rho A_i+m)g}\right)^{\frac{1}{3}} \tag{3.1}$$

The dimensionless flow velocity is then defined in terms of η as:

$$v = \left(\frac{\rho A_i}{EI}\right)^{\frac{1}{2}} \eta\, U \tag{3.2}$$

Moditis et al. [12] investigated theoretically the effect of the length on a pipe subject to counter-current internal and external flows similar to the system under consideration in this study; however, the flow directions were reversed, i.e., discharging pipe and aspirating annulus.

The current experimental results demonstrate a “stabilizing” effect (i.e., abated diminution), as the pipe length was increased, in terms of dimensional and dimensionless critical flow velocities, computed using the de Langre formulation in (3.2) – refer to Tables 3-5 and A-4, respectively. Even though the de Langre formulation is significant for relatively long pipes, it reflects the stabilizing effect expected for the critical flow velocities. This behaviour is likely associated with the significant effect of gravity-induced tension which is believed to stabilize the upper portion of the flexible pipe. However, the dimensionless formulation introduced in equation (2.1), which included the pipe length, showed a destabilizing effect for the critical flow velocities – refer to

Table A-6. Therefore, the dimensionless v is capable of collapsing the results for different pipe length (L) rather better in comparison to the dimensionless u_i, since it demonstrates the expected stabilizing effect for the critical flow velocities.

3.5 Experimental results for flow separation utilizing pipe III with a coaxially positioned rigid tube of length $L' = 100$ mm.

A number of experiments were organized to examine the effect of flow separation on the dynamical behaviour of the system comprising a short pipe (pipe III), with a 100 mm long plexiglas tube, and a constriction formed by a ring-shaped piece. The effect of flow separation was investigated at both the inlet and outlet of the rigid tube – refer to section 2.3.2 for the experimental setup. The inner diameter of the ring-shaped piece used to form the constriction within the plexiglas tube was $D_{ring} = 20$ mm at the inlet and 32 mm at the outlet, and the thickness was constant in both cases at $t_{ring} = 12$ mm.

3.5.1 Constriction at the inlet (or cantilevered end) of the Plexiglas tube

A leakage flow was created by the formation of a very narrow constriction at the inlet of the rigid tube, i.e., 1 mm between the pipe and ring in all directions. A significant destabilizing effect with regards to critical flow velocity and rms amplitude, i.e., lower U_{cr} and greater amplitude, was observed as a result of the addition of a constriction at the inlet for all U_o/U_i ratios investigated. Moreover, the pattern observed in the experiments with no constriction, for reducing critical flow velocities with increasing U_o/U_i ratio, was preserved. The critical flow velocities for the case with no constriction and an inlet constriction are outlined in dimensional form in Table 3-6 and in dimensionless terms in Table A-7.

For the flow velocity ratio of $U_o/U_i = 0.015$, the trend in the bifurcation diagram for the experiment with an inlet constriction was different from that observed for the case without a constriction, as illustrated in Figure 3-22(a). At low internal flow velocities, no dominant frequency was observed, and hence the weak motions observed were likely turbulence induced. As U_i was increased further, a first-mode frequency around $f_1 \simeq 1.45$ Hz was noticed in the PSD near $U_i = 0.96$ m/s ($u_i = 0.44$) and the pipe became unstable by first-mode flutter at $U_i = 1.41$ m/s ($u_i = 0.65$) as determined by the steeper increase in amplitude. In the proximity of $U_i = 4.42$ m/s ($u_i = 2.02$) a weak second-mode frequency component around $f_2 \simeq 9.38$ Hz was detected in addition to the first-mode frequency and the amplitude of vibration increased at a diminished rate beyond this flow velocity. The first-mode frequency remained dominant with increasing internal flow velocity and the second-mode frequency ($f_2 \simeq 9.38$ Hz) became significant near the end of post-instability 2. In contrast to the case with no constriction, the first-mode component was found to increase in value from 1.45 Hz to 2.50 Hz as U_i increased. The amplitude of oscillations was found to form a plateau at approximately 15 mm for U_i in the range of 12 m/s to 15 m/s ($u_i = 5.50 - 6.87$). Furthermore, the first-mode frequency was found to be nearly constant at $f_1 \simeq 2.40$ Hz in the plateau region. Another way to interpret the $f \simeq 2.50$ Hz is to consider it to be induced by the leakage flow instead of a first-mode frequency. However, in this discussion it will be considered as a first-mode frequency as the value of f_1 was found to increase as U_i increased prior to the addition of the rings – refer to earlier sections.

For higher U_o/U_i ratios, i.e., 0.20 – 0.80, similar rms amplitude growth patterns were observed as for the case with no constriction – refer to Figure 3-22(b-d). A first-mode dominant frequency around $f_1 \simeq 1.50$ Hz was detected in the PSDs and the pipe became unstable by first-mode flutter at 0.14, 0.06, and 0.03 m/s (or $u_i = 0.06$, 0.03, and 0.01) for the flow velocity ratios of 0.20, 0.40, and 0.80, respectively, as illustrated by the sharper increase in amplitude. Mixed-mode oscillations composed of first and weak second-mode frequency components were detected in the vicinity of 0.59, 0.24, and 0.09 m/s (or $u_i = 0.27$, 0.11, and 0.04) for the flow velocity ratios of 0.20, 0.40, and 0.80, consecutively. The magnitude of vibration resumed growth at a diminished rate for all of the high U_o/U_i ratios examined. An interesting observation related to the dominant frequency is that it was found to shift from first to second-mode near the end of post-instability 2, for the high U_o/U_i ratios, as illustrated in Figure 3-23(a). Additionally, a second harmonic of the second-mode frequency, i.e., $2f_2$, was observed at elevated internal flow velocities, i.e., near the end of post-instability 2 – refer to Figure 3-23(b). Moreover, the second-mode frequency ($f_2 \simeq 9.38$ Hz) was detected at significantly lower U_i values as compared to the case without the constriction. It is also worth mentioning that a very weak third-mode frequency was noticed in the PSDs at the maximum attainable U_i for each of $U_o/U_i = 0.20$ and 0.40.

Analogous to the case without a constriction, the nature of the oscillations remained unsteady and disordered as illustrated in Figure 3-23(c-d) for $U_o/U_i = 0.20$. Additionally, the asymmetry of the curves in the phase portrait about the origin has been preserved despite the addition of the constriction. Identical patterns have been observed for $U_o/U_i = 0.40$ and 0.80.

Table 3-6: Comparison of the critical flow velocities (U_i in m/s) for all U_o/U_i ratios examined with pipe III for the cases of no constriction and an inlet constriction.

	No constriction			Constriction at cantilevered end $D_{ring} = 20$ mm		
U_o/U_i	$U_{cr,1}$	$U_{cr,2}$	$U_{cr,3}$	$U_{cr,1}$	$U_{cr,2}$	$U_{cr,3}$
0.015	3.54	4.83	12.86	1.41	4.42	-
0.20	0.39	2.20	-	0.14	0.54	-
0.40	0.21	0.88	-	0.06	0.24	-
0.80	0.10	0.51	-	0.03	0.09	-

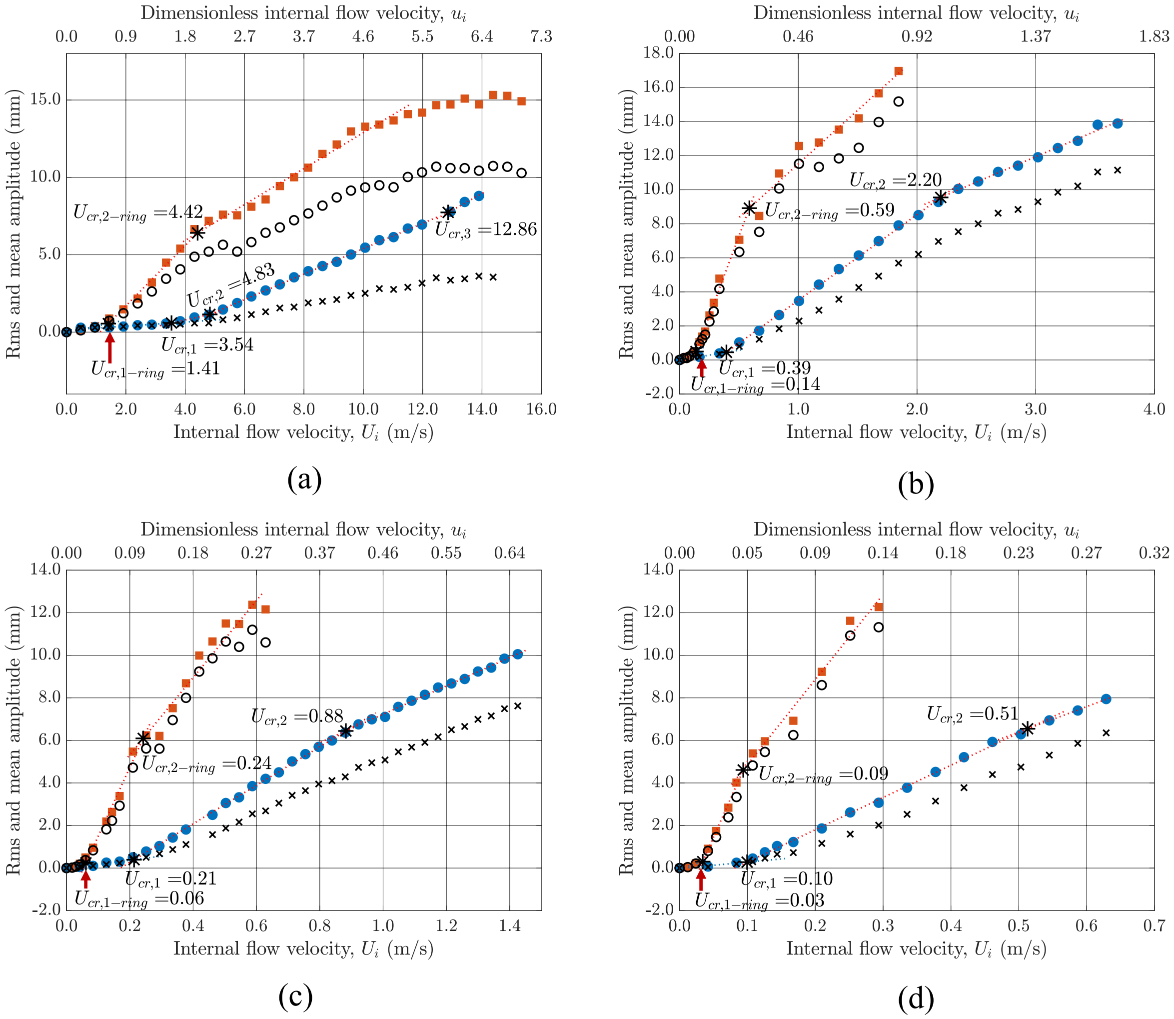

Figure 3-22: Bifurcation diagrams illustrating rms and mean amplitudes of oscillation versus internal flow velocity U_i (or dimensionless internal flow velocity u_i). (a) U_o/U_i = 0.015; (b) U_o/U_i = 0.20; (c)U_o/U_i = 0.40; (d) U_o/U_i = 0.80. Rms amplitude: (●) experiment without a constriction; (■) constriction (ring) at the inlet of the rigid tube; (×) mean deformation for case without a constriction; (○) mean deformation for the case with the constriction at the inlet (pipe III, L' = 100 mm, D_{ch} = 54 mm).

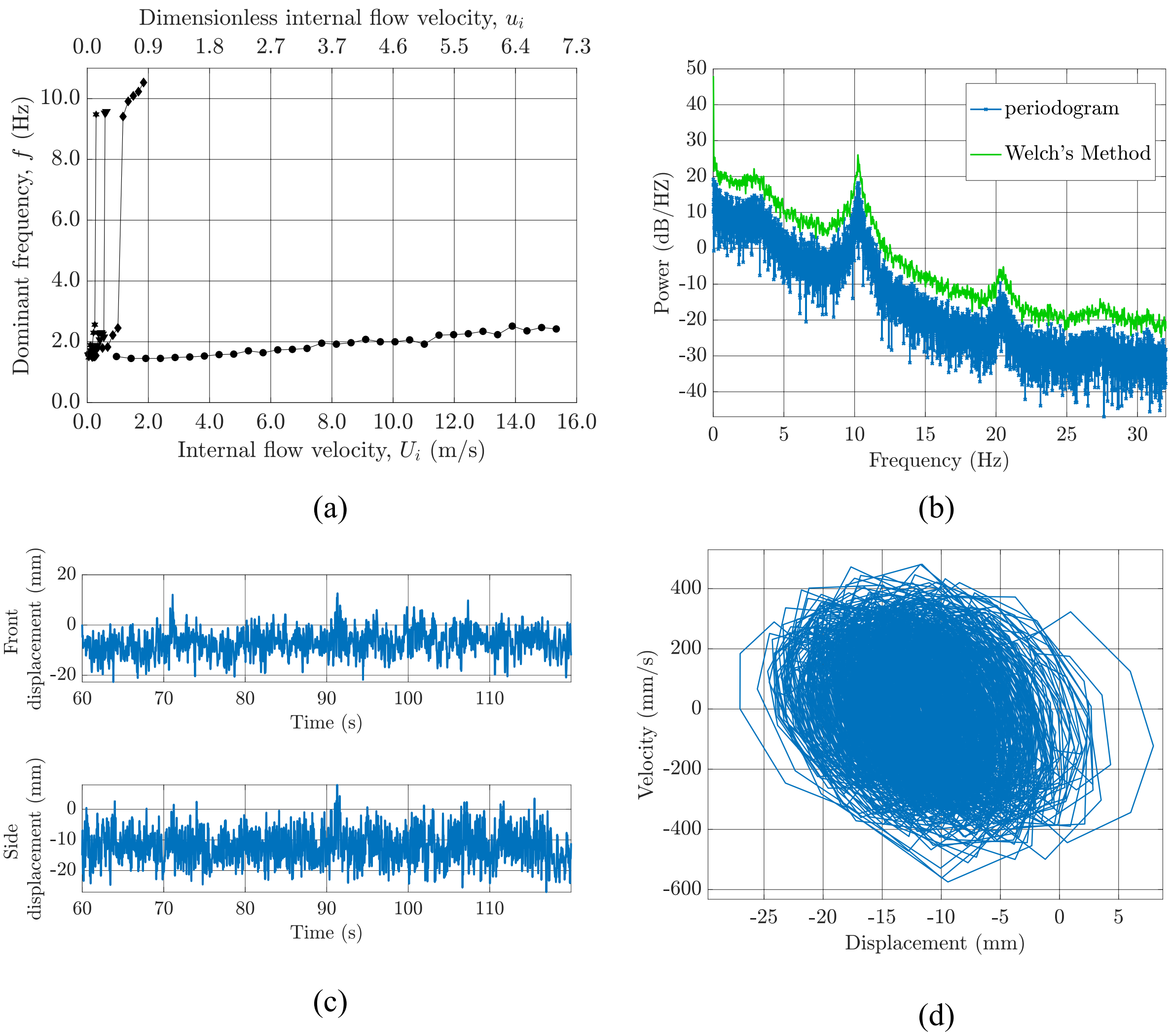

(a)

(b)

(c)

(d)

Figure 3-23: (a) frequency, *f* versus internal flow velocity, U_i (or dimensionless internal flow velocity u_i); (b) PSD, (c) time traces, (d) Phase portrait (side camera) at $U_i = 1.68$ ($u_i = 0.77$) for $U_o/U_i = 0.20$. (●) $U_o/U_i = 0.015$, (◆) $U_o/U_i = 0.20$; (▼) $U_o/U_i = 0.40$, (✱) $U_o/U_i = 0.80$ (pipe III, *L'* = 100 mm, $D_{ring} = 20$ mm - constriction at the cantilevered end).

It is also worth mentioning that multiple ring sizes were considered utilizing pipe I (longer pipe) prior to switching to the shorter pipe. The shorter pipe was used in an effort to increase the critical flow velocities, which were relatively low for the experiments conducted with the longer pipe, such that a definite conclusion could be reached for the effect of flow separation on the critical flow velocities. The effect of multiple D_{ring} sizes varying from 25 mm to 41 mm demonstrated a relatively small stabilizing effect in terms of amplitude (lower amplitude) and no obvious pattern was detected for the critical flow velocities. Experiments were also conducted for D_{ring} = 18 mm and the results were comparable to those for D_{ring} = 20 mm discussed earlier; however, the flow was blocked causing high pressure which moves the ring out of position at very low internal flow velocities. Those results are not included here for brevity.

3.5.2 Constriction at the outlet (or free end) of the plexiglas tube

The external flow passes through the rigid tube over the upper portion of the pipe in the downward direction and then enters a narrower passage near the end of the plexiglas tube. The diameter of the narrow passage formed by the ring-shaped piece is D_{ring} = 32 mm, which is roughly equivalent to the inner diameter of the narrow rigid tube in [90,91].

A prominent stabilizing effect in terms of magnitude of oscillations, i.e., lower magnitude, and a destabilizing effect with respect to critical flow velocities, i.e., lower U_{cr}, for all U_o/U_i ratios examined was observed. The critical flow velocities are organized in dimensional form in Table 3-7 and in non-dimensional form in Table A-8.

For U_o/U_i = 0.015, the pattern in rms amplitude has not been fully conserved as shown in Figure 3-24(a). Overall, the pattern in amplitude is comparable to that of the base case for the narrow rigid tube of D_{ch} = 31.5 mm. A dominant first-mode frequency around $f_1 \simeq 1.55$ Hz was detected in the PSDs and the pipe lost stability via first-mode flutter at U_i = 1.96 (u_i = 0.90) as indicated by the abrupt growth in amplitude shown in Figure 3-24(a). The amplitude of oscillations became nearly constant at 2.5 mm as illustrated by the plateau in the bifurcation diagram for internal flow velocities between 4.79 and 6.71 m/s (u_i = 2.19 – 3.07) – refer to Figure 3-25(a). As U_i was increased further to about 6.93 m/s ($u_i = 3.17$), a weak second-mode frequency component around $f_2 \simeq$ 9.87 Hz was recognized together with the already existing dominant first-mode frequency. Another sharp increase in amplitude was observed as depicted in Figure 3-24(a). In the plateau region, the value of the first-mode frequency component increased from 1.55 to 2.13 Hz with increasing U_i, while it was nearly constant around $f_1 \simeq$ 1.55 Hz in the other regions of the bifurcation diagram as depicted in Figure 3-25(a). Moreover, the second-mode frequency ($f_1 \simeq$ 9.40 Hz) did not materialize in the range of U_i investigated. Additionally, impacting of the pipe on the rim of the outlet ring was also noted and can be seen in the bifurcation diagram through the pause in the rise of the points in the vicinity of $U_i = 11$ m/s ($u_i = 5.04$) in Figure 3-24(a).

The higher U_o/U_i ratios, i.e., 0.20-0.80, for the experiments with the constriction at the free end of the rigid tube demonstrated identical bifurcation diagram trends to those for the case with no constriction as shown in Figure 3-24(b-d). A first-mode frequency ($f_1 \simeq$ 1.55 Hz) appeared in the PSD and the pipe became unsteady due to first-mode flutter at $U_i = 0.20$, 0.14, and 0.04 ($u_i = 0.09$, 0.06, and 0.02) for $U_o/U_i = 0.20$, 0.40, and 0.80, consecutively. A weak superimposed second-mode frequency about $f_2 \simeq$ 9.87 Hz was detected along with the prevalent first-mode component near $U_i = 0.89$, 0.83, and 0.41 m/s ($u_i = 0.41$, 0.38, and 0.19) for $U_o/U_i = 0.20$, 0.40, and 0.80, respectively. Additionally, a very weak third-mode frequency of $f_3 \simeq 25.73$ Hz was noticed near the maximum attainable U_i only in the case for $U_o/U_i = 0.20$; however, for higher U_o/U_i the U_i required to excite higher vibrational modes has not been achieved. Furthermore, the value of the dominant first-mode frequency increased as U_i increased for the high U_o/U_i ratios examined – refer to Figure 3-25(a).

The characteristics of the vibration were found to be unorganized and unsettled, comparable to the case without a constriction as illustrated in Figure 3-25(c,d). Additionally, the asymmetry of the curves in the phase portrait about the origin has been observed, similar to the case with no ring; however, the curves are centered at -3 mm rather than -10 mm for the experiment with no constriction. Analogous patterns have been observed for the other U_o/U_i ratios examined.

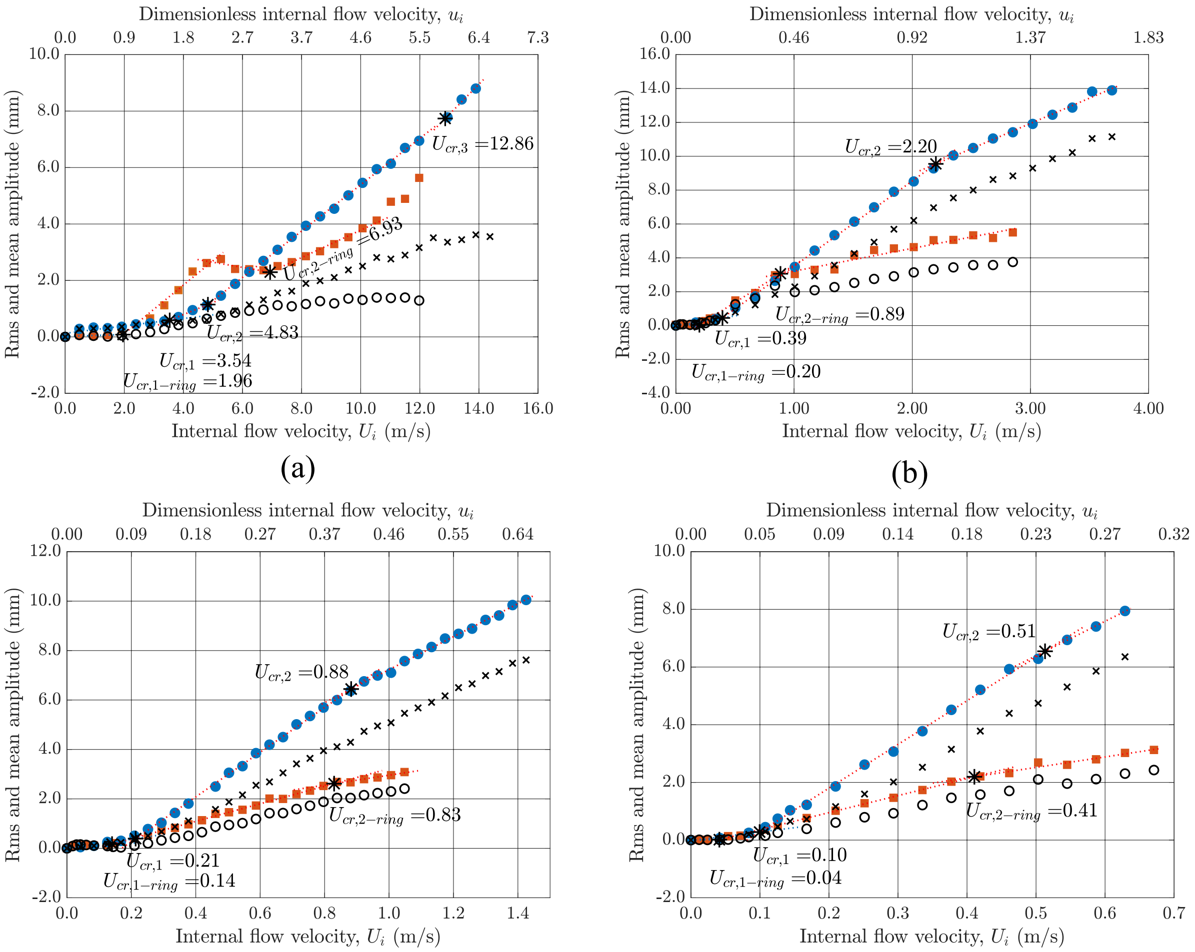

(a) (b)

(c) (d)

Figure 3-24:Bifurcation diagrams illustrating rms and mean amplitudes of oscillation versus internal flow velocity U_i (or dimensionless internal flow velocity u_i). (a) $U_o/U_i = 0.015$; (b) $U_o/U_i = 0.20$; (c)$U_o/U_i = 0.40$; (d) $U_o/U_i = 0.80$. Rms amplitude: (●) experiment without a constriction; (■) constriction (ring) at the free end of the rigid tube; (×) mean deformation for case without a constriction; (○) mean deformation for the case with the constriction at free end of the rigid tube (pipe III, L' = 100 mm, D_{ch} = 54 mm).

It is worth mentioning that due to the stabilizing effect on the amplitude of vibrations in the case of a constriction at the outlet, the determination of the critical flow velocities became significantly more difficult, since the amplitude growth rates are less steep than in the previously discussed cases – refer to Figures 3-22 and 3-24.

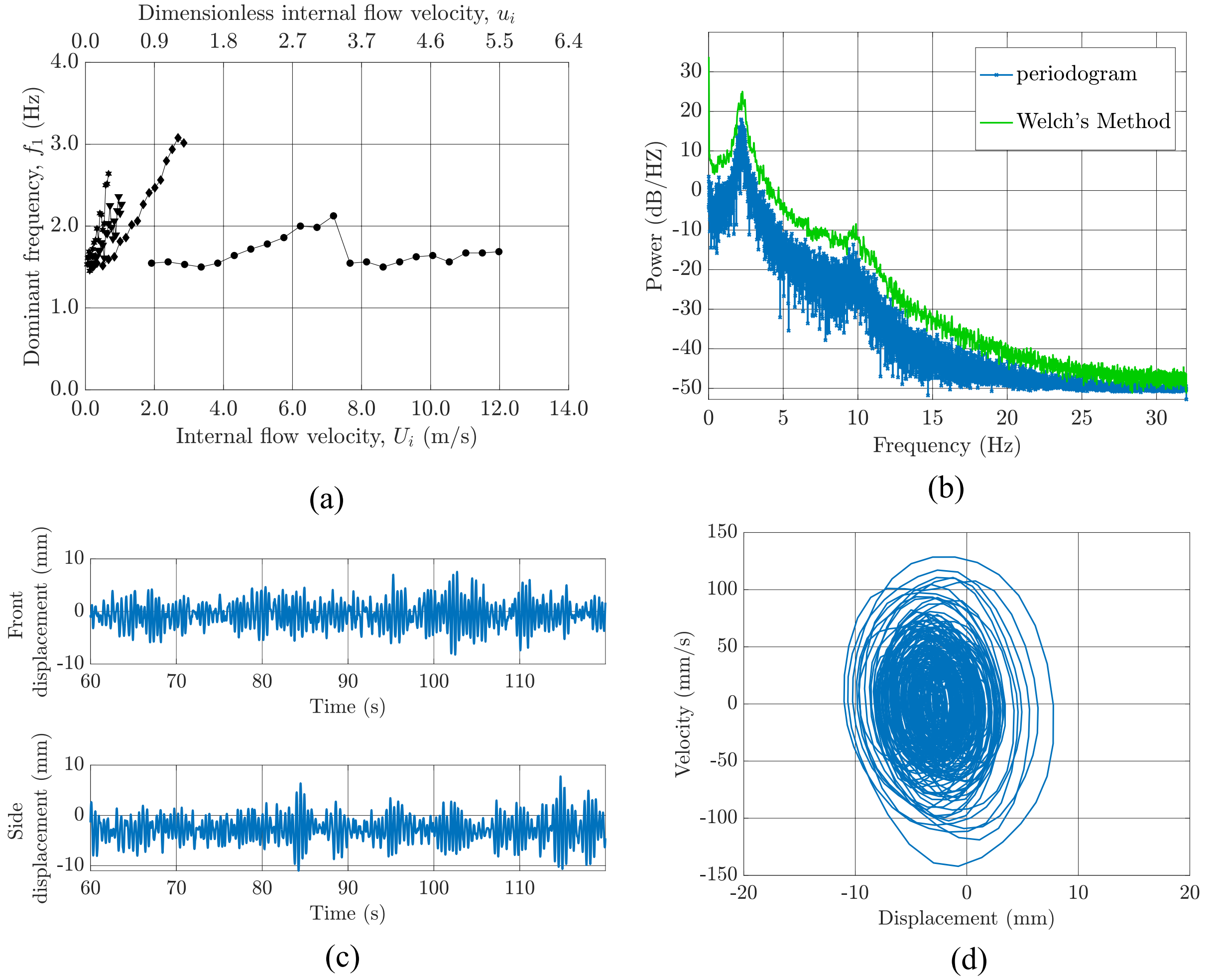

(a)

(b)

(c)

(d)

Figure 3-25: (a) Dominant frequency, f_1 versus internal flow velocity, U_i (or dimensionless internal flow velocity u_i), (b) PSD, (c) time traces; (d) Phase portrait (side camera) at $U_i = 1.68$ ($u_i = 0.77$) for $U_o/U_i = 0.20$. (●) $U_o/U_i = 0.015$, (◆) $U_o/U_i = 0.20$; (▼) $U_o/U_i = 0.40$, (✱) $U_o/U_i = 0.80$ (pipe III, $L' = 100$ mm, $D_{ring} = 20$ mm - constriction at the free end).

Table 3-7: Comparison of the critical flow velocities (U_i in m/s) for all U_o/U_i ratios studied with pipe III for the cases of no constriction and an outlet constriction.

	No constriction			Constriction at free end D_{ring} = 32 mm		
U_o/U_i	$U_{cr,1}$	$U_{cr,2}$	$U_{cr,3}$	$U_{cr,1}$	$U_{cr,2}$	$U_{cr,3}$
0.015	3.54	4.83	12.86	1.96	6.93	-
0.20	0.39	2.20	-	0.20	0.89	-
0.40	0.21	0.88	-	0.14	0.83	-
0.80	0.10	0.51	-	0.04	0.41	-

Discussion of the results on the effect of flow separation at either end of the rigid tube

The effect of a constriction at the inlet (fixed end) or outlet (free end) of the rigid tube is comparable to the work on Pressure Water Reactors (PWR) by Miller [93] discussed in subsection 1.3.5. A constriction at the fixed end for the system generated a destabilizing effect in terms of critical flow velocities and amplitude of oscillations, while an outlet constriction showed a destabilizing effect in terms of critical flow velocities and a stabilizing effect in terms of amplitude of oscillations.

A constriction at the fixed end directs the fluid into a narrow passage of a small flow area and then the flow passes through the wider region of the annulus. The leakage flow mechanism may be explained by considering the creation of a localized valving effect by giving the pipe an instantaneous velocity towards one side of the rigid tube. The flow on that side of the pipe will decelerate as flow area is reduced and it will accelerate on the other side. This results in a variation in the transient static pressure, leading to the generation of a net force directed in the same direction as the instantaneous velocity given to the pipe. Therefore, the pipe may extract energy from the surrounding external flow, making loss of stability by flutter possible, provided that the negative damping is significant in comparison to the positive damping in the system. This mechanism is believed to be responsible for the destabilizing effect in terms of amplitude and critical flow velocities observed in the results presented earlier. The above explanation of the mechanism is based on the external flow only (neglecting internal flow effect) since the addition of the constriction only alters the external flow geometry.

The opposite effect is expected when a constriction is added at the free end/outlet of the annulus since the flow passes from a wider to a narrower region. The pipe is expected to be stabilized for an outlet constriction; however, the stabilizing effect was only observed for the amplitude of oscillation and a destabilizing effect was noticed for critical flow velocities.

Chapter 4 : Conclusion and future work

An experimental investigation has been conducted and discussed in this thesis for the system involving a hanging cantilevered pipe which is partially surrounded by a concentric cantilevered plexiglas tube over its upper portion. Fluid is discharged downwards from the annulus formed by the gap between the pipe and the rigid tube with an external flow velocity U_o and the pipe is aspirating fluid upwards with internal flow velocity U_i. Additionally, fluid flow denoted by Q_a, may be discharged from the bottom of the pressure vessel to achieve higher U_o/U_i ratios than the U_o/U_i ratio determined by continuity for $Q_a = 0$ (see Figure 2-2(a)). The current investigation is concerned with the influence of various system parameters on the onset of instability and post-instability dynamical behaviour of the system. The parameters examined comprise the annular gap size, eccentric positioning the rigid tube relative to the centerline of the flexible pipe and pressure vessel, pipe length, and a constriction at the inlet/outlet of the rigid tube.

4.1 Summary and conclusions

4.1.1 Annular gap size

In the experiments with the wider annular gap (D_{ch} = 54 mm), the aspirating pipe became unstable due to first-mode flutter for all U_o/U_i ratios examined, as was also observed for the narrower annular gap (D_{ch} = 31.5 mm) in both the present investigation and in [90,91]. The bifurcation diagram containing the data for all U_o/U_i ratios, suggested the existence of two distinct dynamical behaviours, specifically for low ($U_o/U_i = 0.015 – 0.06$) and high ($U_o/U_i = 0.20 – 0.80$) flow velocity ratios – refer to Figure 3-12(a). A decreasing trend in critical flow velocities as the U_o/U_i ratio increased was noticed – refer to Tables 3-1 (dimensional) and A-1 (dimensionless).

The base case for the wider annular gap ($Q_a = 0$), represented by $U_o/U_i = 0.015$, demonstrated three distinct sharp increases in rms amplitude, in contrast to the base case for the narrower rigid tube represented by $U_o/U_i = 0.055$ where two sharp increases with a plateau (nearly constant amplitude) in-between has been observed.

For $U_o/U_i = 0.03$ and 0.06, the behaviour was found to be qualitatively similar to that for $U_o/U_i = 0.015$, in terms of amplitude trends, prior to $U_{cr,3}$. However, past $U_{cr,3}$ the rms amplitude was found to increase at a diminished rate.

For the higher U_o/U_i ratios studied (0.20 – 0.80), the bifurcation diagrams illustrated a sharp increase in amplitude of oscillations, followed by a more modest rate of increase in amplitude. On the other hand, for the narrower annular gap there was an increase in amplitude at two distinct increasing rates for the high U_o/U_i ratios. It was also found that the magnitude of oscillations was relatively higher for the wider annular gap in contrast to the narrower one at comparable U_i values.

The dynamics of the system for the high U_o/U_i ratios (0.20 – 0.80) was found to be dependent on the external flow for both annular gap sizes at sufficiently high U_o values – refer to Figure 3-11(b) for $D_{ch} = 54$ mm and in [90,91] for $D_{ch} = 31.5$ mm.

It was found that reducing the annular gap size has a stabilizing effect, with regards to the first critical flow velocity and rms amplitude for comparable flow velocity ratios. On the other hand, a destabilizing effect was noted for the second critical flow velocity. This effect has been observed as the annular gap size was reduced from 54 mm to 31.5 mm and it was preserved as the gap was reduced further to 27 mm. The general behaviour of the motions, which was found to be more severe for higher U_o/U_i ratios, may be described as unsteady and chaotic.

It would be expected that the critical flow velocities would decrease for a narrow annular gap due to the increased added mass effect. However, this was not the case in the current experimental investigation, especially for the first critical flow velocity. The postponing of the first critical flow velocity for narrower annular gaps, could possibly be related to the presence of prevalent unbalanced viscous forces due to the viscosity-related variations in the unsteady pressure field, in comparison to the relatively negligible inviscid flow effect at low internal flow velocities. Moreover, information regarding the nature of the motions (PSDs, phase portraits, time traces, and polar plots) can be found in section 3.1.

4.1.2 Eccentric plexiglas tube with respect to the central aspirating pipe

Experiments were conducted to examine the effect of eccentrically placing the plexiglas tube with respect to the central flexible pipe on the dynamics of the system. The investigation was carried out for two distinct eccentricities, namely t_{gap1} = 10 mm and t_{gap2} = 14 mm, for various U_o/U_i ratios. The bifurcation diagrams demonstrated qualitatively comparable trends to those observed for the concentric placement. The pipe lost stability via first-mode flutter for all U_o/U_i ratios in the eccentric configurations.

The amplitude of oscillations for all U_o/U_i ratios examined increased as eccentricity increased for all regions past the pre-instability (turbulence-induced) flow range. The higher amplitude is mainly due to the relatively larger mean deformation component, in contrast to the oscillatory component which remained nearly constant as eccentricity was increased.

The critical flow velocities for the flow velocity ratio of $U_o/U_i = 0.015$ were found to decrease as eccentricity was increased. The case of $U_o/U_i = 0.20$, demonstrated a decreasing trend for the first critical flow velocity with increasing eccentricity. For $U_o/U_i = 0.40$ and 0.80, no obvious trend was spotted for the first critical flow velocity as eccentricity increased. The second critical flow velocities were delayed for an eccentricity $t_{gap1} = 10$ mm in comparison to the concentric experiments for $U_o/U_i = 0.20 – 0.80$. However, as the eccentricity was increased further to $t_{gap2} = 14$ mm, a small reduction in $U_{cr,2}$ was observed. The decreasing trend in critical flow velocities as U_o/U_i ratios increased was found to hold for an eccentricity of $t_{gap1} = 10$ mm and partially for $t_{gap2} = 14$ mm, where the only flow velocity ratio that did not fit in the trend was $U_o/U_i = 0.20$ – refer to Tables 3-3 (dimensional) and A-3 (dimensionless).

The increased mean deformation observed as the eccentricity was increased may be attributed to the unbalanced external flow distribution about the flexible pipe. The pressure on the side of the pipe closer to the outer tube is higher in comparison to the other side. Hence, a net pressure force towards the side of the pipe with a larger gap would be expected and has been verified experimentally.

An experiment was conducted for a flow velocity ratio of 0.40 and $t_{gap1} = 10$ mm utilizing two cameras positioned at the front window but leveled at different heights to capture the motion at the pipe tip and inside the rigid tube (near its free end) simultaneously. It was found that the pipe exhibited higher signal power, and higher vibrational frequencies (f_2 and f_3) appeared in the data collected from within the rigid tube as compared to those captured at the tip where only weak first-mode frequency components were detected.

In section 3.3, more information regarding the nature of the motions may be found.

4.1.3 Pipe length

A set of experiments was conducted with a shorter pipe to investigate the effect of pipe length on the dynamical behaviour of the aspirating pipe in comparison to the results of the longer pipe. The growth patterns in rms amplitude for the shorter pipe were qualitatively comparable to those for the longer pipe for all U_o/U_i ratios. Moreover, the rms amplitude was found to be equivalent at identical dimensionless internal flow velocities, denoted by u_i (based on equation (2.1)), for all U_o/U_i ratios tested. In dimensional form, the rms amplitudes of the shorter pipe at $U_i = x$ is approximately equal to that for the longer pipe at $U_i = 2x$ for all U_o/U_i ratios tested.

Nevertheless, the critical flow velocities were not halved in dimensional form (U_{cr}) or doubled in dimensionless form (u_{cr}) as the pipe length was doubled – refer to Table 3-4 (dimensional) and Table A-5 (dimensionless) for the critical flow velocity ratios. The critical flow velocities were increased in terms of dimensional internal flow velocity U_i and decreased in terms of dimensionless flow velocity u_i (based on equation (2.1)) as the pipe length was reduced– refer to Tables 3-5 (dimensional) and A-6 (dimensionless). The critical flow velocities and pipe length are considered to be related in a complex way. Moreover, the results showed that as pipe length was halved, the average change in critical flow velocity was around 1.52 for U_{cr} and 0.78 for u_{cr}.

The dimensionless format in equation (2.1) is rather not the best representation of the critical flow velocities, mainly because it demonstrates a destabilizing effect with decreasing pipe length which is the opposite of the expected effect. Therefore, a more reasonable dimensionless form suggested by de Langre et al. [75] was utilized to demonstrate the “stabilizing” abatement effect of increasing length, expected for the critical flow velocities - refer to equation (3.2) and Table A-4. This stabilizing effect noticed with regards to critical flow velocities is believed to be associated with the significant influence of gravity-induced tension on the upper portion of the flexible pipe. Additionally, a description of the nature of the motions can be found in section 3.4.

4.1.4 Flow separation

The effect of flow separation was examined through the addition of a constriction at the fixed and free ends of the rigid tube.

Constriction at the cantilevered end of the plexiglas tube

The constriction at the inlet was formed through the utilization of a ring-shaped piece of internal diameter $D_{ring} = 20$ mm such that the external flow passes from a narrow to a wider region. The pipe became unstable via first-mode flutter for all U_o/U_i ratios with an inlet constriction. A qualitatively different rms amplitude trend has been observed for the case of $U_o/U_i = 0.015$, while the trend was preserved for other flow velocity ratios.

A destabilizing effect was noticed for all U_o/U_i ratios examined, in terms of higher rms amplitudes and lower critical flow velocities in comparison to the case without flow separation. The critical flow velocities were also found to decrease as U_o/U_i increased – refer to Tables 3-6 (dimensional) and A-7 (dimensionless).

The bifurcation diagram for the flow velocity ratio of $U_o/U_i = 0.015$ with an inlet constriction demonstrated a sharp increase in amplitude, past the turbulence-induced region, followed by an increase at a diminished rate and a plateau (constant amplitude), consecutively.

Constriction at the free end of the plexiglas tube

A constriction at the outlet of the rigid tube was formed by the addition of a ring-shaped piece of internal diameter D_{ring} = 32 mm such that the external flow passes from the wider upper portion surrounding the pipe into a narrower region. The pipe was found to lose stability by first-mode flutter for all U_o/U_i ratios with an outlet constriction.

The magnitude of oscillations was relatively lower and the critical flow velocities were reduced for all U_o/U_i ratios examined when an outlet constriction was included. As U_o/U_i was increased, the critical flow velocities were found to decrease – refer to Tables 3-7 (dimensional) and A-8 (dimensionless).

For the flow velocity ratio of $U_o/U_i = 0.015$, the bifurcation diagram with the outlet constriction was comparable to that for the base case ($U_o/U_i = 0.055$) for the narrower rigid tube (D_{ch} = 31.5 mm) in terms of the presence of a plateau between two sharp increases in amplitude.

For U_o/U_i = 0.20-0.80 similar amplitude growth patterns were observed as in the experiments without a ring.

The effect of flow separation discussed in this thesis is explainable by considering a localized valving effect formed by giving the pipe an instantaneous velocity towards one side of the outer tube. This leads to the deceleration of the flow on that side of the pipe as the flow area is reduced and the flow accelerates on the other sides of the pipe. This results in a variation in the transient static pressure leading to the generation of a net force directed in the same direction as the instantaneous velocity experienced by the pipe. Therefore, the pipe becomes capable of extracting energy from the surrounding flow and may lose stability by flutter.

The effect is expected to be reversed if the constriction is placed at the outlet of the rigid tube. In other words, the pipe should be stabilized in terms of amplitude of oscillations and critical flow velocities. However, in the current investigation only the amplitude of oscillations was reduced. Section 3.5 contains additional information pertaining to the characteristics of the motion.

Table 4-1: Summary of the results showing the influence on critical flow velocities for all parameters.

	U_o/U_i	Effect of	$U_{cr,1}$	$U_{cr,2}$	$U_{cr,3}$
Annular confinement	0.015 – 0.06	Reducing D_{ch} from 54 mm to 27 mm	-	-	-
	0.20 – 0.80		↗	↘	-
Eccentricity	0.015	Increasing t_{gap} from 0 mm to 14 mm	↘	↘	↘
	0.20 – 0.80		Nearly constant	↗ then ↘	-
Pipe length	0.015	Reducing L from 441 mm to 221 mm	↗	↗	↗
	0.20 – 0.80		↗	↗	-
Inlet constriction	0.015	Adding D_{ring} = 20 mm	↘	↘	-
	0.20 – 0.80		↘	↘	-
Outlet constriction	0.015	Adding D_{ring} = 32 mm	↘	↗	-
	0.20 – 0.80		↘	↘	-

Enhancing the design of solution-mined caverns

According to the experimental results presented in this thesis, possible design improvements for solution-mined caverns include the utilization of a narrower rigid casing to postpone the onset of instability – refer to Table 4-1. However, this will come with the drawback of earlier impacting of the brine-string with the rim of the surrounding casing. Another proposal could be the addition of a constriction at the free end of the rigid casing to reduce the intensity of the motions; however, this may not be an optimal solution due to the possible destabilizing effect on the onset of instability as illustrated in Table 4-1. These proposals are based on the results of experiments conducted for the flow configuration representative of the storage mode of solution-mined caverns. Prior to making any modifications to the design of the system, the effect of the reverse flow configuration, i.e., production mode, must be taken into consideration. Modifications to this system are rather complicated as they must be optimized for both operation modes. Moreover, the results of the eccentricity experiments have also shown that the system is very sensitive to relatively small geometrical imperfections with regards to the onset of instability and intensity of vibrations.

4.2 Future work

It would be interesting to investigate the effect of confinement analytically utilizing the current linear model to determine the degree of agreement with the current experimental results. This will aid in understanding the dynamics of the system, as very narrow annular gap sizes are difficult to study experimentally due to the expected impacting of the flexible pipe with the rim of the outer tube.

It might also be interesting to examine the influence of varying the length of the wider rigid tube (D_{ch} = 54 mm) to compare to the results obtained for different shorter rigid tube lengths [90,91], i.e., effect of r_{ann}.

The system was investigated theoretically by a linear model, which provided a reasonable prediction for the first critical flow velocity [90,92]. However, given the new experimental findings the model should be extended to account for non-linear terms to better represent the system under consideration. Moreover, the model should account for eccentricity to verify the experimental findings and help in understanding the effect of eccentricity on critical flow velocities, especially for high U_o/U_i ratios in which loss of stability occurred at very low flow velocities.

It would be beneficial to examine theoretically the effect of a very long brine-string on the dynamics of the system, since it is not possible to study it experimentally with the relatively small bench-top apparatus.

It would also be of interest to study experimentally and analytically the influence of a curved pipe on the onset of instability and post-instability dynamical behaviour of the system.

References

[1] H.-J. Bungartz and M. Schäfer. *Fluid-Structure Interaction: Modelling, Simulation, Optimisation*. Berlin: Springer-Verlag, 2006.

[2] O. C. Zienkiewicz, R. L. Taylor, and P. Nithiarasu. *The finite element method for fluid dynamics*. Oxford: Butterworth-Heinemann, 2014.

[3] L. Wang and Q. Ni. Vibration of slender structures subjected to axial flow or axially towed in quiescent fluid. *Advances in Acoustics and Vibration*, vol. 2009, pp. 1–19, 2009.

[4] M. P. Païdoussis. *Fluid-Structure Interactions: Slender Structures and Axial Flow*. Vol. 1 (Second Edition), Academic Press, 2014.

[5] M. J. Hannoyer and M. P. Païdoussis. Instabilities of tubular beams simultaneously subjected to internal and external axial flows. *Journal of Mechanical Design*, vol. 100, no. 2, pp. 328–336, 1978.

[6] M. P. Païdoussis, T. P. Luu, and S. Prabhakar. Dynamics of a long tubular cantilever conveying fluid downwards, which then flows upwards around the cantilever as a confined annular flow. *Journal of Fluids and Structures*, vol. 24, no. 1, pp. 111–128, 2008.

[7] W. Huang, D. Gao, S. Wei, and X. Li. A generalized quasi-static model of Drill String System. *Journal of Natural Gas Science and Engineering*, vol. 23, pp. 208–220, 2015.

[8] M. P. Païdoussis. 1992 Calvin Rice Lecture: Some curiosity-driven research in fluid structure interactions and its current applications. *Journal of Pressure Vessel Technology*, vol. 115, no. 1, pp. 2–14, 1993.

[9] X. Ge, Y. Li, X. Chen, X. Shi, H. Ma, H. Yin, N. Zhang, and C. Yang. Dynamics of a partially confined, vertical upward-fluid-conveying, slender cantilever pipe with reverse external flow. *Applied Sciences*, vol. 9, no. 7, p. 1425, 2019.

[10] S. Mokhatab, W. A. Poe, and J. Mak, *Handbook of Natural Gas Transmission and processing: Principles and practices*. Cambridge, MA: Gulf Professional Publishing, pp. 1-35, 2019.

[11] P. Bérest, A. Réveillère, D. Evans, and M. Stöwer. Review and analysis of historical leakages from Storage Salt Caverns wells. *Oil & Gas Science and Technology – Revue d'IFP Energies nouvelles*, vol. 74, p. 27, 2019.

[12] K. Moditis, M. Païdoussis, and J. Ratigan. Dynamics of a partially confined, discharging, cantilever pipe with reverse external flow. *Journal of Fluids and Structures*, vol. 63, pp. 120–139, 2016.

[13] M.P. Païdoussis. *Fluid-Structure Interactions: Slender Structures and Axial Flow*. Vol. 2 (Second Edition), Academic Press, 2016.

[14] F.-J. Bourrières. Sur un phénomène d'oscillation auto-entretenue en mécanique des fluides réels, E. Blondel La Rougery, 1939.

[15] H. Ashley and G. Haviland. Bending vibrations of a pipe line containing flowing fluid. *Journal of Applied Mechanics*, vol. 17, no. 3, pp. 229–232, 1950.

[16] V.P. Feodos'ev. Vibrations and stability of a pipe when liquid flows through it. *Znzhenernyi Sbornik* 10**,** 169-170, 1951.

[17] G.W. Housner. Bending vibrations of a pipe line containing flowing fluid. *Journal of Applied Mechanics*, vol. 19, no. 2, pp. 205–208, 1952.

[18] R.H. Long. Experimental and theoretical study of transverse vibration of a tube containing flowing fluid. *Journal of Applied Mechanics*, vol. 22, no. 1, pp. 65–68, 1955.

[19] G.H. Handelman. A note on the transverse vibration of a tube containing flowing fluid, *Quarterly of Applied Mathematics*, vol. 13, no. 3, pp. 326–330, 1955.

[20] F.I. Niordson. Vibrations of a cylindrical tube containing flowing fluid. *Kungliga Tekniska Hogskolans Handlingar (Stockholm)* No. 73, 1953.

[21] T.B. Benjamin. Dynamics of a system of articulated pipes conveying fluid - I.theory. *Proceedings of the Royal Society of London. Series A. Mathematical and Physical Sciences*, vol. 261, no. 1307, pp. 457–486, 1961.

[22] T.B. Benjamin. Dynamics of a system of articulated pipes conveying fluid - II. experiments. *Proceedings of the Royal Society of London. Series A. Mathematical and Physical Sciences*, vol. 261, no. 1307, pp. 487–499, 1961.

[23] R.W. Gregory, M. P. Païdoussis. Unstable oscillation of tubular cantilevers conveying fluid I. theory. *Proceedings of the Royal Society of London. Series A. Mathematical and Physical Sciences*, vol. 293, no. 1435, pp. 512–527, 1966.

[24] R.W. Gregory, M. P. Païdoussis. Unstable oscillation of tubular cantilevers conveying fluid II. experiments. *Proceedings of the Royal Society of London. Series A. Mathematical and Physical Sciences*, vol. 293, no. 1435, pp. 528–542, 1966.

[25] M.P. Païdoussis. Dynamics of tubular cantilevers conveying fluid. *Journal of Mechanical Engineering Science*, vol. 12, no. 2, pp. 85–103, 1970.

[26] R.A. Stein and M. W. Tobriner. Vibration of pipes containing flowing fluids. *Journal of Applied Mechanics*, vol. 37, no. 4, pp. 906–916, 1970.

[27] M.P. Païdoussis and J.-P. Denise. Flutter of cylindrical shells conveying fluid. *Journal of Sound and Vibration*, vol. 16, no. 3, pp. 459–461, 1971.

[28] M.P. Païdoussis and J.-P. Denise. Flutter of thin cylindrical shells conveying fluid. *Journal of Sound and Vibration*, vol. 20, no. 1, pp. 9–26, 1972.

[29] L.K. Shayo and C. H. Ellen. Theoretical studies of internal flow-induced instabilities of cantilever pipes. *Journal of Sound and Vibration*, vol. 56, no. 4, pp. 463–474, 1978.

[30] M.P. Païdoussis and N. T. Issid. Dynamic stability of pipes conveying fluid. *Journal of Sound and Vibration*, vol. 33, no. 3, pp. 267–294, 1974.

[31] R. Shilling and Y.K. Lou. An experimental study on the dynamic response of a vertical cantilever pipe conveying fluid. *Journal of Energy Resources Technology*, vol. 102, no. 3, pp. 129–135, 1980.

[32] A.L. Thurman and C. D. Mote. Nonlinear oscillation of a cylinder containing a flowing fluid. *Journal of Engineering for Industry*, vol. 91, no. 4, pp. 1147–1155, 1969.

[33] P.J. Holmes. Bifurcations to divergence and flutter in flow-induced oscillations: A finite dimensional analysis. *Journal of Sound and Vibration*, vol. 53, no. 4, pp. 471–503, 1977.

[34] P.J. Holmes. Pipes supported at both ends cannot flutter. *Journal of Applied Mechanics*, vol. 45, no. 3, pp. 619–622, 1978.

[35] P. Holmes and J. Marsden, "Bifurcation to divergence and flutter in flow-induced oscillations: An infinite dimensional analysis," *Automatica*, vol. 14, no. 4, pp. 367–384, 1978.

[36] J. Rousselet and G. Herrmann. Flutter of articulated pipes at finite amplitude. *Journal of Applied Mechanics*, vol. 44, no. 1, pp. 154–158, 1977.

[37] J. Rousselet and G. Herrmann. Dynamic behavior of continuous cantilevered pipes conveying fluid near critical velocities. *Journal of Applied Mechanics*, vol. 48, no. 4, pp. 943–947, 1981.

[38] T.S. Lundgren, P. R. Sethna, and A. K. Bajaj. Stability boundaries for flow induced motions of tubes with an inclined terminal nozzle. *Journal of Sound and Vibration*, vol. 64, no. 4, pp. 553–571, 1979.

[39] A.K. Bajaj, P. R. Sethna, and T. S. Lundgren. Hopf bifurcation phenomena in tubes carrying a fluid. *SIAM Journal on Applied Mathematics*, vol. 39, no. 2, pp. 213–230, 1980.

[40] M.P. Païdoussis and F. C. Moon. Nonlinear and chaotic fluidelastic vibrations of a flexible pipe conveying fluid. *Journal of Fluids and Structures*, vol. 2, no. 6, pp. 567–591, 1988.

[41] C. Semler. Nonlinear dynamics and chaos of a pipe conveying fluid. Ph.D. Thesis, Department of Mechanical Engineering, McGill University, 1991.

[42] C. Semler, G. X. Li, and M.P. Païdoussis. The non-linear equations of motion of pipes conveying fluid. *Journal of Sound and Vibration*, vol. 169, no. 5, pp. 577–599, 1994.

[43] M.P. Païdoussis and C. Semler. Nonlinear and chaotic oscillations of a constrained cantilevered pipe conveying fluid: A full nonlinear analysis. *Nonlinear Dynamics*, vol. 4, no. 6, pp. 655–670, 1993.

[44] G.S. Copeland and F. C. Moon. Chaotic flow-induced vibration of a flexible tube with end mass. *Journal of Fluids and Structures*, vol. 6, no. 6, pp. 705–718, 1992.

[45] M. Wadham-Gagnon, M. P. Païdoussis, and C. Semler. Dynamics of cantilevered pipes conveying fluid. part 1: Nonlinear equations of three-dimensional motion. *Journal of Fluids and Structures*, vol. 23, no. 4, pp. 545–567, 2007.

[46] M.P. Païdoussis, C. Semler, M. Wadham-Gagnon, and S. Saaid. Dynamics of cantilevered pipes conveying fluid. part 2: Dynamics of the system with Intermediate Spring Support. *Journal of Fluids and Structures*, vol. 23, no. 4, pp. 569–587, 2007.

[47] Y. Modarres-Sadeghi, C. Semler, M. Wadham-Gagnon, and M. P. Païdoussis. Dynamics of cantilevered pipes conveying fluid. part 3: Three-dimensional dynamics in the presence of an end-mass. *Journal of Fluids and Structures*, vol. 23, no. 4, pp. 589–603, 2007.

[48] Y. Modarres-Sadeghi, M. P. Païdoussis, and C. Semler. Three-dimensional oscillations of a cantilever pipe conveying fluid. *International Journal of Non-Linear Mechanics*, vol. 43, no. 1, pp. 18–25, 2008.

[49] A. Sarkar and M.P. Païdoussis. A compact limit-cycle oscillation model of a cantilever conveying fluid. *Journal of Fluids and Structures*, vol. 17, no. 4, pp. 525–539, 2003.

[50] L. Wang, T. L. Jiang, and H. L. Dai. Three-dimensional dynamics of supported pipes conveying fluid. *Acta Mechanica Sinica*, vol. 33, no. 6, pp. 1065–1074, 2017.

[51] J. Duan, K. Chen, Y. You, R. Wang, and J. Li. Three-dimensional dynamics of vortex-induced vibration of a pipe with internal flow in the subcritical and supercritical regimes. *International Journal of Naval Architecture and Ocean Engineering*, vol. 10, no. 6, pp. 692–710, 2018.

[52] M.P. Païdoussis and T. P. Luu. Dynamics of a pipe aspirating fluid such as might be used in Ocean Mining. *Journal of Energy Resources Technology*, vol. 107, no. 2, pp. 250–255, 1985.

[53] M.P. Païdoussis. Aspirating pipes do not flutter at infinitesimally small flow. *Journal of Fluids and Structures*, vol. 13, no. 3, pp. 419–425, 1999.

[54] G.L. Kuiper and A. V. Metrikine. Dynamic stability of a submerged, free-hanging riser conveying fluid. *Journal of Sound and Vibration*, vol. 280, no. 3-5, pp. 1051–1065, 2005.

[55] M.P. Païdoussis, C. Semler, and M. Wadham-Gagnon. A reappraisal of why aspirating pipes do not flutter at Infinitesimal Flow. *Journal of Fluids and Structures*, vol. 20, no. 1, pp. 147–156, 2005.

[56] G.L. Kuiper and A. V. Metrikine. Experimental investigation of dynamic stability of a cantilever pipe aspirating fluid. *Journal of Fluids and Structures*, vol. 24, no. 4, pp. 541–558, 2008.

[57] S. Rinaldi. Experiments on the Dynamics of cantilevered pipes subjected to internal and/or external axial flow (Master's thesis). Department of Mechanical Engineering, McGill University, 2009.

[58] D.B. Giacobbi. The Dynamics of Aspirating Cantilevered Pipes and Pipes Conveying Variable Density Fluid (Master's thesis). Department of Mechanical Engineering, McGill University, 2010.

[59] M.P. Païdoussis and M. Tétreault-Friend. Aspirating Cantilevers and reverse sprinklers. *American Journal of Physics*, vol. 77, no. 4, pp. 349–353, 2009.

[60] D.B. Giacobbi, S. Rinaldi, C. Semler, and M. P. Païdoussis. The dynamics of a cantilevered pipe aspirating fluid studied by experimental, numerical and analytical methods. *Journal of Fluids and Structures*, vol. 30, pp. 73–96, 2012.

[61] W. R. Hawthorne. The early development of the Dracone flexible barge. *Proceedings of the Institution of Mechanical Engineers*, vol. 175, no. 1, pp. 52–83, 1961.

[62] M. P. Païdoussis. Dynamics of flexible slender cylinders in axial flow part 1. Theory. *Journal of Fluid Mechanics*, vol. 26, no. 4, pp. 717–736, 1966.

[63] M.P. Païdoussis. Dynamics of flexible slender cylinders in axial flow part 2. Experiments. *Journal of Fluid Mechanics*, vol. 26, no. 4, pp. 737–751, 1966.

[64] M.P. Païdoussis. Stability of towed, totally submerged flexible cylinders. *Journal of Fluid Mechanics*, vol. 34, no. 2, pp. 273–297, 1968.

[65] C.R. Ortloff and J. Ives. On the dynamic motion of a thin flexible cylinder in a viscous stream. *Journal of Fluid Mechanics*, vol. 38, no. 4, pp. 713–720, 1969.

[66] H.P. Pao. Dynamical stability of a towed thin flexible cylinder. *Journal of Hydronautics*, vol. 4, no. 4, pp. 144–150, 1970.

[67] M.P. Païdoussis. Dynamics of submerged towed cylinders. Eighth Symposium on Naval Hydrodynamics: Hydrodynamics in the Ocean Environment. Office of Naval Research, U.S. Department of the Navy ARC-179, pp. 981-1016, 1970.

[68] M. P. Païdoussis. Dynamics of cylindrical structures subjected to axial flow. *Journal of Sound and Vibration*, vol. 29, no. 3, pp. 365–385, 1973.

[69] M. P. Païdoussis and M. J. Pettigrew. Dynamics of flexible cylinders in axisymmetrically confined axial flow. *Journal of Applied Mechanics*, vol. 46, no. 1, pp. 37–44, 1979.

[70] M. P. Païdoussis, D. Mateescu, and W.-G. Sim. Dynamics and stability of a flexible cylinder in a narrow coaxial cylindrical duct subjected to annular flow. *Journal of Applied Mechanics*, vol. 57, no. 1, pp. 232–240, 1990.

[71] G. S. Triantafyllou and C. Chryssostomidis. Analytic determination of the buckling speed of towed slender cylindrical beams. ASME *Journal of Energy Resources Technology*, vol. 106, no. 2, pp. 246–249, 1984.

[72] G. S. Triantafyllou and C. Chryssostomidis. Stability of a string in axial flow. ASME *Journal of Energy Resources Technology*, vol. 107, no. 4, pp. 421–425, 1985.

[73] A. P. Dowling. The dynamics of towed flexible cylinders Part 1. neutrally buoyant elements. *Journal of Fluid Mechanics*, vol. 187, pp. 507–532, 1988.

[74] A. P. Dowling. The dynamics of towed flexible cylinders Part 2. negatively buoyant elements. *Journal of Fluid Mechanics*, vol. 187, pp. 533–571, 1988.

[75] E. de Langre, M. P. Païdoussis, O. Doaré, and Y. Modarres-Sadeghi. Flutter of long flexible cylinders in axial flow, *Journal of Fluid Mechanics*, vol. 571, pp. 371–389, 2007.

[76] O. Doaré and E. de Langre. The flow-induced instability of long hanging pipes. *European Journal of Mechanics - A/Solids*, vol. 21, no. 5, pp. 857–867, 2002.

[77] M. Kheiri, M. P. Païdoussis, and M. Amabili. A nonlinear model for a towed flexible cylinder. *Journal of Sound and Vibration*, vol. 332, no. 7, pp. 1789–1806, 2013.

[78] M. Kheiri, M. P. Païdoussis, and M. Amabili. An experimental study of dynamics of towed flexible cylinders. *Journal of Sound and Vibration*, vol. 348, pp. 149–166, 2015.

[79] M. Kheiri, M.P. Païdoussis, Linear dynamics and stability of a towed flexible cylinder, in Proceedings of 23rd CANCAM, Vancouver, BC, Canada, pp. 263–266, 2011.

[80] S. Rinaldi and M. P. Païdoussis. Theory and experiments on the dynamics of a free-clamped cylinder in confined axial air-flow. *Journal of Fluids and Structures*, vol. 28, pp. 167–179, 2012.

[81] S. Rinaldi and M. P. Païdoussis. An improved theoretical model for the dynamics of a free-clamped cylinder in axial flow. *Journal of Fluids and Structures*, vol. 94, p. 102903, 2020.

[82] M. Tavallaeinejad, M. P. Païdoussis, and M. Legrand. Nonlinear static response of low-aspect-ratio inverted flags subjected to a steady flow. *Journal of Fluids and Structures*, vol. 83, pp. 413–428, 2018.

[83] M. P. Païdoussis, E. Grinevich, D. Adamovic, C. Semler, Linear and nonlinear dynamics of cantilevered cylinders in axial flow. Part 1: Physical dynamics. *Journal of Fluids and Structures*, vol. 16, no. 6, pp. 691–713, 2002.

[84] J.-L. Lopes, M. P. Païdoussis, C. Semler, Linear and nonlinear dynamics of cantilevered cylinders in axial flow. Part 2: The equations of motion. *Journal of Fluids and Structures*, vol. 16, no. 6, pp. 715–737, 2002.

[85] C. Semler, J.-L. Lopes, N. Augu, M. P. Païdoussis, Linear and nonlinear dynamics of cantilevered cylinders in axial flow. Part 3: Nonlinear dynamics. *Journal of Fluids and Structures*, vol. 16, no. 6, pp. 739–759, 2002.

[86] F. Cesari, S. Curioni. Buckling instability in tubes subject to internal and external axial fluid flow. In Proceedings of the 4th Conference on Dimensioning. Budapest: Hungarian Academy of Science. pp. 301–311, 1971.

[87] Q. Qian, L. Wang, and Q. Ni. Vibration and stability of vertical upward-fluid-conveying pipe immersed in rigid cylindrical channel. *Acta Mechanica Solida Sinica*, vol. 21, no. 5, pp. 431–440, 2008.

[88] A. R. Abdelbaki, M. P. Païdoussis, and A. K. Misra. A nonlinear model for a hanging cantilevered pipe discharging fluid with a partially-confined external flow. *International Journal of Non-Linear Mechanics*, vol. 118, p. 103290, 2020.

[89] M. Chehreghani, A. R. Abdelbaki, A. K. Misra, and M. P. Païdoussis. Experiments on the dynamics of a cantilevered pipe conveying fluid and subjected to reverse annular flow. *Journal of Sound and Vibration*, vol. 515, p. 116480, 2021.

[90] M.F.J. Butt. The Dynamics of Hanging Tubular Cantilevers Simultaneously Subjected to Internal and External Axial Flows (PhD thesis). Department of Mechanical Engineering, McGill University, 2022.

[91] M. F. J. Butt, M. P. Païdoussis, and M. Nahon. Dynamics of a confined pipe aspirating fluid and concurrently subjected to external axial flow: An experimental investigation. *Journal of Fluids and Structures*, vol. 104, p. 103299, 2021.

[92] M. F. J. Butt, M. P. Païdoussis, and M. Nahon. Dynamics of a confined pipe aspirating fluid and concurrently subjected to external axial flow: A theoretical investigation. *Journal of Sound and Vibration*, vol. 509, p. 116148, 2021.

[93] M. P. Païdoussis. Flow-Induced Vibrations in Nuclear Reactors and Heat Exchangers: Practical Experiences and State of Knowledge, Practical Experiences with Flow Induced Vibrations (eds. Naudascher, E. & Rockwell, D.), pp.1-81, Berlin, Springer-Verlag, 1980.

[94] D.R. Miller. Generation of positive and negative damping with a flow restrictor in axial flow. In *Proceedings of the Conference on Flow-Induced Vibrations in Reactor System Components* (eds G.S. Rosenberg, M.W. Wambsganss & R.P. Carter), Report ANL-7685, pp. 304-311, Argonne National Laboratory, Argonne, IL, U.S.A, 1970.

[95] T.M. Mulcahy. A review of leakage-flow-induced vibrations of reactor components. Report ANL-83-43, Argonne National Laboratory, Argonne, IL, U.S.A, 1983a.

[96] T.M. Mulcahy. Avoiding leakage flow-induced vibration by a tube-in-tube slip joint. Report ANL-84-82, Argonne National Laboratory, Argonne, IL, U.S.A. Also in *Fluid-Structure Interaction and Aerodynamic Damping* (eds E.H. Dowell & M.K. Au-Yang), pp. 159-169, 1985, ASME: New York, 1984.

[97] T.M. Mulcahy. Leakage-flow-induced vibrations of reactor components. *The Shock and Vibration Digest* 15(9), pp. 11-18, 1983b.

[98] D.E. Hobson. Fluid-elastic instabilities caused by flow in an annulus. *Proceedings of 3rd International Conference on Vibration in Nuclear Plant*, Keswick, pp. 440-463. London: BNES. 1982.

[99] D. Mateescu and M. P. Païdoussis. The unsteady potential flow in an axially variable annulus and its effect on the dynamics of the Oscillating Rigid Center-body. *Journal of Fluids Engineering*, vol. 107, no. 3, pp. 421–427, 1985.

[100] D. Mateescu and M. P. Païdoussis. Unsteady viscous effects on the annular-flow-induced instabilities of a rigid cylindrical body in a narrow duct. *Journal of Fluids and Structures*, vol. 1, no. 2, pp. 197–215, 1987.

[101] D. Mateescu, M. P. Païdoussis, and F. Bélanger. Unsteady pressure measurements on an oscillating cylinder in narrow annular flow. *Journal of Fluids and Structures*, vol. 2, no. 6, pp. 615–628, 1988.

[102] T. M. Mulcahy. One-dimensional leakage-flow vibration instabilities. *Journal of Fluids and Structures*, vol. 2, no. 4, pp. 383–403, 1988.

[103] F. Inada and S. Hayama. A study on leakage-flow-induced vibrations. fluid-dynamic forces acting on the walls of a one-dimensional, narrow passage. *JSME international journal. Ser. 3, Vibration, control engineering, engineering for industry*, vol. 31, no. 1, pp. 39–47, 1988.

[104] F. Inada and S. Hayama. A study on leakage-flow-induced vibrations. part 1: Fluid-dynamic forces and moments acting on the walls of a narrow tapered passage. *Journal of Fluids and Structures*, vol. 4, no. 4, pp. 395–412, 1990.

[105] F. Inada and S. Hayama. A study on leakage-flow-induced vibrations. part 2: Stability Analysis and experiments for two-degree-of-freedom systems combining translational and rotational motions. *Journal of Fluids and Structures*, vol. 4, no. 4, pp. 413–428, 1990.

Appendix A

Table A-1: Summary of results listing the dimensionless critical flow velocities u_i for all U_o/U_i (u_o/u_i) ratios investigated for the annular gap size study with pipe I.

		D_{ch} = 54 mm			D_{ch} = 31.5 mm			D_{ch} = 27 mm		
U_o/U_i	u_o/u_i	$u_{cr,1}$	$u_{cr,2}$	$u_{cr,3}$	$u_{cr,1}$	$u_{cr,2}$	$u_{cr,3}$	$u_{cr,1}$	$u_{cr,2}$	$u_{cr,3}$
0.015	0.038	2.11	3.79	6.66	-	-	-	-	-	-
0.03	0.08	1.02	2.43	4.40	-	-	-	-	-	-
0.055	0.139	-	-	-	1.00	3.76	-	-	-	-
0.06	0.15	0.80	1.84	2.83	-	-	-	-	-	-
0.20	0.50	0.22	1.43	-	0.37	1.33	-	0.40	1.11	-
0.40	1.01	0.10	0.73	-	0.17	0.57	-	0.23	0.55	-
0.60	1.51	0.08	0.45	-	-	-	-	-	-	-
0.80	2.02	0.06	0.27	-	-	-	-	-	-	-

Table A-2: Summary of results listing the dimensionless critical flow velocities u_i for all U_o/U_i (u_o/u_i) ratios investigated for pipe II.

			D_{ch} = 54 mm Pipe II	
U_o/U_i	u_o/u_i	$u_{cr,1}$	$u_{cr,2}$	$u_{cr,3}$
0.033	0.045	1.04	1.98	3.77
0.06	0.08	0.90	1.47	3.04
0.20	0.27	0.52	-	-
0.40	0.55	0.24	-	-

Table A-3: Comparison of the dimensionless critical flow velocities u_i for all U_o/U_i (u_o/u_i) ratios investigated with pipe I for various eccentricities.

		Concentric $t_{gap,1}$ = 0 mm			Eccentric $t_{gap,1}$ = 10 mm			Eccentric $t_{gap,1}$ =14 mm		
U_o/U_i	u_o/u_i	$u_{cr,1}$	$u_{cr,2}$	$u_{cr,3}$	$u_{cr,1}$	$u_{cr,2}$	$u_{cr,3}$	$u_{cr,1}$	$u_{cr,2}$	$u_{cr,3}$
0.015	0.038	2.11	3.79	6.66	1.70	3.25	5.48	1.54	2.97	4.50
0.20	0.50	0.22	1.43	-	0.16	1.93	-	0.009	1.86	-
0.40	1.01	0.10	0.73	-	0.11	0.79	-	0.10	0.69	-
0.80	2.02	0.06	0.27	-	0.09	0.38	-	0.037	0.37	-

Table A-4: Dimensionless comparison in terms of dimensionless parameters defined in [75,76] for pipes I and III of different length for all U_o/U_i (v_o/v_i) examined.

		Plexiglas tube (L' = 200 mm) Pipe I (L = 441 mm)			Plexiglas tube (L' = 100 mm) Pipe III (L = 221 mm)		
U_o/U_i	v_o/v_i	$v_{cr,1}$	$v_{cr,2}$	$v_{cr,3}$	$v_{cr,1}$	$v_{cr,2}$	$v_{cr,3}$
0.015	0.031	0.71	1.28	2.24	1.09	1.49	3.96
0.20	0.42	0.07	0.48	-	0.12	0.68	-
0.40	0.84	0.03	0.25	-	0.06	0.27	-
0.80	1.68	0.02	0.09	-	0.03	0.16	-

Table A-5: Summary of the dimensionless critical flow velocity ratios of pipe III to pipe I for all U_o/U_i ratios investigated.

U_o/U_i	$\frac{u_{cr,1}\text{ (pipe III)}}{u_{cr,1}\text{ (pipe I)}}$	$\frac{u_{cr,2}\text{ (pipe III)}}{u_{cr,2}\text{ (pipe I)}}$	$\frac{u_{cr,3}\text{ (pipe III)}}{u_{cr,3}\text{ (pipe I)}}$
0.015	0.77	0.58	0.88
0.20	0.82	0.71	-
0.40	1.00	0.55	-
0.80	0.83	0.85	-

Table A-6: Comparison of the dimensionless critical flow velocities u_i for all U_o/U_i (u_o/u_i) ratios investigated with pipes I and III of different length and constant $r_{ann} \simeq ½$.

		Plexiglas tube (L' = 200 mm) Pipe I (L = 441 mm)			Plexiglas tube (L' = 100 mm) Pipe III (L = 221 mm)		
U_o/U_i	u_o/u_i	$u_{cr,1}$	$u_{cr,2}$	$u_{cr,3}$	$u_{cr,1}$	$u_{cr,2}$	$u_{cr,3}$
0.015	0.038	2.11	3.79	6.66	1.62	2.21	5.89
0.20	0.50	0.22	1.43	-	0.18	1.01	-
0.40	1.01	0.10	0.73	-	0.10	0.40	-
0.80	2.02	0.06	0.27	-	0.05	0.23	-

Table A-7: Comparison of the dimensionless critical flow velocities u_i for all U_o/U_i (u_o/u_i) ratios examined with pipe III for the cases of no constriction and an inlet constriction.

		No constriction			Constriction at cantilevered end D_{ring} = 20 mm		
U_o/U_i	u_o/u_i	$u_{cr,1}$	$u_{cr,2}$	$u_{cr,3}$	$u_{cr,1}$	$u_{cr,2}$	$u_{cr,3}$
0.015	0.038	2.11	3.79	6.66	0.65	2.02	-
0.20	0.50	0.22	1.43	-	0.06	0.25	-
0.40	1.01	0.10	0.73	-	0.03	0.11	-
0.80	2.02	0.06	0.27	-	0.01	0.04	-

Table A-8: Comparison of the dimensionless critical flow velocities u_i for all U_o/U_i (u_o/u_i) ratios examined with pipe III for the cases of no constriction and an outlet constriction.

		No constriction			Constriction at free end D_{ring} = 32 mm		
U_o/U_i	u_o/u_i	$u_{cr,1}$	$u_{cr,2}$	$u_{cr,3}$	$u_{cr,1}$	$u_{cr,2}$	$u_{cr,3}$
0.015	0.038	2.11	3.79	6.66	0.90	3.17	-
0.20	0.50	0.22	1.43	-	0.09	0.41	-
0.40	1.01	0.10	0.73	-	0.06	0.38	-
0.80	2.02	0.06	0.27	-	0.02	0.19	-